High Anisotropy Magnetic Materials for Data Storage and Spintronic Memory

A DISSERTATION

SUBMITTED TO THE FACULTY OF

UNIVERSITY OF MINNESOTA

BY

Patrick Aaron Quarterman

IN PARTIAL FULFILLMENT OF THE REQUIREMENTS

FOR THE DEGREE OF

Doctor of Philosophy

Advised by Jian-Ping Wang

January 2018

Acknowledgements

I can proudly say that the work I present here is my own, but I would never have arrived here without the support of my family, friends, teachers and countless others. I sincerely hope I did not miss anyone in this section.

First, I want to thank my adviser Jian-Ping Wang. You provided guidance by knowing when to step in and when to take a hands-off approach. I have greatly enjoyed our discussions on topics ranging from spintronics, our research moon shots ideas, and finally to the everyday aspects of life. You have also fostered a great relationship between group members which will last well beyond the years of grad school.

Thank you to all the amazing teachers over the years I've had. The WOSO coaches will always hold a special place for fueling my desire to go into the sciences. I especially want to thank Mr. August Lukow and Bob Myers who never once told me what I couldn't do, but simply provided me the resources to try—I will never forget the years discussing trebuchet designs and more under your guidance. Dr. Wayne Repko, not only were you a professor who inspired me to continue the physics path, showed me how to treat everyone with respect, and even helped elevate my tennis serve. Dr. Norman Birge, you have been an incredible mentor even after I left your group.

Nathan, Boo, Ali, Ang, Todd, Mint, and Andy, you all made the ups of the PhD program more fun, and the downs more bearable. Thanks for all the good times in Keller hall! Also, my fellow group mates, past and current, you have been incredible colleagues over the years. I've enjoyed our discussions many wonderful and varied chats over the years which made the office a wonderful place to work. I also want to thank all the Charfac staff for their willingness to work and help students like me. Especially Javier, who I worked with as close as any group member; it was a pleasure learning from you, collaborating with you, and most of all the friendship that developed from our work together. I also want to thank my many fantastic collaborators over the years. Without you, much of the work in this dissertation would not have been possible.

Finally, and most importantly, I want to thank my family who have never been anything but supportive since day one… of any goal. Your never-ending support and pushing for me to do my best has been a constant source of energy. And so, the following pages are equally a tribute to your dedication to being supportive parents as it is to my studies and research.

Dedication

To my family, friends and teachers

Abstract

Data storage technologies that utilize magnetic materials for storage are key for both increasing areal density of storage in traditional hard disk media and providing low energy alternatives to traditional CMOS technology through spintronic memory and logic devices. Spintronic memory relies on the spin of an electron rather than charge and is a promising candidate for achieving non-volatility which can provide dramatic energy savings. A key challenge for magnetic based storage is achieving 10 nm or smaller feature sizes while retaining thermal stability. This requires development of magnetic thin films with large magnetocrystalline anisotropy. Switching the magnetization of high anisotropy magnetic materials requires large Oersted field or spin current. One way to decrease the switching energy is to lower the anisotropy during the switching process with an applied strain or heat. This scheme retains thermal stability during storage and makes write energies feasible from a technological aspect. Development of suitable high anisotropy materials at sub 10 nm scale has proved difficult due to limitations on traditional thin film growth methods, nanoscale effects, and additional requirements on materials for memory applications. The effect of a static strain on the magnetic anisotropy is well understood, but less so for application in devices which require fast switching and high cycling. The other approach to lowering switching energies is to use magnetic materials with small magnetization, such as Mn-based compounds.

I will discuss my experiments to advance understanding of: development of FePt for HAMR media, effect of strain assisted switching on the spin state of FePt, and development of novel high anisotropy Mn-based materials with low magnetization. Finally, I will present my experimental realization of Ru as the 4th room temperature ferromagnetic element. Ru has been predicted to become ferromagnetic when placed into a metastable tetragonal or cubic phase. This new phase of Ru also has potential to achieve the requirements for a viable spintronic device. I will show my work on the realization of the tetragonal phase Ru using seed layer engineering in thin films, and its associated ferromagnetic properties.

Table of Contents

List of Tables

List of Figures

Chapter 1. Introduction to magnetic data storage

1.1. General magnetism

Magnetism has garnered interest since even ancient times for use in navigating the globe using the compass. In modern times, magnetism can be found in countless aspects of life-- such as refrigerator magnets, theft prevention, motors, speakers, MRIs, and data storage. It is the last item application of magnetism, data storage, which this dissertation focuses on. Historically, magnetism has dominated in tape and hard disk drive (HDD) storage, whereas semiconductors have cornered random access memory (RAM). Since the discovery of giant magnetoresistance and tunneling magnetoresistance over the last few decades, ferromagnetic materials have become among the hottest topics of study in the research community since there is both room for many fundamental studies, and commercial applications. In upcoming data storage technologies there is a likely upcoming about-flip. Solid state drives (SSD), based on semiconducting technology, are overcoming traditional HDD technologies at a rapid pace for consumer level storage, and is encroaching on enterprise level as well. However, semiconductor RAM are volatile storage—that is they require constant power to retain data storage; in addition, the power density of these devices is rapidly approaching the limit of heat dissipation. Magnetic random-access memory (MRAM) technologies are intrinsically non-volatile and have potential to achieve significant energy savings—if current challenges in write energies are overcome.

There are five fundamental types of magnetic materials: diamagnetic, paramagnetic, ferromagnetic, ferrimagnetic, and antiferromagnetic. All five types will be summarized briefly, but since this dissertation's focus is primarily on ferromagnetic materials, emphasis will be primarily on ferromagnetism and relevant effects in ferromagnets that make these materials valuable for data storage and spintronic memories.

Ferromagnetism occurs is when there is a net magnetic moment in the absence of an external field and is due to electron spins of a system aligning in a parallel orientation; conversely anti-ferromagnetism occurs when the spins align anti-parallel, leading to a net moment of zero. Ferrimagnetism occurs when spins align anti-parallel, but there are two sublattices with different magnetization, and so there is a non-zero net magnetic moment. Paramagnetic and diamagnetic materials have a random orientation of local moments in a zero-magnetic field condition, but when a field is applied they orient parallel and anti-parallel, respectively, as a linear function of the applied field.

Ferromagnets tend to align their magnetic dipoles in parallel due to the exchange interaction, which is a purely quantum mechanical effect, and there is no classical picture for this effect. Ferromagnets have what is known as a Curie temperature (T_c), a material dependent temperature, and when this temperature is exceeded a material transitions from being ferromagnetic to paramagnetic. Despite this quantum mechanical basis, ferromagnetism has a long history of study, but to date only three single elements display room temperature

ferromagnetism—Fe, Co and Ni [1]. Gd nearly misses room temperature ferromagnetism with a Curie temperature of 293 K [2], and Pd and Pt narrowly miss the Stoner criteria (Fig 1.1), which states that ferromagnetism exists when the product of the exchange integral and the density of states at the Fermi level is greater than unity [3].

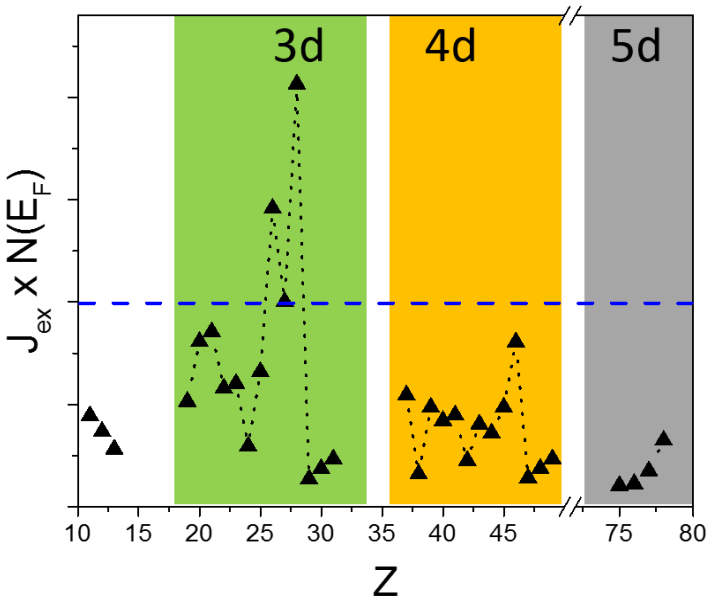

Fig 1.1: Calculation of the Stoner criterion for determination of transition metal ferromagnetic elements as a function of atomic number. Elements above the dashed line (J_{ex} x $D(E_F)$ > 1) are predicted to be ferromagnetic.

In addition, countless alloys have been produced, which are composed of at least one 3d element, such as NiFe, FePt, CoPt, $SmCo_5$, MnBi, and more; they vary in anisotropy constant, K_u, from 10^5-10^8 erg/cm^3. In chapter 6 of this dissertation I will introduce my work demonstrating that Ru can become the fourth single element ferromagnetic material at room temperature, which has long been predicted by theoretical works.

The magnetic moment is denoted as *m*, however, it is generally more common to discuss the magnetization (*M* = *m*/*V*) as this is a material specific parameter. In addition, the CGS units will be used for magnetic values as a general rule of thumb.

1.2. Demagnetization field

Ferromagnetism can most easily be understood from a magnetic dipole picture, with the simplistic picture of “north” and “south” poles. If the ferromagnet is magnetized such that the field curls from the “north” pole to the “south” pole, then inside the magnet there is a magnetic field (H) that is pointing anti-parallel to the magnetization direction—this field is known as the demagnetization field (H_d). H_D is strongly dependent on the geometry of the ferromagnet ($\overleftrightarrow{\boldsymbol{N}}$, the demagnetization factor), and is described by equation 1.1. In CGS units, the sum of the demagnetization factors along three orthogonal vectors must add to 4π, or 1 in SI units.

$$H_d = -\overleftrightarrow{\boldsymbol{N}}\boldsymbol{M} \tag{1.1}$$

$$N_{xx} + N_{yy} + N_{zz} = 4\pi \tag{1.2}$$

In general, $\overleftrightarrow{\boldsymbol{N}}$ can be quite difficult to calculate, but in some cases, it can be determined *a priori* based on the symmetry—for example in a thin film N_{zz} is the unique axis and so $N_{zz} = 4\pi$ and the other terms are zero.

1.3. Anisotropy

The term anisotropy referrers to properties having directional dependence. Magnetic anisotropy is the property of magnetic materials to have a preferred magnetization orientation—this can arise from material shape, crystal structure, and strain.

1.3.1. Shape anisotropy

Shape anisotropy arises from the long range dipolar coupling via the demagnetization field since the strength of the demagnetization field is different along different axes, which implies the only shape having no shape anisotropy is that of a perfect sphere. The shape anisotropy term can be calculated from:

$$K_{shape} = \int -H_d \cdot dM = \frac{1}{2} M^2 \overleftrightarrow{\boldsymbol{N}} \tag{1.3}$$

In the case of a thin film, approximated by an infinite plane, this becomes:

$$K_{shape} = 2\pi M_{zz}^2 = 2\pi M_s^2 \cos\theta \tag{1.4}$$

1.3.2. Magnetocrystalline anisotropy

Magnetocrystalline anisotropy (MCA) is the result of spin-orbit coupling interacting with a crystal field. Specifically, the crystal field is strongly tied to the bonding associated with the crystallographic structure, and this crystal field then couples to orbital shape and electronic structure because the orbital moments are quenched [4]. This results in a preference of spins to align with energy favorable crystallographic directions (easy axis) and resist unfavorable crystallographic directions (hard axis) [5]. The magnetocrystalline anisotropy energy (MAE) is the

energy required to overcome the spin-orbit coupling and rotate the spins from the easy to hard crystallographic axis. There are several types of MCA—cubic, hexagonal, and uniaxial, with the last being the most relevant for data storage. In a cubic crystal system, such as body centered cubic (BCC) Fe, it is simple to image that there is rotational invariance in the symmetry for the <100> family of crystallographic planes, and as such these are the easy axis planes. The <111> family of planes in turn form the hard axis. In the case of Ni, which has face centered cubic (FCC) structure, the situation is inverted, where (100) is the hard axis and (111) the easy axis. Co has hexagonal close pack (HCP) structure, and as is characteristic of hexagonal structures, the (0001) axis is the easy axis, which is to be expected intuitively from the rotation symmetry of the hexagonal crystal structure. Uniaxial is a specific case in which a material has a single easy axis; this form of anisotropy is the most common in data storage applications, and will be used for derivations in this chapter. Uniaxial anisotropy is common in crystals such as hexagonal or tetragonal structures. The energy of a uniaxial MCA is described as a power series as shown in Equation 1.5a, where θ is the angle between the magnetization and easy axis. In practice the anisotropy term is limited to K_{u1} and K_{u2} terms, and the K_{u0} term has no physical meaning, and so is disregarded [5].

$$\frac{U}{V} = \sum_n K_{un} \sin^{2n} \theta \approx K_{u1} \sin \theta + K_{u2} \sin^4 \theta \quad (1.5a)$$

$$K_u = \sum_n K_{un} \quad (1.5b)$$

Conventionally, $K_u > 0$ means there is a uniaxial easy axis, and $K_{us} < 0$ implies no easy axis. In practice, it is desirable for the uniaxial easy axis to be aligned perpendicular to the substrate plane (out-of-plane), and the hard axis lies parallel to the substrate plane (in-plane).

1.4. Effects of stress

In 1842 Joule discovered that when an iron rod is exposed to a magnetic field, the length of the rod changed—in effect a magnetically induced strain. This effect is now known as magnetostriction (λ), and defined from the change in the length (*l*):

$$\lambda = \frac{\Delta l}{l} \tag{1.6}$$

Direct magnetostriction effect tends to be quite small ($\lambda \sim 10^{-5}$), and is not of much important, but there is a related effect, inverse magnetostriction, which has historically been important. And recently is of interest to modify the magnetization switching energy. Inverse magnetostriction is when a strain is applied, and a resultant change in the anisotropy and magnetization [4]. In general, calculating a strain induced anisotropy is quite involved given that it is intrinsically tied to the crystal symmetry, however, it is common to assume that in the case of a cubic crystal with an applied stress (σ) the magnetoelastic anisotropy term is:

$$K_{me} = \frac{3}{2}\lambda\,\sigma\sin^2\theta \tag{1.7}$$

Strained magnetic materials are commonly generated in thin film applications due to mismatches between crystal layers even in highly epitaxial multilayers. Using a

ferroelectric heterostructure in contact with a ferromagnetic material allows for a voltage applied to the piezoelectric to modulate the magnetic properties of the magnetic layer via an induced strain, which will further be discussed in the following chapters. Traditionally the effect of strain on magnetic materials has been calculated by determining an overall anisotropy term that is a sum of shape, MCA, and strain terms, however, with recent advances in technologies this is no longer an acceptable assumption, and will be looked at in detail in chapter 4 for $L1_0$ FePt.

Strains are also of interest given that they provide the ability to stabilize certain crystal phases in thin films. Often a thin film is constrained to the equilibrium phase simply by bonding to the substrate surface—that is the expected phase from the calculated phase diagram. It is possible using strain generated from an epitaxial relation, however, to stabilize the growth of a metastable phase, which opens a plethora of studies into magnetic materials that cannot exist in bulk form [1]. An example of this will be explored in chapter 6 as the formation of a metastable Ru phase has been developed and characterized.

1.5. Magnetization process and hysteresis

When a field is applied to a virgin ferromagnet (i.e. as-grown, never magnetized before) there can be a wide variety in the behavior of the magnetization vs. field characteristics. As the magnetic field increases, the initially randomly oriented spins of the system gradually rotate to be parallel to the field, eventually once all the spins are parallel, this is known as the saturation regime. Once saturated and if the field is swept to negative saturation field, then for the

easy axis there will be a rapid rotation in the magnetization direction at the negative coercive field (H_c). However, if the field is swept along the hard axis, the magnetization will rotate linearly with field to the opposite magnetization direction between $+H_c$ and $-H_c$. M vs. H hysteresis loops for the field sweeps along the easy and hard axis are shown in Fig 1.2. Ferromagnetic materials which require a large field to saturate are known said to be 'hard' and materials which require little field are 'soft'. A ferromagnet is said to be 'switched' once it has fully reversed from one saturation

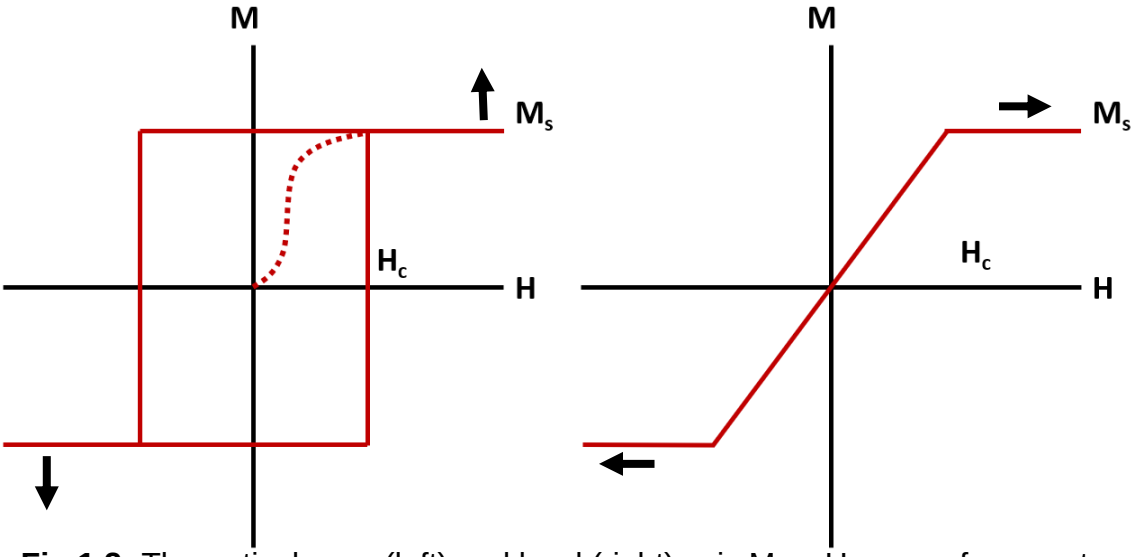

Fig 1.2: Theoretical easy (left) and hard (right) axis M vs H curves for a system with uniaxial anisotropy. The dashed line on the easy axis curve shows the virgin curve, which is due to domain wall motion at low field, and rotation near saturation.

state to the other. In practice the turning point of the hard axis loop is used to estimate the true anisotropy constant of a thin film sample.

1.6. Stoner-Wohlfarth Switching

The M vs H hysteresis loops can be demonstrated quite easily using the Stoner-Wohlfarth method. In this model, a single domain particle with uniaxial anisotropy and uniform magnetization, at angle α to the easy axis is considered when a field (H) is applied at an angle θ from the easy axis, and the set up for this problem is shown in Fig 1.3. The total energy per volume can be written as a sum of a generalized anisotropy energy term (MCA, strain, etc.) and the potential energy from an applied field:

$$\frac{E}{V} = K_u \sin^2\theta + HM_s \cos(\alpha - \theta) \tag{1.8}$$

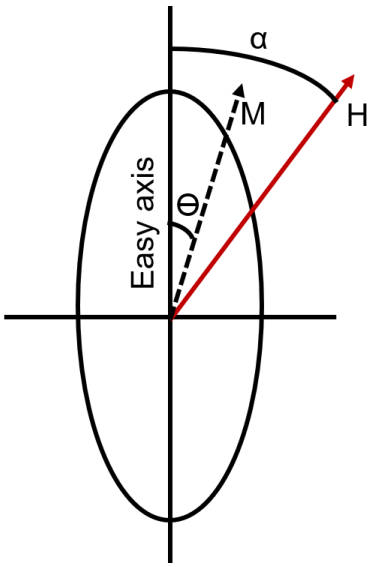

Fig 1.3: Setup for Stoner-Wohlfarth model of magnetization switching process.

The minimum energy can then be found by setting the derivative of (1.8) to zero:

$$\frac{dE/V}{d\theta} = 2K_u \sin\theta\cos\theta - HM_s \sin(\alpha - \theta) \tag{1.9}$$

It is now useful to define the anisotropy field H_k, which in a perfect single domain film is equal to H_c:

$$H_k = \frac{2K_u}{M_s} \tag{1.10}$$

and divide H by this to arrive at a quartic equation in $\sin\theta$:

$$h = H/H_k \tag{1.11a}$$

$$\sin\theta\cos\theta - h\sin(\alpha - \theta) = 0 \tag{1.11b}$$

which can be used to solve for M vs H behavior, and for the case of α = 0° and 90° leads to the M vs H curves shown in Fig 1.2.

1.7. Thermal fluctuations

The expressions arrived at thus far using the Stoner-Wohlfarth model do not account for the effect of temperature and size dependence of magnetic particles—denoted by a volume, V. Temperature effects in magnetic particles lead to thermal fluctuations when the volume is small enough that the thermal energy is enough to overcome the anisotropy energy, and as such there is the possibility of the magnetization switching from one state to another, without an external field. The probability (P) of a thermal fluctuation from state 1 to state 2 can be described from an Arrhenius formulation:

$$P = f_0 e^{-\Delta E/k_B T} \tag{1.12}$$

f_0 is known as the attempt frequency (generally between 10^7 and 10^{12} Hz), and for a particle with uniaxial anisotropy:

$$\Delta E = K_u V \tag{1.13}$$

And for a collection of such particles, the rate of switching from state 1 to state 2 can be derived as:

$$\frac{dM}{dt} = -PM = -Mf_0 e^{-\Delta E/k_B T} = \frac{M}{\tau} \quad (1.14a)$$

$$\frac{1}{\tau} = f_0 e^{-\Delta E/k_B T} \quad (1.14b)$$

$$\frac{dM}{M} = -\frac{dt}{\tau} \quad (1.14c)$$

$$\ln M = \frac{t}{\tau} \quad (1.14d)$$

$$M = M_o e^{-t/\tau} \quad (1.14e)$$

And so, for thermal stability, with time constant τ_0, the requirement for thermal stability is:

$$Log(\tau_0 f_0) > \frac{K_U V}{kT} \quad (1.15)$$

Which for the typical data storage requirement of 10 years, this factor is ~ 60, and measurement times require 100 s, leading to a factor of 25. This also shows the need for materials with large K_u, for example, in the case of a cylindrical single domain magnetic cylindrical pillar that is 5 nm tall, a K_u of 7 x 10^6 erg/cm^3 is needed to retain thermal stability with a diameter of 5 nm (assuming room temperature).

1.8. Magnetic dynamics

The Stoner-Wohlfarth model and related models on thermal fluctuations provide a relatively simple model to understand the magnetization process of magnetic materials. However, these models cannot account for the complexities

of magnetic dynamics in realistic materials. When predicting dynamic behavior, it is common to use micromagnetic techniques, which generally involves using computational methods to solve the Landau-Lifshitz-Gilbert-Slonczewski equation:

$$\frac{1}{\gamma}\frac{d\boldsymbol{m}}{dt} = -\boldsymbol{m} \times \boldsymbol{H}_{eff} - \frac{\alpha}{\gamma M_s}\frac{d\boldsymbol{m}}{dt} \times \boldsymbol{m}$$

$$-\frac{\hbar}{2e}\frac{\eta I}{m^2}(\boldsymbol{n_s} \times \boldsymbol{m}) \times \boldsymbol{m} - \boldsymbol{m} \times \boldsymbol{H}(\alpha T) \qquad (1.16)$$

Where the first term is the precession, followed by the damping, spin torque (Slonczewski term), and finally the thermal fluctuation term.

1.9. Magnetoresistance

Magnetoresistance, as its name implies, is the effect in which the electrical resistivity is dependent on the magnetic field experienced by the conducting electrons. There multiple classifications under the magnetoresistance (MR) family such as anisotropic magnetoresistance (AMR), colossal magnetoresistance (CMR), giant magnetoresistance (GMR) which won the Nobel prize in 2007, and tunneling magnetoresistance (TMR) which is most applicable to this dissertation [5]. In the case of GMR and TMR, when there is a trilayer stack of ferromagnet/spacer/ferromagnet the electrical resistance varies when the ferromagnetic layers are aligned in a parallel (R_P) or antiparallel (R_{AP}) configuration, which is shown in Fig 1.4. The difference in resistivity can understood by drawing the density of state diagrams for the parallel and anti-parallel states, shown in Fig 1.4, and the availability states for an electron traveling

from the first to second ferromagnetic layer. In GMR the spacer is a non-ferromagnetic metal, and in TMR is an insulator such as MgO. TMR will be the focus of MR effects in the remainder

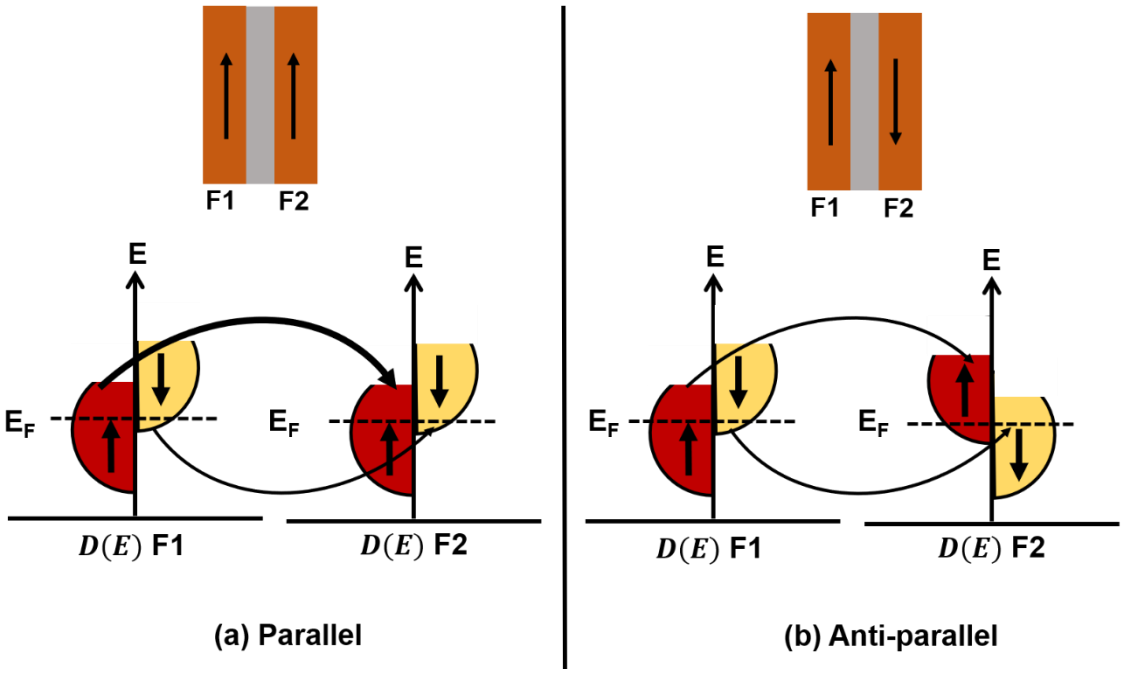

Fig 1.4: Schematic of a ferromagnet/insulator/ferromagnet TMR for (a) parallel (low resistance) and (b) anti-parallel (high resistance) states. The density of states D(E) is also illustrated as a simple explanation for parallel state having lower resistance than anti-parallel state.

of this dissertation, which has its origin in spin dependent tunneling behavior, and forms the basis for magnetic tunnel junctions (MTJs) which are the fundamental building block of MRAM. A large tunneling magnetoresistance (TMR) ratio is desirable for data storage application and is defined as:

$$TMR = \frac{R_{AP} - R_P}{R_P} \tag{1.17}$$

In TMR it is also useful to define the spin polarization ratio (*P*), which is defined from the density of states *D(E)* for a ferromagnetic electrode with the spins aligned

($D_{\uparrow}(E)$) and anti-aligned ($D_{\downarrow}(E)$) to an external magnetic field, as proposed by Julliere:

$$P = \frac{D_{\uparrow}(E_F) - D_{\downarrow}(E_F)}{D_{\uparrow}(E_F) + D_{\downarrow}} \tag{1.18}$$

If the two ferromagnetic electrode layers are then described as having spin polarizations of P_1 and P_2, the TMR ratio from (1.17) can be re-written as:

$$TMR = \frac{2P_1P_2}{1 - P_1P_2} \tag{1.19}$$

Since the spin polarization comes directly from the density of states, it is a material dependent property, and in order to achieve as large of a TMR as possible, achieving P as close to 1 is an ongoing research topic. It is also worth noting the spin polarization is the tunneling spin polarization, and so is dependent on the insulating spacer. This is important form a historical perspective since TMR was initially shown using amorphous Al_2O_3, but it has since been shown that MgO provides larger TMR due to the symmetry of the Δ states. Practical application of TMR for use in MRAM technologies will be discussed in the following sections.

1.10. Data storage and memory applications using magnetics

High K_u magnetic materials have two key applications in data storage technologies: hard disk media and spintronic memories. Perpendicular magnetic materials (i.e easy axis perpendicular to substrate) is preferred due to its ability to provide higher areal densities. In both technologies, the hard magnetic layer can be considered to have three key requirements: thermal stability, low write energy, and ‘readability.’ In both magnetic recording and spintronics, the thermal stability

requirement arises from the figure of merit derived in equation 1.20, which shows that for 10 year storage:

$$\frac{K_u V}{k_B T} > 60 \tag{1.20}$$

Thus, for decreasing feature sizes (i.e. V) to increase storage capacity, materials with large K_u are required—this is the primary motivation of this dissertation. Furthermore, materials with perpendicular anisotropy are preferred for data storage given that higher K_u values are possible, there is no shape anisotropy. The readability and writability requirements are quite different between the two technologies however, since the read-write process is fundamentally different. These requirements will be discussed in detail in the following sections.

1.10.1. Magnetic recording

Magnetic recording technology was initially invented in the 1950s, with areal densities on order of only a few Kbit/in^2 (5 MB storage capacity). Since then there has been an ever-increasing push for higher areal densities fueled by discoveries in thin film technology, magnetoresistance, and perpendicular writing (Fig 1.5a) [6]. Currently research is pushing for areal densities greater than 1 TB/in^2 using novel technologies such as heat assisted magnetic recording (HAMR), bit patterned media (BPM), and microwave assisted magnetic recording (MAMR). The expected road map for the development of these technologies, and the areal densities they will achieve provided by ASTC can be seen in Fig 1.5b [7].

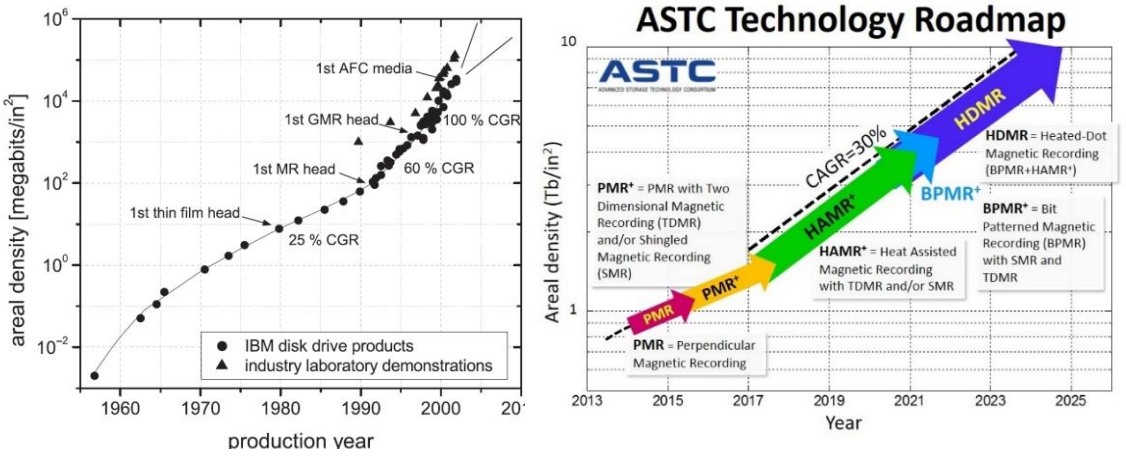

Fig 1.5: (a) History of areal density in HDD technology with key technological milestones [6]. https://doi.org/10.1088/0022-3727/35/19/201 © IOP Publishing. Reproduced with permission. (b) Roadmap of hard disk drive areal densities for upcoming technologies [7].

The disk, or platters, are where data is stored in a hard-magnetic material layer at the top surface. Along the disk, there are concentric rings, known as tracks which is spun on a spindle at 5 kRPM and faster and the track is made up of bits. Magnetic media (storage layer) is grown into a granular array with a boundary matrix of a non-magnetic material (commonly oxides), and bunches of grains that are exchange coupled together form a single bit. A magnetic read-write head is attached to an actuating arm, which allows for the head to access every bit, on every track simply by moving the arm and rotating the disk. The read-write head, as the name implies, allows for determination of the magnetization direction of the bits, and rotate the magnetization direction using a field from the writer.

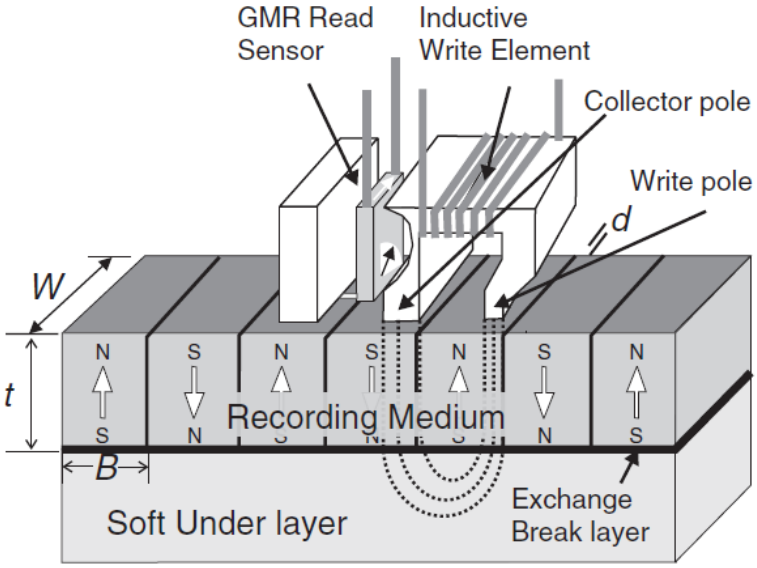

Fig 1.6: Schematic of the perpendicular magnetic recording scheme [6]. https://doi.org/10.1088/0022-3727/35/19/201 © IOP Publishing. Reproduced with permission.

In modern perpendicular magnetic recording, the read-write head consists of a pole head that is used to generate a magnetic field for switching the magnetization direction of bits, and a GMR/TMR sensor to determine the magnetization direction. The magnetic media is broken up into bits that consist of grains with large perpendicular magnetic anisotropy; there is a soft magnetic under layer material to complete the magnetic flux lines for the head. The free layer of the read head is forced to align its magnetization based on the stray field of the magnetic material, and the resulting resistance for a parallel or anti-parallel state is used to determine the bit magnetization state. A schematic for a perpendicular magnetic recording head and media is shown in Fig 1.6 [6]. The write field that the pole in the head can apply is proportional M_s of the pole material, and the highest M_s materials are found from the Slater-Pauling curve (Fig 1.7 [4]); FeCo has the maximum head

field with approximately 2.45 T. The development of higher M_s materials such as $Fe_{16}N_2$ is also an active research field to go beyond FeCo alloys. This in practice implies that there is a limit to the field that can be applied to the the bit for switching, and so places a limitation on the coercive field of the media layer. This is known as the writability issue, which states that in conventional magnetic recording the field necessary to write the bit must be less than the write head field, where the coercive field is:

$$H = \alpha \frac{2K_u}{M_s} - N_{eff} M_s \tag{1.21}$$

Where α is the structure factor and N_{eff} is the effective demagnetization factor for the media layer. This creates a dilemma, since for thermal stability a large K_u is required, but if K_u is too large there is not enough available write field to change the magnetization direction.

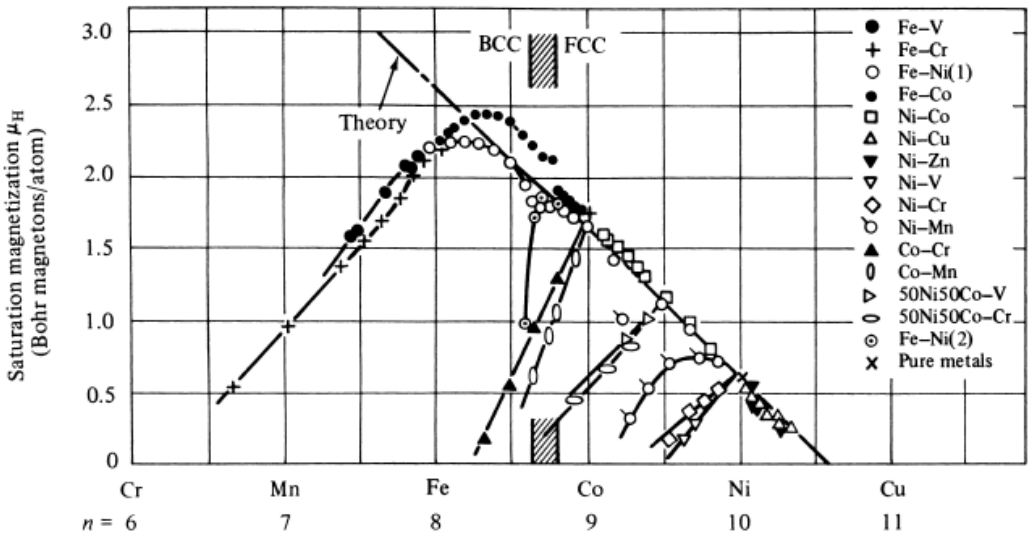

Fig 1.7: The Slater-Pauling curve, which shows the magnetization for various magnetic alloys [4].

This dilemma involving K_u for maintaining thermal stability and a small enough write field is solved by introducing a new write scheme—HAMR. In HAMR a high K_u material, such as $L1_0$ FePt, is used for the media, which has a coercive field too large to be written by the pole field at room temperature, but this allows for grains to avoid superparamagnetism at feature sizes as small as 3 nm. In order to flip the FePt magnetization, a laser is used to heat the bit to near the Curie temperature, which results in a low coercive field long enough to write the bit. The laser is then turned off, and the FePt bit to cools down to room temperature to regain its large K_u. This process is shown in Fig 1.8. HAMR has faced a great number of research challenges, such as focusing the laser down to adequate spot sizes by using near field transducers, and growing highly ordered $L1_0$ FePt with sub 8 nm grains has proved more challenging than expected when HAMR was proposed, but HAMR is on track to be in commercial products within the upcoming year or two.

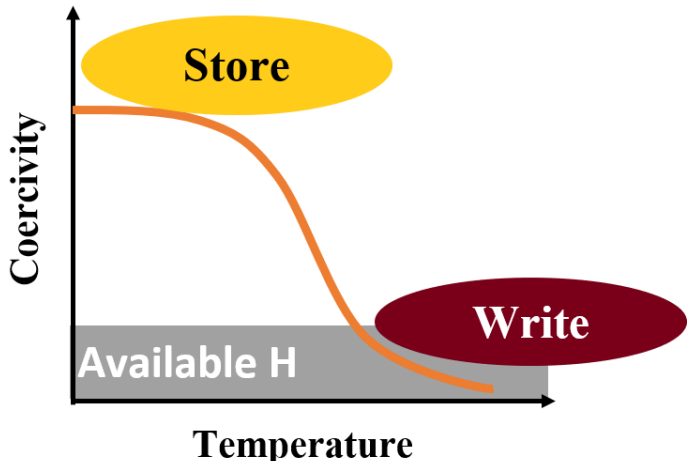

Fig 1.8: The working principle of HAMR, which allows for ultra-high K_u materials to be written using a laser to heat the hard layer long enough to flip the magnetization.

1.10.2. Spintronics

Spintronic memories and logic devices, which rely on magnetic tunnel junctions (MTJs) as the fundamental building block, are of great interest due to their intrinsic non-volatile property [8–10]. The MTJ consists of a ferromagnetic tunnel barrier, in which one ferromagnetic layer is the fixed (reference) layer, and the other ferromagnetic layer is the free layer. The fixed layer is frequently set by using an anti-ferromagnetic layer, such as IrMn, to exchange bias the magnetization into a fixed direction. Spin torque transfer random access memory (STT-RAM) is a promising technology for writing the free layer of the MTJ utilizing momentum transfer from a spin polarized current [11–13]. STT allows for direct switching of the magnetization of the free layer in a MTJ by a charge current, which makes it appealing for application, since no external magnetic field is required. In the STT scheme, a charge current is passed through a ferromagnetic material and the charge current becomes spin polarized. The electrons in the spin polarized current are aligned such that their spin is parallel to the direction of the ferromagnet magnetization due to an imparted angular momentum transfer from the ferromagnet to the charge current electrons. The spin polarized current can then be used for the write process by imparting an angular momentum to switch the magnetization direction of a ferromagnetic layer. Consider a MTJ in the anti-parallel state, when a charge current pass through the fixed layer, the electrons become spin polarized along the fixed layer direction. When the polarized electrons reach the free layer there is an additional spin torque from the anti-

parallel free layer applying an angular momentum on the electrons to reorient their direction, but due to momentum conservation, the electrons also exert a spin torque on the magnetic free layer. At large enough charge current density (J_c), the imparted torque from the spin current onto the free layer is enough to rotate the magnetization such that the two magnetic layers become aligned in a parallel configuration. The process for magnetization reversal for a parallel to anti-parallel configuration is similar. In this chase, the charge current is applied in reverse direction (free layer to fixed layer), and when the charge current reaches the fixed layer, electrons with the opposite spin direction are reflected towards the free layer, which in turn exert a spin torque to switch the free layer. This switching process for a STT MTJ is summarized in Fig 1.9.

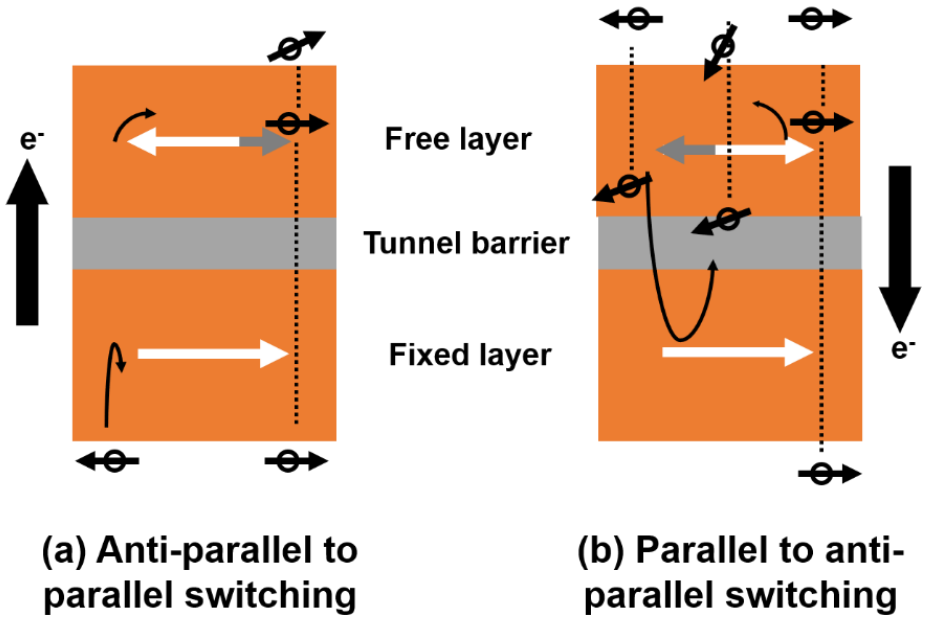

Fig 1.9: Schematic of a MTJ for spin torque transfer switching in the case of (a) anti-parallel to parallel state and (b) parallel to anti-parallel.

The critical current required for perpendicular spin torque magnetization switching is:

$$J_c = \frac{2e\alpha M_s t H_k}{\hbar \eta} \tag{1.22}$$

where α is the Gilbert damping, and η an efficiency parameter. STT writing is currently limited by the large current densities (10^6-10^7 A/cm^2) required for writing, and a current density of 0.5 MA/cm^2 is considered necessary to allow STT-RAM to be competitive. In addition the lifetime of STT-RAM is limited due to the large current passed through the tunnel barrier [14]. In order to achieve energy efficient switching, novel magnetic materials that possess low α and M_s are needed; simultaneously, to maintain thermal stability a large K_u is needed. There is a similar dilemma in spintronics as in magnetic recording, the requirement for thermal stability in high K_u materials directly competes with the need for small write current. Compared to magnetic recording, this dilemma is even more restrictive given that STT write current is sensitive to α and M_s In fact, this is further complicated since high K_u materials rely on materials with 5d orbitals, which also tend to have large damping, and Fe based alloys tend to have relatively large M_s. Traditional materials such as CoPt, FePt, and CoFeB do not fulfill all the necessary requirements. In addition, a large TMR ratio (> 150%) is needed to allow for readability, and from equation (1.19) this implies that materials with large spin polarizations are necessary. Finally, in the STT scheme, the state of the MTJ is read by a current that also travels transverse to the MTJ, which further increases the energy usage of this scheme. One method to lower the write current for STT

switching of magnetization is to use an applied strain during the write process to decrease the write energy needed by modulating K_u. In order to better understand the effects of strain, chapter 4 will focus on the effects of strain on the 3d occupancy of $L1_0$ FePt.

1.11. High anisotropy magnetic materials

Magnetic materials have a wide range of magnetocrystalline anisotropy, from ultra-soft materials, such as $Ni_{80}Fe_{20}$ (permalloy) with $K_u \sim 0$ erg/cm^3, to the highest known anisotropy material of $SmCo_5$ with $K_u \sim 10^8$ erg/cm^3. Figure 1.10 [15] shows K_u and M_s for the most researched high anisotropy materials. It can be seen that $SmCo_5$ has the largest K_u, however it is not used in practice given its instability. FePt has the second largest K_u, and is chemically stable in atmosphere, and so it is a widely studied material for both hard drive media and early MTJs. High anisotropy materials are key in data storage for retaining thermal stability at nanoscale; for example, FePt can retain thermal stability for grain sizes as small as 3 nm. Given that the magnetocrystalline anisotropy is due to spin-orbit coupling, materials that have unpaired spins in the 4*d* and 5*d* orbitals have a larger K_u. As previously discussed, for STT based technologies, magnetic materials with small Ms are desired to reduce the critical switching current densities necessary for switching, and so Fe-based alloys are less desirable due to their large M_s. Mn-based materials have a lower M_s than Fe-based materials, which makes them attractive candidates, and while having a smaller K_u than FePt and FePd, $K_u > 10^7$ erg/cm^3 is considered large enough for current applications. In addition, the critical

current density is dependent on the Gilbert-damping term (α), which increases with spin-orbit coupling, which makes materials with 5d elements less attractive (e.g. FePd is of current interest since it has lower α than FePt). FePt and MnBi have been extensively studied in this dissertation, and so focus will be on introducing these two material systems. In chapter 6 I will introduce Ru as another potential high K_u magnetic material.

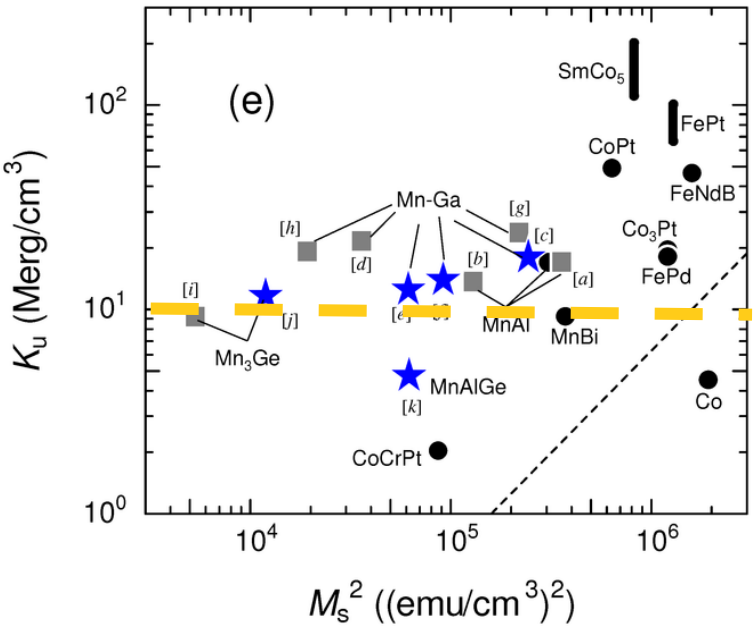

Fig 1.10: Table summarizing K_u and M_s for high anisotropy magnetic materials by Sugihara et al [15].

1.11.1. FePt

FePt has two relevant phases, the chemically disordered FCC magnetically soft A1 phase, and the ordered, magnetically hard $L1_0$ phase which has a face centered tetragonal (FCT) crystal structure. The disordered phase has no preferential location of Fe vs. Pt atoms, but in the ordered phase the FCT structure

is formed of alternating layers of Fe and Pt, as seen in Fig 1.11 [16]. It is possible to describe the extent of the Fe and Pt chemical ordering calculating an ordering parameter (*S*) of a FePt sample using x-ray diffraction:

$$S = \sqrt{\frac{\left(I_{(001)}/I_{(002)}\right)_{Exp}}{\left(I_{(001)}/I_{(002)}\right)_{Theory}}} \tag{1.23}$$

Where *I* is the integrated intensity of the (001) and (002) XRD FePt peaks. This parameter is meant to correspond to a pure A1 phase in the case of S = 0, and pure $L1_0$ when S =1. In highly textured $L1_0$ FePt thin films values for S greater than 1 are commonly measured, and detailed calculations by Yang et al have shown that a correction is required to account for texturing and finite thickness effects in thin films [17]. $L1_0$ FePt has long been studied for its thermal stability at sub 5 nm grain sizes for HAMR, and spintronics, due to its large K_u of 7 x 10^7 erg/cm^3 [18],

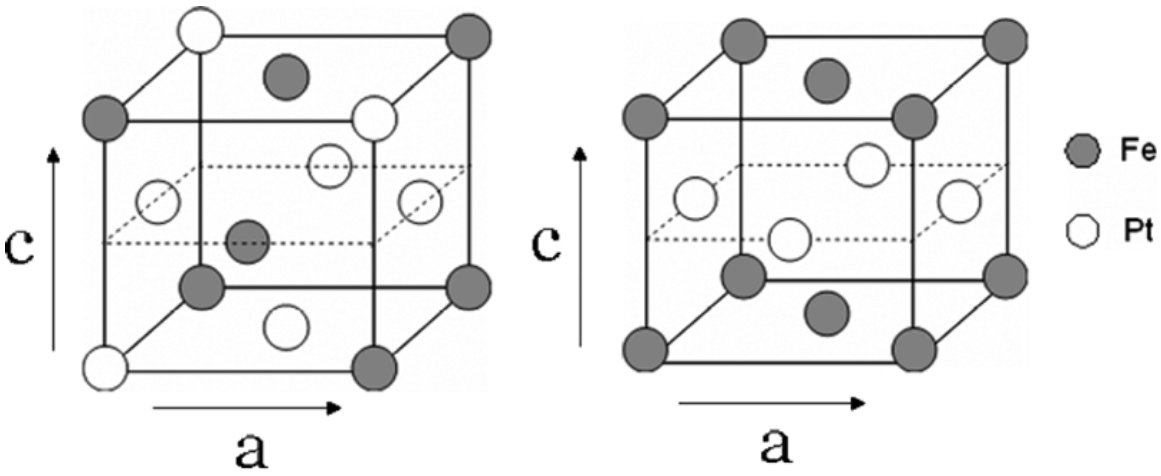

Fig 1.11: Crystal structure of FCC A1 FePt, $L1_0$ FCT FePt [16]. Reprinted from Jian-Ping Wang, "FePt magnetic Nanoparticles and their Assembly for Future Magnetic Media" Proceedings of the IEEE. 96 11 (2008), with permission of AIP publishing.

and chemical stability [19], since to scale below 8 nm, traditional materials, such as CoCrPt in media and CoFeB in magnetic tunnel junctions (MTJs), will not remain thermally stable [20,21]. $L1_0$ FePt thin films and nanostructures have been frequently proposed for their potential in future information storage media [16,22–24], permanent magnets [25] and spintronic devices [26]. The effect of a change to the FePt lattice parameter on the MAE has been well researched, both experimentally and theoretically [27–29]; this effect has been taken advantage of for magnetic recording media by statically straining the FePt film in order to modify magnetic and microstructure properties [30,31]. In chapter for the detailed effects of ordering and strain on the spin and oxidation state of FePt will be examined. Chapter 3 of this dissertation focuses on size and symmetry effects in $L1_0$ FePt, which will be of consequence to the magnetic recording field when trying to achieve grain sizes of 3 nm.

1.11.2. MnBi

Mn based materials such as Mn_3Ge, Mn_2Ga, and MnBi have become of interest due to their relatively large perpendicular K_u as large as 1 - 2 x 10^7 erg/cm^3 and modest M_s of approximately 670 emu/cm^3 or less for MnBi [15,32]. MnBi has a stable low temperature phase (LTP), in which a ferromagnetic NiAs hexagonal structure is formed, and has long been studied for permanent magnet applications [33,34], and more recently in spintronic applications due to its high K_u, low M_s, relatively high spin polarization, and Curie temperature well above room temperature [35,36]. A spin polarization as high as 63% in NiAs structured MnBi

has been experimentally demonstrated [37], however, first-principles calculations predict a meta-stable zinc blende structure of MnBi which is half-metallic [38], but this metastable phase has not been experimentally reported to date. Furthermore, MnBi is of interest due to having an extraordinarily large Kerr angle [39], and predictions of ultra-fast domain wall motion under a thermal gradient [40]. Also having a MTJ based on hexagonal crystal structures allows for integration with alternative tunnel barriers such as BN [41], and can lattice match to several topological insulators for spin orbit torque switching [42,43]. The previous results discussed use island structured MnBi with film thicknesses on order of 5-200 nm, and it has been shown that forming ferromagnetic MnBi at sub 25 nm thicknesses, while maintaining suitable K_u and M_s, is difficult to achieve [44], which must be overcome for MnBi to integrate into MTJ structures. In addition, MTJ thin films require continuous with low surface roughness, not island-like microstructure. The effect of dopants in MnBi has also been examined, and in the case of adding Fe or Au, the magnetization decreases, K_u and magnetoresistance (MR) ratio can be strongly modified, which has been proposed to be resultant of competing ferromagnetic and anti-ferromagnetic interactions [45,46]. In addition MnBi/Al multilayers have been investigated to understand effect of particle size on the magnetization reversal process [47]. K_u for MnBi also has been shown to have an inverse dependence on temperature [48,49], and is still not well understood.

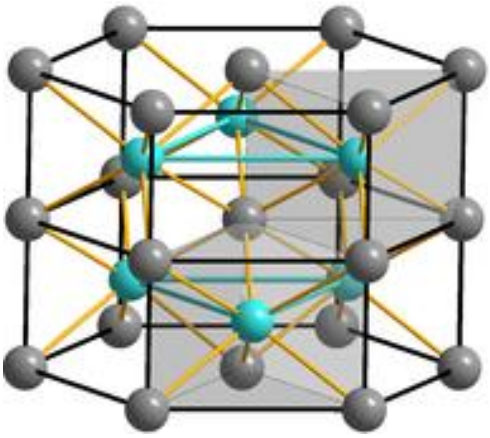

Fig 1.12: NiAs structure for the LTP MnBi phase.

1.12. Dissertation outline

This dissertation summarizes my efforts to develop novel high anisotropy magnetic materials for use in hard disk media and spintronic memories. In addition, it aims to answer fundamental questions in magnetic materials concerning strain and metastable phases, and is presented as follows:

- In **chapter 1** a brief summary of ferromagnetism, and effects relevant to the research in the following chapters has been discussed. The motivation for high anisotropy magnetic materials has also been summarized.
- **Chapter 2** discusses the key experimental methods for thin film growth and characterization, with the basic theory of each technique discussed.
- **Chapter 3** presents experimental demonstration of a surface effect in the anisotropy field of $L1_0$ FePt that occurs at nanoscale due to broken symmetry. This effect is explained, and a method to repair the symmetry is presented.

- **Chapter 4** covers the effects of strain and chemical ordering on L10 FePt through the use of synchrotron techniques and first principles calculations.
- **Chapter 5** presents efforts to develop low temperature phase MnBi for STT application by improving the magnetic properties at sub 50 nm thicknesses. In this chapter, I report on an observed capping layer effect that must be considered when growing thin film MnBi.
- **Chapter 6** reports the first experimental demonstration of Ru as a single element room temperature ferromagnet since Fe, Co and Ni, which has been predicted by several theoretical works.
- **Chapter 7** summarizes the work in this dissertation. The outlook for magnetic materials and new spintronic memory technologies is also presented.

Chapter 2. Experimental methods

2.1. Thin films

2.1.1. Growth methods

The rise of high density magnetic recording, GMR, and MTJs is closely tied to the development of capable thin film deposition systems, which intimately related to development of high vacuum systems (pressure of 10^{-6} Torr or better). Even though the underlying principles of common thin film growth technologies go back a century, they are still under development given their extensive use in fields such as magnetic, semiconducting, superconducting, ferroelectric, MEMS, etc. The most common methods for depositing thin films fall (mostly) into two main categories: physical vapor deposition and chemical vapor deposition. These two categories, however, are an umbrella for a variety of specific methods for growing thin films, which are summarized in Fig 2.1 [50]. Each of the methods for thin film growth have their advantages and disadvantages depending on the film growth needs. For example, molecular beam epitaxy (MBE) is able to grow nearly perfectly epitaxial films, but the process is extremely slow which limits it to ultra-thin films and is unusable for many commercial applications. Evaporation and CVD can grow thick films relatively quickly, especially oxides and nitrides, but with relatively low film quality. Evaporation is also limited to materials that have evaporation temperatures that can be achieved from a resistive heater (~1000 °C),

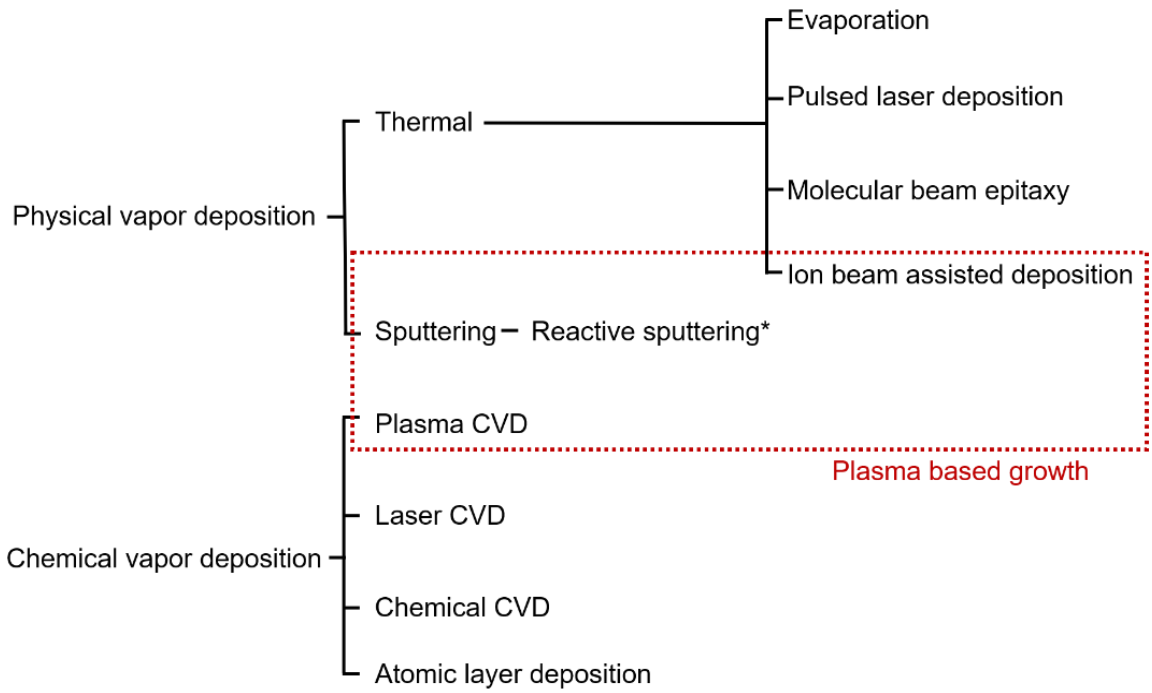

Fig 2.1: Umbrella diagram of common thin film deposition methods.

which rules out common transition metals. Sputtering, which is employed for nearly all thin films in this dissertation, is popular in both industry and academic studies, especially metals, given that it allows for high throughput, highly textured thin films with low surface roughness, wide versatility in materials available to deposit (including alloys), and can be built for relatively low cost given its straightforward design.

2.1.2. Sputtering

Sputtering was first discovered in 1852, but it took another half century for the application in thin films to take seed, and decades more to become a viable technology [51]. In the conventional sputter deposition process, Ar gas is ionized into a plasma in a high vacuum environment, and used to bombarded high energy

ions (Ar^+) at a target made of the desired material. This leads to the target atoms to be ejected, and backscattered towards the substrate. In practice, the target placed on the cathode, and the substrate on the anode, which is often grounded to the chamber, except in the case of biased sputtering. The sputtering rate is increased by using a magnetic field (magnetron sputtering) to increase the concentration of ionized Ar atoms near the surface of the target in a ring like configuration. In this setup, a “south” pole magnet is placed in the center of a disk like cathode (sputter gun) geometry, and a ring “north” pole magnet is along the perimeter of the sputter gun. This magnetic field traps electrons near the target in a racetrack like geometry, which increases the Ar^+ plasma near the target surface by an order of magnitude or more and thus the sputter rate also increases; this is shown in Fig. 2.2. Since the sputtering process is a fundamentally physical process, it can deposit a wide variety of materials and is not limited by evaporation temperatures. Sputtering can occur with a dc or RF source at the cathode, where dc is preferred, but unable to generate plasma for insulating materials (e.g. SiO_2 and MgO), but is generally capable of targets that are electrically conductive. It is also common to include a heater near the substrate, which allows for increased control of the thin film properties during deposition.

Development of alloys through sputtering is common and accomplished through two methods. The first method is to use an alloyed target, with appropriate composition. From a thin film growth point of view, this method is often easier, however, it leaves little room to control the composition, and if the materials making up the alloy have dissimilar sputter yields, the target composition changes over time. The second method is by co-sputtering, where one or more sputter guns are directed at the substrate and the targets are sputtered simultaneously. This method is more difficult, but it allows for the composition to be finely tuned from the sputter yield of each target. In this dissertation, a UHV 8-target sputtering

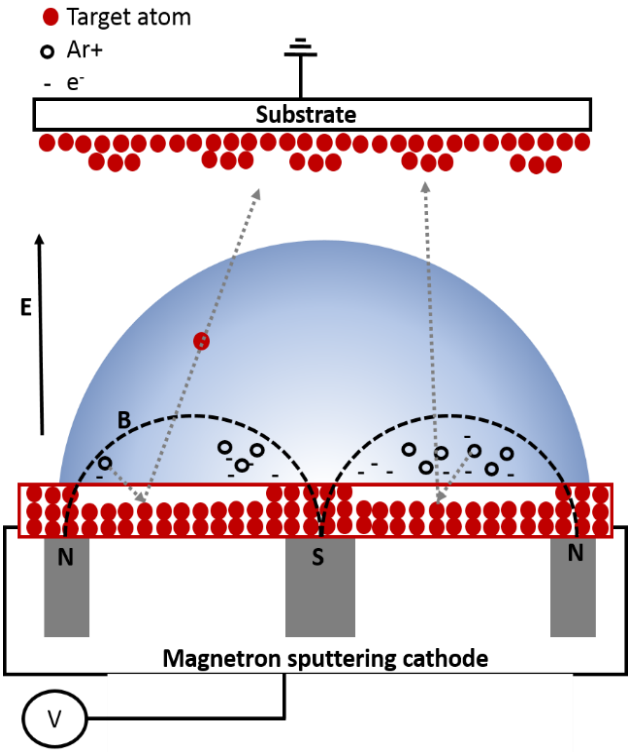

Fig. 2.2: Schematic of magnetron sputtering process. The magnetic field (B) is used to confine the Ar+ and electrons (e^-) near the target surface. The shaded region indicates the plasma. The ejected atoms travel towards the substrate and land on the surface due to the electric field (E).

system with an *in situ* resistive heater is used to grow all thin films in this work, unless designated otherwise.

2.1.3. Thin film nucleation process

Important film properties to control with sputtering, depending on the specific application, include composition, grain size, surface roughness, uniformity, and crystallinity. In hard disk media, high quality magnetic films with well segregated grains are required, but in spintronic memories having a continuous film with low surface roughness is necessary. It is possible to grow both types of thin films using sputtering, however, it requires some knowledge of the thin film growth process. As the atoms kicked off the target land on the substrate, the atoms then diffuse along the surface until 'sticking' at a low energy site. Additional atoms deposited then either agglomerate with existing atoms to form islands, or start a new nucleation for islands. The islands then continue to grow and add atoms until the film is coated. There are three modes of thin film growth: Frank-van der Merwe, Volmer-Weber, and Stranski-Krastanov which are shown in Fig 2.3. Frank-van der Merwe growth is when the film grows in a planar layer by layer order. This occurs when the deposited atoms prefer to bond to the substrate rather than other deposited atoms, and is most commonly observed in single crystal and highly

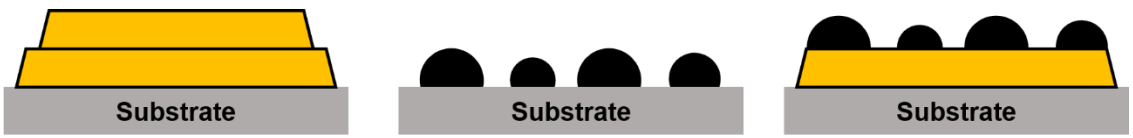

(a) Frank-van der Merwe (b) Volmer-Weber (C)Stranski-Krastanov

Fig 2.3: The three types of thin film growth (a) Frank-van der Merwe (layer), (b) Volmer-Weber (island), and Stranski-Krastanov (mixed).

epitaxial films. Volmer-Weber is an island growth process where the deposited atoms preferentially bind to each other instead of the substrate, and this is common for metals deposited on oxide substrates. Stranski-Krastanov is a mix of island and layer growth. After several layers have grown, islands become more favorable, and is common for deposition of metals on other metals [52]. These three types of thin film growth show the importance of choosing the proper substrate which can be limited based on the application. Important considerations include the surface energy between interfaces, that is to say does the deposited material adhere to the substrate, or is an additional adhesion layer required. Is the growth process meant to be epitaxial? If so then a single crystal (e.g. MgO, Al_2O_3, $SrTiO_3$) substrate is needed, and lattice mismatch calculation between the film and substrate must be done to ensure the strain is not too large. It is also common to

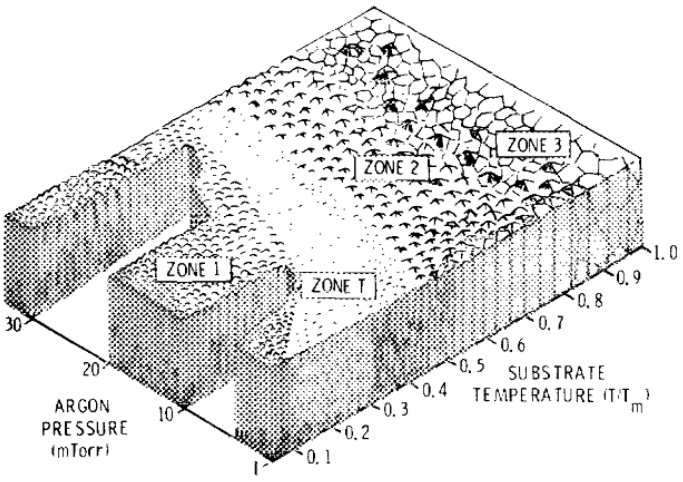

Fig 2.4: Thornton model for effect of Ar pressure and substrate deposition temperature on micro-structure of a sputtered thin film [52]. Reprinted from J. A. Thornton and D. W. Hoffman, “Stress related effects in thin films” Thin Solid Films, 171 5 (1989), with permission from Elsevier.

grow textured thin films on amorphous substrates (e.g. glass and SiO_2). The Ar sputtering pressure and substrate temperature are critical for controlling a sputtered films microstructure, and their dependence is shown in Fig 2.4 from the Thornton zone model [53]. High temperature growth generally leads to increased grain size and can often induce improved texturing since the surface diffusion is enhanced during deposition.

2.2. Magnetometry

A magnetometer is the standard method for measuring magnetic moments, there are several common variations on this tool, in order of increasing sensitivity: vibrating sample magnetometer (VSM), alternating gradient magnetometer (AGM), and superconducting quantum interference device (SQUID) magnetometer. The SQUID provides the highest resolution (10^{-7} emu), but requires superconducting magnets, which makes it a far costlier system than a VSM or AGM, and SQUID measurements can take up to a full day for the same measurement that a VSM can complete in 10 minutes. A schematic method for the VSM is shown in Fig 1. A M-H hysteresis loops can be measured by sweeping an external magnetic field from $+H_{sat}$ to $-H_{sat}$ and back while measuring the magnetic moment. In thin films M_s is calculated dividing by the total sample area and total ferromagnetic thin film thickness, which is often the largest source of error when determining the magnetization. The VSM is the dominant tool used in this dissertation for collection of this work; the working principle is that a pair of magnetic poles are used to magnetize a sample. Then the sample is set to vibrating, which generates a

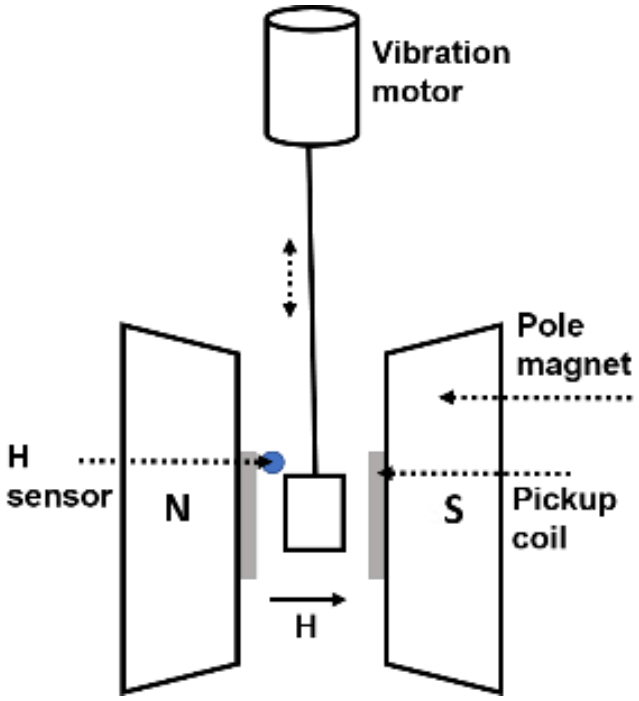

Fig 2.5: Schematic of a vibrating sample magnetometer (VSM).

voltage (V_{coil}) in a pair of pick up coil, as shown in Fig. 2.5. V_{coil} is a function of the sample magnetic moment (*m*), amplitude of vibration (*A)*, coupling constant (*C*), and vibration frequency (ω). The sample holder and substrate will contribute a diamagnetic or paramagnetic signal to the measured curve, and in thin films can be quite dominant. Provided the sample can be fully saturated this background can be subtracted out and is generally done for all plots in this work unless it is noted otherwise.

2.3. X-ray diffraction

One of the most common methods to characterize the crystal structure of materials is with x-ray diffraction (XRD) by measuring the interplanar spacing of crystals, which relies on the Bragg condition:

$$2d_{hkl}sin\theta = n\lambda \quad (2.1)$$

Where λ is the wavelength of the x-ray source, commonly Cu or Co Kα, 1.54 and 1.79 Å, respectively. θ is the incident x-ray angle, d_{hkl} the interplanar spacing between (hkl) planes, and n the order of the reflection. The geometry underlying the Bragg equation can be seen in Fig 2.6 as well as the sample and x-ray geometry for a typical diffractometer. XRD allows for detailed understanding of a thin films crystallographic phase, epitaxial growth mechanism, strain, relaxation and film quality. The symmetric Bragg condition is sensitive only to the lattice parameter aligned perpendicular to the substrate, grazing parallel, and asymmetric is sensitive to both, with each demonstrated in Fig 2.7. In non-textured structures, commonly known as 'powder diffraction', the orientation of the x-ray source and detector only need to in the symmetrical reflection geometry (Fig 2.7) since all available Bragg conditions are available in a sample with random crystallographic orientation. This is completed by measuring a θ-2θ coupled scan, with the incident x-rays aligned such that ω is perpendicular to the substrate characteristic peak,

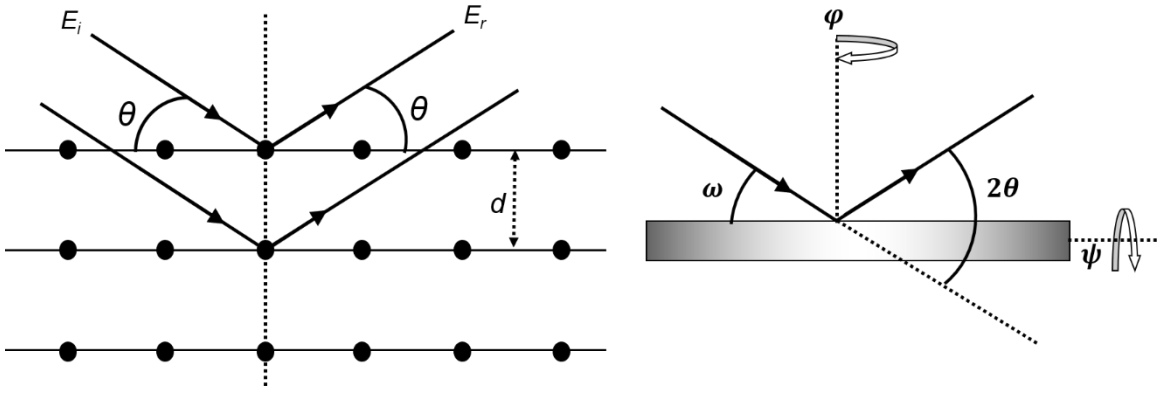

Fig 2.6: (a) Set up for Bragg condition, which forms the theoretical basis for XRD, and (b) the experimental configuration.

where ω = 2θ x ½ + offset for the scan. In textured thin films, characterization becomes more complex, as a simple θ-2θ symmetrical reflection scan does not necessarily provide adequate information. Using the full-width-half-max of a diffraction peak, XRD can also be used to estimate a limit of the grain size using the Scherrer formula:

$$\tau = \frac{0.9\,\lambda}{\beta \cos\theta} \tag{2.2}$$

Often, even in highly textured samples, there are slight misalignments between grains due to the nucleation process, and this is known as mosaic spread. By fixing 2θ, and varying ω a rocking curve is collected, and the mosaicity can be characterized as well as film curvature. To find information about the in-plane lattice parameters, the grazing incidence configuration is employed, where the incident x-ray is applied only slightly off from parallel to the film surface, which requires use of a point-source incident x-ray. While in the grazing incidence

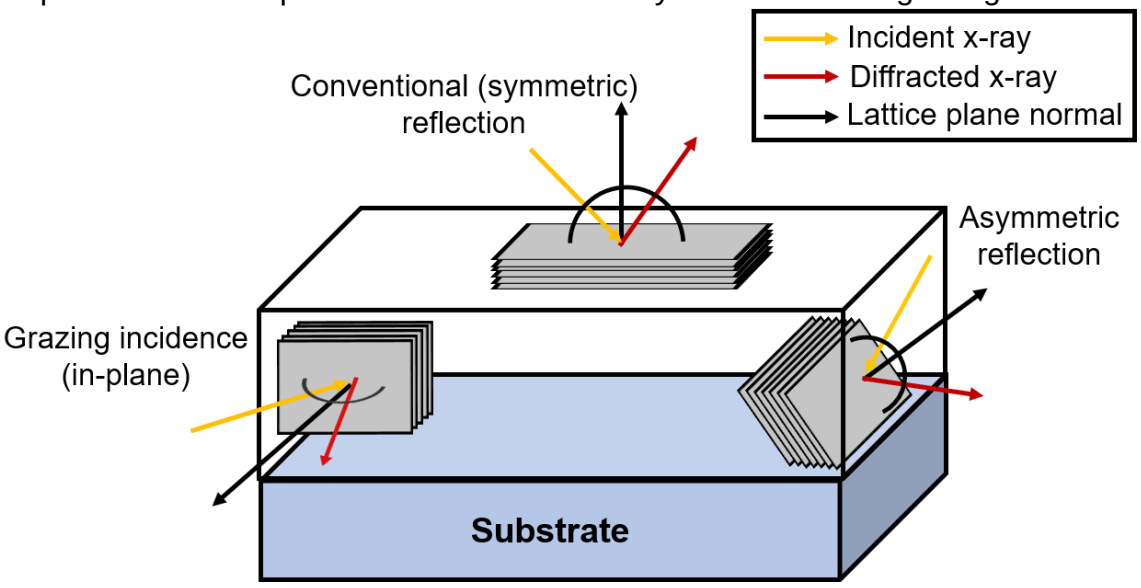

Fig 2.7: Schematic of various x-ray diffraction measurement geometries.

condition, the sample can be rotated 360° which can show the symmetry of the substrate and thin films, along with any rotation between the growth planes. An example of this can be seen in chapter 6 concerning the detailed analysis of the epitaxial growth mechanism for samples discussed.

2.4. X-ray reflectivity

X-ray reflectivity (XRR) is a technique in thin film characterization that can provide film thicknesses, surface roughness, interface roughness in multilayers, and the lattice density. XRR can be advantageous over more 'direct' probes of the surface (i.e. AFM and surface profiling) since direct methods tend to be at small length scales, where XRR can provide the average roughness over large sample regions. XRR can be thought of as analogous to the classical Snell's law problem in basic optics, where at an interface an incident beam has a reflected and transmitted component. Since similar reflectometry methods are utilized with neutrons, it is common to refer to the scattering in q space rather than θ, since q is generalized to any wavelength, where q is defined as:

$$q = \frac{4\pi \sin\theta}{\lambda} \tag{2.3}$$

Because the frequency of the x-rays for typical sources in experiments is so high, the x-ray interaction with a crystal can be described in a classical form [54]. The set up for a one-dimensional XRR problem is shown in Fig 2.8.

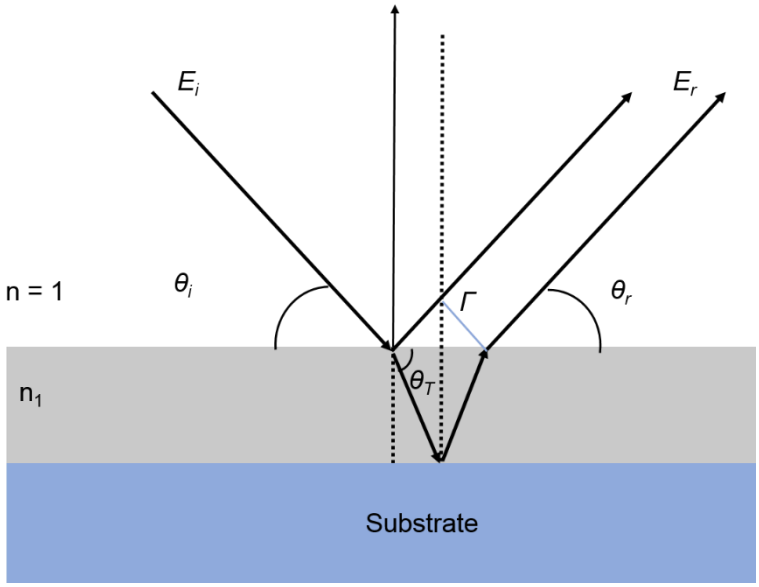

Fig 2.8: Schematic of x-ray reflectivity for a single thin film grown on a substrate.

Where the index of refraction for x-rays is:

$$n_1 = 1 - \delta - i\beta \tag{2.4}$$

δ and β are due to the dispersion and absorption of the materials, respectively, and are:

$$\delta = \frac{r_e}{2\pi}\lambda^2\rho \tag{2.5a}$$

$$\beta = \frac{r_e}{2\pi}\lambda\mu \tag{2.5b}$$

Where r_e is the classical electron radius (2.81 x 10^{-5} Å), λ is the incident x-ray wavelength, ρ the electron density for the material, and μ is the linear absorption coefficient. From Snell's law we can say (n of air is 1):

$$n_{air}\cos\theta_i = n_1\cos\theta_T \tag{2.6}$$

There is a critical incidence angle (θ_c) where there is total external reflection of the incoming x-rays, which occurs when $\underline{\theta_T}$ = 0. β is usually small enough to disregard and by taking small angle approximation for *cos* θ, a critical angle can be written as:

$$\theta_c = \sqrt{2\delta} \tag{2.7}$$

Each interface has a partially reflected beam, with distance between the two of Γ, which gives rise to interference with constructive and deconstructive maxima and minima. The resultant interference oscillations are known as Kiessig fringes. The angle between Kissieg fringe maxima and θ_c can be shown to be:

$$\theta - \theta_c = m^2 \left(\frac{\lambda}{2d}\right)^2 \tag{2.8}$$

Where *d* is the film thickness and with peak order denoted by the integer 'm.' Thus by plotting the angle of each Kiessig fringe maxima vs m^2, the slope can then be used to calculate the film thickness to a high degree of accuracy. There is also an intrinsic dependence of the reflectivity on *q* (or θ), which scales approximately as:

$$R(q) \propto \frac{1}{q^4} \tag{2.9}$$

Thus far it has been assumed that samples have a perfectly smooth surface roughness, but this cannot be ignored since surface roughness has a significant effect on the intensity of the reflectivity. A film with roughness σ decreases in intensity as described by a Debye-Waller factor:

$$R_{roughness} = R_0 e^{-q^2\sigma^2/2} \tag{2.10}$$

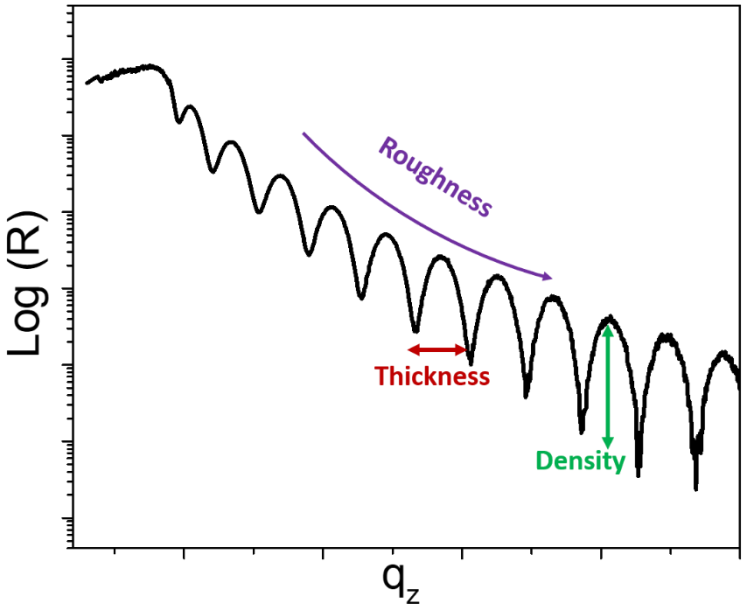

Fig 2.9: Example of an experimental XRR curve, which the effect of thickness, roughness, and lattice density on the curve.

Because of the strong dependence of roughness and intensity on *q*, reflectivity curves are often limited in signal to low *q* except in thin films with ultra-smooth surface and interfacial roughness. Fig 2.9 shows a XRR curve for a highly textured Mo thin film on a sapphire substrate to qualitatively demonstrate how changes in thickness, roughness and density effect R(q). In practice, the film thickness can be determined from just the fringe peaks or valleys, but in order to gather information about the density and layer roughness' simulation software such as GenX [55] is required.

2.5. Synchrotron techniques

A synchrotron provides the availability of x-rays with wide energy range, ability for light polarization, element specific measurements and time scale resolution make studies using a synchrotron powerful in probing fundamental

magnetism. There are many synchrotron techniques with a wide variety of applications beyond magnetism, and acronyms forming an alphabet soup, but this work will focus on the three techniques used in this dissertation: x-ray absorption spectroscopy (XAS), x-ray emission spectroscopy (XES), and x-ray magnetic circular dichroism (XMCD). XES and XAS at the most basic level come from energy associated with the transition of electrons between shells, and so it is useful to define the terminology. Fig. 2.10 illustrates the relevant transitions, and their name (e.g. K_α, L_β, etc). The first letter denotes the principle quantum number (*n*) that the electron is transitioning to (emission) or exciting from (absorption), and a subsequent Greek letter refers to the difference in *n* from initial state to final; for example, going from n=3 (M shell) to n=1 (K shell) is the K_β transition. The transitions are of course limited to the allowed transitions from the quantum

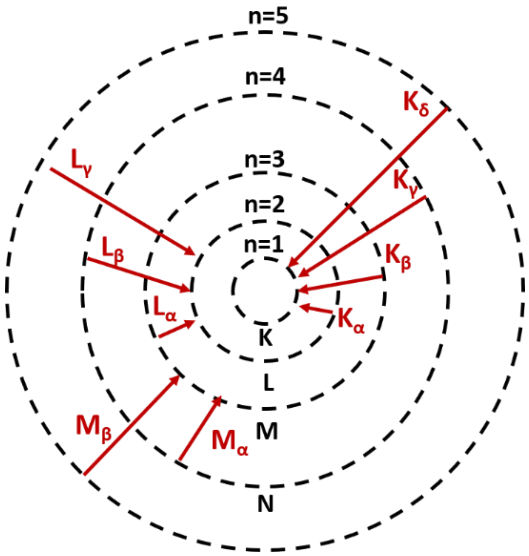

Fig 2.10: Electron transitions and their associated name of the edge. The arrows are for an emission process, but absorption is simply reversed direction.

mechanical selection rules. In addition, the energy required for the various transitions is element specific.

2.5.1. X-ray absorption spectroscopy

XAS occurs when incident x-rays are injected into an atom at the proper energy to excite a core electron to transition to a higher energy unoccupied state. The electron can also be completely removed from the atom, which is known as a continuum state. XAS provides insight into the unoccupied states of an orbital, and so can provide detailed insight into the oxidation state and bonding of the element that is excited. XAS on the *L*-edge is useful for probing the magnetic 3*d* occupancy of transition metals. For example, in the case of $L1_0$ FePt, XAS on the L_2 and L_3 edges has been used to examine the oxidation state of Fe (2+ vs 3+), and the chemical ordering [56], where the L_2 and L_3 edges are defined as:

$$L_2: 2p_{\frac{1}{2}}\ to\ 3d_{\frac{3}{2}}$$

$$L_3: 2p_{\frac{3}{2}}\ to\ 3d_{\frac{5}{2}}$$

Commonly XAS is broken up into two regions: the x-ray absorption near edge spectroscopy (XANES) an extended x-ray absorption fine structure (EXAFS). A sample XAS curve collected around the Fe absorption is shown in Fig 2.11, which the XANES and EXAFS regions noted [57].

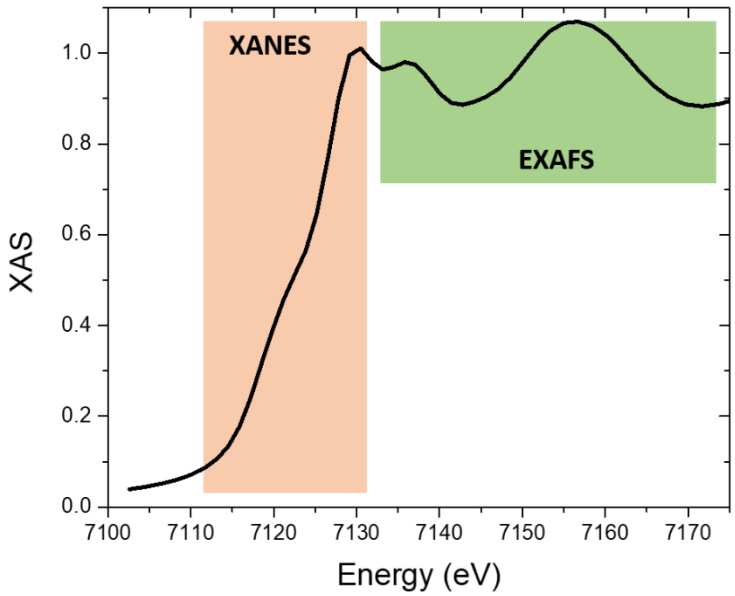

Fig 2.11: Example of a simulated XAS scan on the Fe edge for $L1_0$ FePt.

2.5.2. X-ray emission spectroscopy

XES occurs when an electron drops to fill a lower shell, and in the process emits a photon. XES is often considered a secondary process to XAS because the emission process happens as a consequence to absorption. After the XAS process, discussed in preceding section, there is a vacancy for an inner shell electron, and so a higher shell electron drops down to fill this state [58]. XES provides detailed insight into the occupied electron states and in particular the spin-orbital (*Kα*) and electron-electron interactions (*Kβ*). In the case of the Fe *Kβ* (3*p* → 1*s*) emission, the number of unpaired spins can be observed experimentally, which allows for studies of high vs. low spin states in magnetic materials. The *Kβ* spectra emission is mainly due to the interaction of the 3*p* hole and electrons in the partially filled 3*d* states. The *Kβ* emission is affected by the spin state—when

the state is $3p^{\uparrow}3d^{\uparrow}$ there is a singular main peak, known as $K\beta_{1,3}$, but when the state is $3p^{\downarrow}3d^{\uparrow}$ an additional emission appears at slightly lower energy known as the $K\beta'$ satellite emission [59,60].

Since XAS and XES are such complementary techniques, it is possible to combine both methods into what is known as resonant inelastic x-ray scattering (RIXS). RIXS allows for probing more interactions than traditional XES since the added intermediate resonant state allows magnetic excitations to be studied since the two-step process allows for transitions that are forbidden by the transition rules in XES. This however complicates the interpretation of RIXS data in practice due to the convolution of many processes. RIXS is a method growing in popularity since it is now more feasible due to higher photon fluxes from modernized synchrotrons. Due to the complexity of the RIXS process, the theory will not be discussed in this dissertation, but Luuk et al have made a thorough summary of the underlying physics, and potential of the technique [61]. In RIXS the incident photon energy is measured, which starts the absorption process, along with the energy transfer of the scattered photon from the emission process. The incident energy dependence of the fluorescence provides insight into the 3*d* orbital population, where the energy transfer dependence probes changes in charge and spin density.

2.5.3. X-ray magnetic circular dichroism

X-ray magnetic circular dichroism (XMCD) allows for direct measurement of element specific magnetic moments. This is done by measuring two XAS spectra

using right and left circularly polarized x-rays to a magnetized sample. And it is especially valuable for looking at element specific ferromagnetism, for example, it can be used to rule out magnetic contamination by tuning to the element specific absorption energy, and isolate element specific magnetic properties in compounds (e.g. tune to Fe absorption energy when measuring an FePt film). XMCD can also be used to experimentally extract the orbital and spin moment contributions, however, in practice the extracted values can have rather large error [62].

2.6. Electron microscopy

One of the most powerful tools in characterization of materials at nanoscale is the transmission electron microscope (TEM), and the closely associated scanning transmission electron microscope (STEM); both techniques can be measured in the same instrument, and so the terms are often used interchangeably. In a TEM, a beam of electrons, collimated and focused with magnetic lenses, are transmitted through a sample that is electron transparent (less than 100 nm) and projected onto a screen or camera. Since the electron beam is transmitted through the sample, TEM imaging is sensitive to the crystal structure, composition, and magnetic field of the sample. Modern day high resolution TEMs can reach angstrom level resolution, and *in situ* measurements are possible. A schematic of the TEM column in Fig 2.12 shows the path of the electron beam [63]. A major difficulty in TEM studies is the sample preparation, however, with recent advances in focused ion beam (FIB) techniques, the process is easier than ever.

The TEM can be used in imaging or diffraction mode. When in imaging mode, a high-resolution image of the sample (bright field) which can show information about texturing, grain alignment, and interfaces in detail; it is also contrast sensitive to the atomic number ('z contrast') of the materials imaged. Diffraction mode provides additional information about the crystal structure, which requires aligning to a known zone axis (analogous to crystal plane) for accurate analysis, about

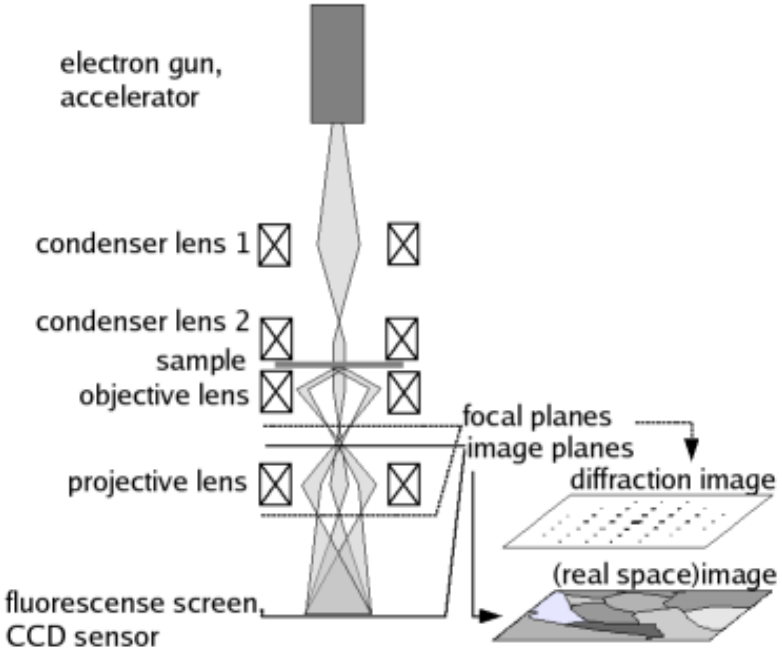

Fig 2.12: Schematic of a typical transmission electron microscope [63].

lattice spacing, distortion, and even element relative element location. Diffraction TEM however is not a replacement for XRD since XRD is more sensitive to lattice parameters, and provides crystallographic information across large regions of a sample, where TEM is a local measurement. XRD is also a much faster technique to complete in general. Furthermore, STEM characterization of crystal structure can be limited in multi-phase samples since the electron beam transmits through

the entire sample, competing phases will have differing zone axes which can make the analysis significantly more difficult, even impossible, compared to XRD characterization.

Chapter 3. Observation and elimination of broken symmetry in $L1_0$ FePt nanostructures

*Reprinted from P. Quarterman, Hao Wang, Jiao-Ming Qiu, Honghua Guo, Bin Ma, Xiaoqi Liu, and Jian-Ping Wang. “Observation and elimination of broken symmetry in L10 FePt nanostructures” Appl. Phys. Lett. 107, 232401 (2015) with the permission of AIP Publishing.

3.1. Introduction

Surface magnetism has inspired tremendous interest since the early work of Louis Néel [64] and remains an important research topic [65]. As nanostructured materials continue to become more relevant, the effects of surface atoms need to be considered because surface atoms are no longer a negligible portion of the volume. From a technological standpoint, surface effects on magnetic phenomena will play a key role in the continued down scaling of feature sizes in HAMR, bit pattern magnetic recording [22] and spintronic memories and devices [66]. Despite the increasing importance of surface magnetism, few results have been reported on the direct measurement of the surface anisotropy of magnetic nanoparticles because of accessibility issues [67]. Consequently, most of the treatments of surface effects have been done theoretically [68], except for special thin film cases—in which large and repeatable surfaces can be constructed experimentally [69,70]. Unfortunately, in the case of nanoparticles, it is even difficult to determine the direction of the magnetic easy axis on the surface [71].

Simulation results have shown that the surface contribution of magnetic nanoparticles depends on both the orientation and magnitude of surface anisotropy, while the latter is usually an estimation based on the strength of the exchange interaction [72].

As discussed in chapter 1, $L1_0$ FePt is a promising candidate for use in HAMR media [16,22–24] and spintronic devices [26]. This is largely due to its large MCA of 7×10^7 erg/cm^3. It has been well accepted by magnetic research community and magnetic recording industry that the large bulk anisotropy could keep the magnetization direction thermally stable at a size as small as 3 nm in diameter before becoming superparamagnetic [22], however, this size calculation is based on the assumption that the MCA is independent of particle size, and any particle size reduction will not induce additional physical effects on the magnetic performance. Unfortunately, this is not a valid assumption because roughly half of all the FePt atoms are on the surface for a 3 nm particle, and so significant surface effects should be expected due to broken symmetry along the surface. We suggest this surface effect will significantly impact the magnetic properties of FePt based on previous reports of FePt nanostructures. $L1_0$-FePt has been chosen to study surface effects in this work since the well-ordered magnetically hard phase can be grown well using multiple methods, and combined with it being thermally stable at sizes in which surface effects are significant. In this chapter, first we report our experimental observation of the surface anisotropy effect in $L1_0$ FePt nanoparticles and $L1_0$ FePt thin films with island structure. Then we propose, and experimentally

demonstrate, an approach to eliminate this surface anisotropy effect by repairing the broken symmetry.

3.2. Demonstration of surface effect on MH loop in $L1_0$ FePt nanostructures

$L1_0$ FePt nanoparticles were prepared using a gas-phase condensation technique [73], which can selectively make mono-dispersed single-crystalline FePt nanoparticles with either A1 or $L1_0$ phases [74,75].The octahedral shape is clearly visible from the TEM image in Fig. 3.1a, and was used to create The 3-D particle model, shown in Fig. 3.1b, which illustrates the packing sequence of Fe and Pt atoms; all the surface atoms sit on (111) planes which are most closely packed to obtain the lowest surface. At this size, surface atoms on the eight equivalent (111) planes have an overall volume fraction of 28.3 [73,74,76]

The magnetization reversal process of $L1_0$ FePt nanoparticles was measured, as shown in Fig. 1c—the measurement field was applied parallel to the easy axis direction. As shown in Fig. 3.1c, the sample has a coercivity value of 33.4 kOe at a measurement temperature of 5 K. Clearly, there is a ‘kink’ in the hysteresis loop near the zero-field region. Similar behavior has been found for: highly ordered FePt particulate films [77], octahedral-shaped FePt nanoparticles formed using FePt and MgO alternate deposition [78] at substrate temperature as high as 780 °C [79], and FePt-Ag-C recording media fabricated at 550 °C [80].

The observed 'kink' has been completely ignored and previously attributed to the existence of poorly ordered phase due to size effect [81], but surface effects were not taken into account. However, considering all the FePt samples listed above were highly $L1_0$ ordered, it is more likely that the 'kink' came from surface spin reversal governed by the surface anisotropy contributions. In addition, Zhou,

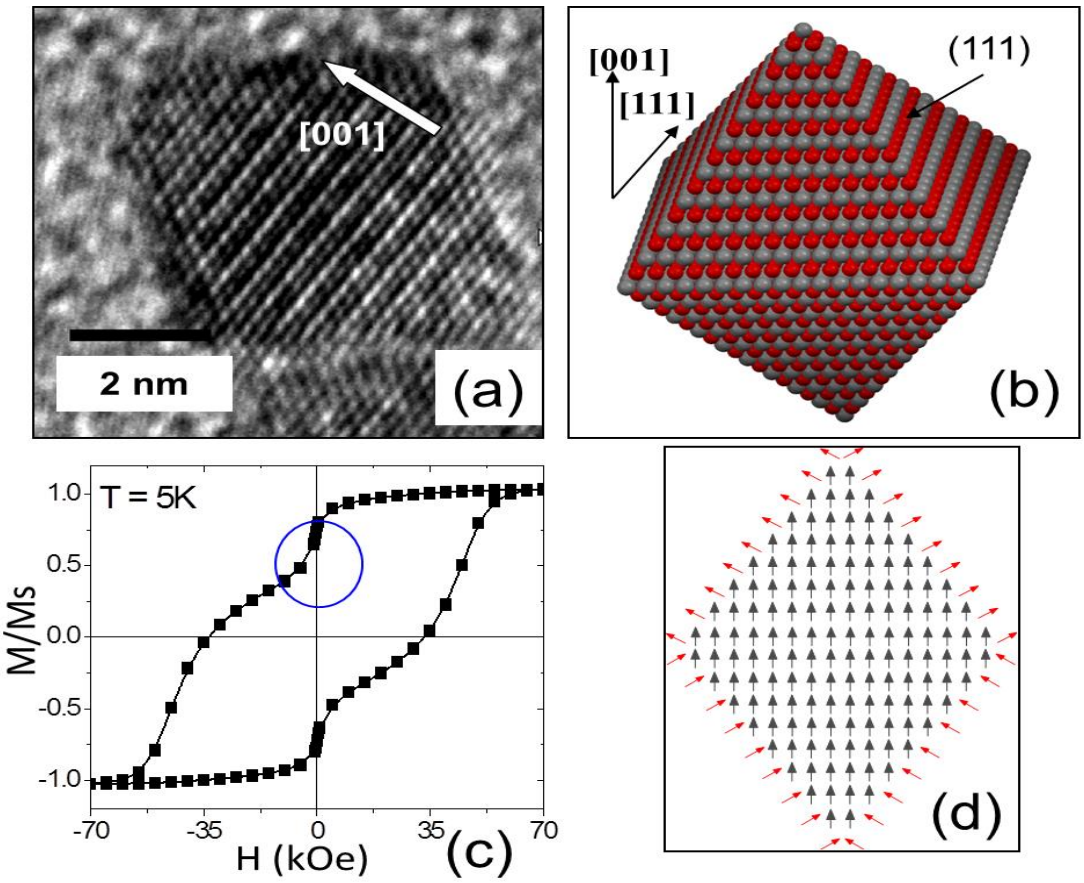

Fig 3.1: Directly ordered $L1_0$ FePt nanoparticles prepared using a gas-phase aggregation technique at room temperature. [16] (a) TEM image of one chemically ordered particle with its c-axis (the magnetic easy axis) lying in-plane (b) a 3-D atomic reconstruction of the $L1_0$ FePt particle. (c) Hysteresis loop of 30 layers of mono-dispersed $L1_0$ FePt nanoparticles, with a coercivity of 33.4 kOe at temperature of 5 K. (d) The remanent state of one octahedral $L1_0$ FePt nanoparticle. Here arrows represent the spins from iron atoms and all platinum atoms have been omitted for clarity. Red arrows are surface spins and black arrows are interior spins, respectively.

Skomski and Sellmyer simulated FePt grains using the core shell model in which the hard FePt grains are surrounded by a soft phase, and no such kink was found to exist [82]. These surface spins experience an anisotropy associated with the broken symmetry of their crystal environment, and when this surface anisotropy is comparable to, or larger than the exchange coupling interaction, the surface spins will favor a full alignment along the surface anisotropy direction. Consequently, there will be jumps on magnetization curves [83]. The validity of the surface anisotropy assumption also lies in such an understanding that the bulk anisotropy energy in an FePt system is not simply a result of the Néel model or directly due to tetragonal distortion. Instead, the magnetocrystalline anisotropy energy comes from the polarization of the Pt 5*d* electrons by the Fe 3*d* electrons, and the strong spin-orbit coupling in 5*d* electrons of Pt [27]. Every Fe atom in the interior part of the nanoparticle has eight Pt atoms as its nearest neighbors, but surface Fe atoms have at most six Pt atoms as nearest neighbors as shown in Fig. 1b, four of which are surface Pt atoms. Therefore, the symmetry between Fe and Pt is differs from the interior to the surface. Since each surface has a different normal direction, which is structurally associated with the broken symmetry, each surface should have its own anisotropy direction. This may cause atoms on different surfaces to also have different remanent states, as shown in Fig. 3.1d. Also, the exchange coupling in the surface portion has to be relatively weak, otherwise the surface spins would be coupled with the internal spins, and there would be no kink in the hysteresis loop.

It is also not possible for a kink to be formed by dipole-dipole interactions. If the grains are strongly coupled via the dipole interaction, then the grains will switch more coherently than if decoupled thus increasing the ‘squareness’ of the loops, but will not result in a partial switch that is necessary for a kink in the MH loops. A micromagnetics simulation package (OOMMF) [84] was used to observe effects on the hysteresis loops of a one dimensional chain of FePt grains separated by a non-magnetic matrix when the strength of the demagnetization field was varied, which is equivalent to changing the dipole-dipole interaction strength, and no such kink was observed in the hysteresis loops.

Based on the discussion above, the most direct approach to confirm and overcome this surface effect is to epitaxially cover the particle surface with Pt. However, it is difficult demonstrate this process using nanoparticles, because it is not only necessary to embed the particles in a Pt matrix, but also induce epitaxial growth at the interface between the FePt nanoparticles and Pt matrix. Thus in the following sections, $L1_0$ phase FePt thin films with well-dispersed FePt islands on MgO substrate were prepared to address the challenge. Since the ‘kink’ has been observed in thin films of FePt islands, as shown in Figure 3, there should be no issue with using thin films instead of nanoparticles to demonstrate the surface effect.

3.3. Demonstration and removal of surface effect in FePt nano-island

It was confirmed that a ultra-thin FePt film formed island-like structure when deposited on single crystal MgO (100) substrate at high temperature [78,85,86] which is predicted based on the Volmer-Weber nucleation model that commonly occurs for metal on oxide growth. An FePt island is cartooned in fig. 3.2a; the island

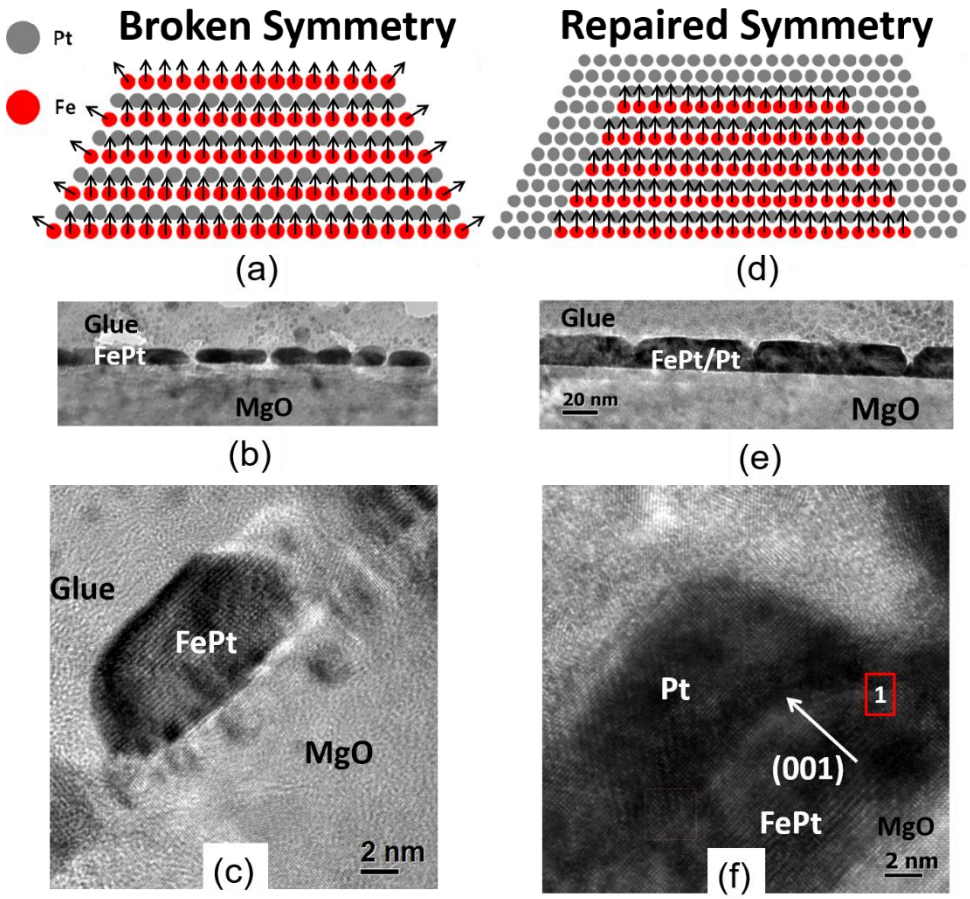

FIG. 3.2: (a) The schematic of an FePt island with (001) texture. (b) The TEM cross-section image of a $L1_0$ FePt island-structural film. (c) The zoom-in cross-section image of a single FePt island, which matches the model in (a). (d) The model for FePt islands epitaxially covered by Pt atoms. (e) The TEM cross-section image of FePt/Pt(8nm) island-structural film. (f) The zoom-in cross-section image of a single FePt/Pt(8nm) island. Region 1 is located at the top of an FePt island. The enlarged and filtered images of region 1 (top part) are shown in the inset to confirm the epitaxial growth and lattice match of Pt on FePt.

has a (001) texture, which was induced by MgO. The islands have a uniaxial anisotropy with an easy axis perpendicular to the film plane. Similar to the (111) surface of FePt nanoparticles, the side wall of FePt islands also have broken symmetry and a 'kink' should be observed in its hysteresis loop. Furthermore, to fix the broken symmetry, we propose coating the FePt islands with a Pt thin film that completely covers the FePt surface, as shown in Fig. 3.2d. Pt has been proposed to repair the symmetry because FCC Pt films closely lattice matches with $L1_0$ phase FePt and can epitaxially grow on top of FePt [87].

The samples were prepared using an eight-target ultra-high vacuum magnetron sputtering system. First, a single crystal MgO substrate was heated to 500 °C, and then an FePt film with 4 nm nominal thickness was deposited at the same temperature. The TEM cross-sectional images of the FePt film are shown in Fig. 3.2; TEM cross-sectional image in Fig. 3.2b reveals an island-like structure for the as-deposited $L1_0$ FePt film, and the average diameter of these islands is 14 nm with a mean height of 7 nm. The distance between two adjacent islands is on order of a few nanometers. Fig. 3.2c displays the zoom-in cross-sectional image of a single $L1_0$ FePt island, which exactly matches the schematic model in Fig. 3.2a. Two other samples were then prepared by depositing Pt on top of the as-deposited island-like FePt film after cooling the samples down to room temperature because of concerns about inter-diffusion between FePt and Pt layers. The layer structures of these two samples are MgO sub/FePt(4 nm)/Pt(3 nm) and MgO sub/FePt(4 nm)/Pt(8 nm), respectively. The TEM cross-sectional images of FePt(4

nm)/Pt(8 nm) sample are shown in Fig. 3.2e, and a zoom in of the FePt/Pt island can be seen in Fig. 3.2f.

As shown in Fig. 3.2e, the islands became much larger (~30nm) after coating with an 8nm-Pt layer because the Pt layer was so thick that adjacent FePt islands were connected by Pt. A single FePt/Pt island is enlarged in Fig. 3.2f, wch confirms that the surface of an FePt island is covered by Pt. Region 1 of Fig. 3.2f is enlarged and filtered in the inset to confirm the epitaxial growth and lattice match between Pt and FePt. The TEM images shown in Fig. 3.2 clearly suggest that the FePt/Pt sample matches the model, which was proposed earlier and is illustrated in Fig. 3.2a and Fig. 3.2d.

The XRD spectra and hysteresis loops of all three samples are displayed, and compared, in Fig. 3.3. The $L1_0$ ordering and (001) texture of FePt was confirmed, as shown in Fig. 3.3a; after coating a 3 nm Pt layer on top of the FePt islands, Pt (200) and Pt (111) peaks appear, but are relatively weak. Both of these two peaks become much stronger, after increasing the thickness of Pt layer to 8 nm, which suggests that Pt layer has two regions that possess different textures. When deposited on MgO/FePt film at room temperature, the FePt film has an island-like structure, and the surface of MgO substrate exposes between adjacent FePt islands, however, when the Pt layer was deposited, it covered not only the surface of FePt islands, but also the surface of the exposed MgO substrate. Without substrate heating, the epitaxial growth of Pt layer cannot be guaranteed; as a result, the Pt layer formed (111) textured on exposed MgO surface, while formed

(001) texture on (001)-textured FePt island surface and displayed (200) peak in XRD spectrum.

The existence and removal of the kink is most clearly shown with the hysteresis loops in Fig. 3.1 and Fig. 3.3, respectively, which supports our proposed model of broken symmetry. The coercivity of FePt, FePt/Pt(3 nm), and FePt/Pt(8 nm) are 13.5 kOe, 15 kOe and 17 kOe, respectively, but the hysteresis loop of the pure FePt sample has an obvious kink. Although a kink is visible in the hysteresis loop of FePt/Pt(3 nm) sample, it is much smaller than the kink of pure FePt sample's hysteresis loop, and as expected, the kink disappeared in the hysteresis loop of FePt/Pt(8 nm) sample. Since the FePt film formed an island-like structure, the superficial area of the sample is much larger than that of a flat surface. The Pt layer with 3 nm nominal thickness cannot completely cover the sample surface, and so the kink became weaker, but was not removed. However, after increasing

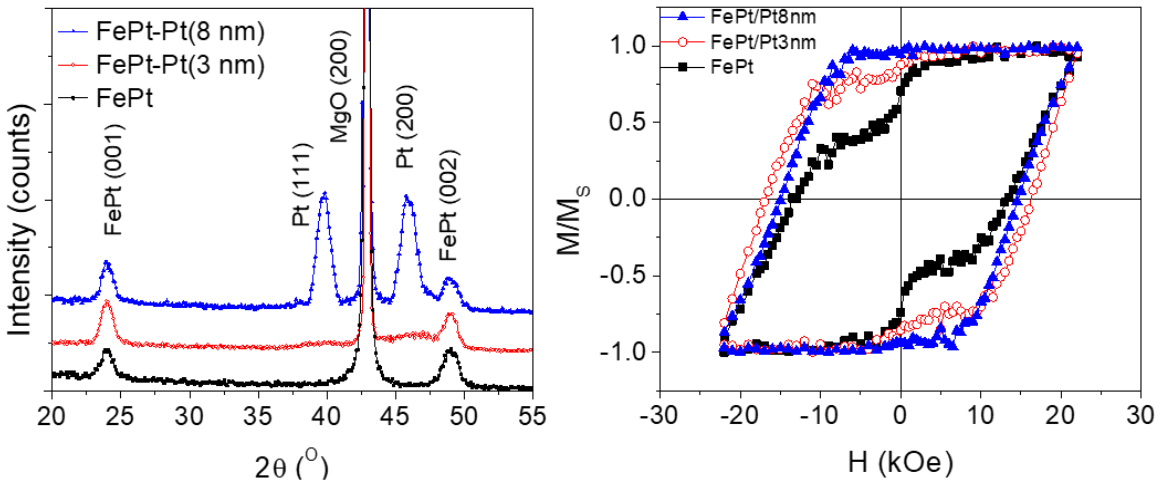

Fig. 3.3: (a) XRD spectra of FePt, FePt/Pt(3 nm), and FePt/Pt(8 nm) samples. All of them show strong (001) texture and $L1_0$ ordering of FePt. Pt layer has both (200) and (111) texture. (b) The hysteresis loops of all three samples.

the nominal thickness of Pt layer to 8 nm, all the surface of FePt and MgO are covered, and the kink of the hysteresis loop was completely eliminated.

3.4. Discussion

The disappearance of the kink in the hysteresis loops after coating the FePt islands with a Pt layer leads us to propose the following:

(1) The surface portion looks soft magnetic or superparamagnetic. The direction of surface anisotropy is related to the surface plane normal due to the broken symmetry. When considering a macroscopic view in the case of the nanoparticles this leads to surface normal pointing in countless surface plane directions since the nanoparticles are not orientated uniformly like the nanoislands. Therefore, the surface portion of the whole sample has a randomly oriented anisotropy. Thus, a behavior similar to a superparamagnetic material was observed in macroscopic measurement.

(2) The exchange coupling between internal atoms and surface atoms is weak, but it became stronger after fixing the broken symmetry. There has been no report about the exchange coupling constant for a monolayer, or several atomic layers, of FePt films. It has been reported that the exchange constant in 14 nm thick epitaxially grown $L1_0$ FePt film is about 1×10^{-6} erg/cm [88] or 2×10^{-14} erg/atom. However, the exchange constants in ultra-thin films can be much smaller than that in thick films or bulk phases. The surface atoms are exchange coupled by fewer neighbors compared to the internal atoms, therefore, the exchange constant at the surface is smaller than in the bulk of the island. The Pt layer coating

the FePt islands causes all of the Fe atoms to become internal atoms, which repairs the symmetry. However, it must be noted that even with the capping layer, the atoms near the FePt/Fe interface have two more Pt neighbors (at the same atomic layer) than the internal Fe atoms. Since the anisotropy of $L1_0$ FePt is caused by the 5*d* electrons in Pt, which are polarized by Fe, the anisotropy orientation at the lateral interface between FePt and Pt is still different from the film plane normal. The disappearance of the kink is likely due to an enhancement of the exchange coupling between the internal and surface magnetic spins.

Lastly, during the preparation of this work for submission, Lv et al. have independently shown that in nanostructures the easy axis can change, and a reduction in magnetic anisotropy can occur by use of DFT calculations [68].

3.5. Summary

In conclusion, we provided an experimental evidence of the existence of surface anisotropy in both 5.8 nm octahedral $L1_0$ FePt nanoparticles and $L1_0$ FePt thin film with island nanostructures. Surface spins are decoupled from the internal spins due to the broken symmetry at surface, and so surface spins switch independently upon applying reversal magnetic field. The surface effect was overcome by coating an epitaxial Pt layer on the FePt islands. The origin of the kink in hysteresis loop is not only due to the surface anisotropy, but also the weak exchange coupling between surface and internal atoms. By converting the surface atoms into internal atoms, their exchange coupling is enhanced, and the kink disappeared. The method could be useful in ultra-high density FePt recording

media, in which the surface atoms of each FePt grain may play an important role in magnetic reversal.

Chapter 4. Effect of strain and chemical ordering on the spin state of $L1_0$ FePt

*Reproduced from manuscript "*Effect of strain and ordering effects on the spin state of $L1_0$ FePt*" by P. Quarterman, Rudra Bannerjee, Michelle E. Jamer, Jinyu Deng, Chengjun Sun, Alpha T. N'Diaye, Jingshen Chen, Biplay Sanyal and Jian-Ping Wang. which is under revisions based on reviewer comments from Phys. Rev. B.

4.1. Introduction and motivation

The effects of an applied strain on magnetic materials have long been studied and realized in applications by either minimizing or maximizing these effects depending on the application. Many applications utilize strain to modify the magnetocrystalline anisotropy energy (MAE) of materials by using seed layers and ferroelectric materials, and the former has long been taken advantage of in the magnetic recording industry [30], while the latter is an important topic for using electric field to modulate magnetic memory and logic devices [89]. Recently, there has been a significant amount of research on the using an electric field, rather than magnetic field, to write data for ultra-low power writing by utilizing strain to couple the electric and magnetic properties due to electric field scaling down to nanoscale sizes better [90–92]. This can be accomplished modulating the MAE with strain in a

multiferroic heterostructure, where a magnetic layer is coupled to an underlying piezoelectric layer [93,94], and this has been predicted to use only a few aJ of energy [89,95]. Generally, effects of strain on properties of magnetic materials are modeled using either Stoner-Wolfarth modeling or numerical simulations of the LLG equation or first principles calculations [96]. In both cases, strain is nearly always accounted for by simply modifying the effective anisotropy field (H_K) term using an additional magnetoelastic contribution [97], which for a constant strain this assumption is valid. In the situation of a changing strain it is not necessarily valid to simplify effects on electronic structure to an effective H_K because changes in magnetic and lattice deformations are generally coupled. Until recently, there has been little to no simulation work in which changes of magnetic and mechanical properties on each other in thin film materials are simultaneously accounted for, however, Liang et al. also raised this point, and are actively involved with modeling this more accurate coupled magneto-elastic scenario [98]. Lastly, questions remain concerning the ultimate switching speeds on strain modulated MRAM devices; speed on order of ~2.5 GHz has been proposed, but no experimental demonstration has been shown to date [99]. Furthermore, the ultimate device lifetime from the viewpoint of defects introduced by repeatedly deforming the thin film lattice may be a concern, but no work to date has examined this issue.

First principles calculations of the band structure for FePt suggest that the MAE can be reduced by as much as 20 % with a 2 % applied strain [100,101], however, experimental verifications have not realized such large modifications to K_u from

strain, and rely on indirect measurements of magnetization vs field (MH) loops [102], crystallographic ordering [103], and not electronic structure. Thus by using x-ray emission spectroscopy (XES) and x-ray circular magnetic dichroism (XMCD), this work probes effects of strain on the spin states of FePt at a more fundamental level than previously studied and provides more insight than more common magnetic characterization methods. Lastly, it is important to develop a more thorough understanding of the effects on the electronic properties of magnetic materials during the straining process, since these properties are of greater importance for devices which rely on strain for each change of the magnetization direction, rather than a crystal lattice that is always strained as in magnetic recording.

XES, and more specifically resonant inelastic x-ray scattering (RIXS), allows for detailed examination of the occupancy of the 3*d* orbitals, as discussed in chapter 2 [61,104], and has been used to examine effects of bulk strain in FeS [60], properties of nanowires [105], and more; it is now well understood that shifts in the Fe *Kβ* peak correspond to changes in the spin state. Several review works have been published, which provide an in depth examination of the principles and applications for RIXS measurements [58,106,107]. FePt has been examined with x-ray spectroscopy techniques by a few groups, however, the work tends to be purely on the effect of the chemical ordering using x-ray absorption spectroscopy (XAS) [108], which provides insight into the bonding and oxidation states, and less to the electronic structure. XMCD can be calculated by taking the difference in the

XAS spectra at positive and negative saturation field when circularly polarized photon source is used, and can be used to provide insight into the orbital and spin moment contributions.

In this work we examine the effects of varied strain on FePt thin films on the electron structure for the 2*p* and 3*d* states, which provides a deeper understanding of the fundamental effects of a lattice change on the magnetic and transport properties. In this work, we utilize RIXS, XAS, and XMCD to experimentally understand the detailed effects of strain and ordering in FePt. Our results are then supported using first principles calculations to understand the role of strain and ordering. Furthermore, this work provides a baseline for future time resolved studies for switching in strain based memories in order to determine the theoretical switching speeds, and device lifetime from a lattice defect point of view due to repeated crystallographic deformations.

4.2. Fabrication and characterization methods

In order to investigate a static strain on FePt films, and to set a base line for future dynamic experiments, continuous $L1_0$ films were deposited onto $SrTiO_3$ (STO), $KTaO_3$ (KTO) and MgO, with lattice parameters of 3.905, 3.989, and 4.216 Å, respectively. FePt films with nominal thickness of 20 nm were deposited onto MgO, KTO and STO single crystal substrates with (001) texture by a AJA Orion 8 magnetron sputtering system with a base pressure lower than 2×10^{-8} Torr (2.67×10^{-6} Pa) at a temperature of 400 °C, and detailed analysis on similar film structures has been previously reported [109]. The film thicknesses were

confirmed using XRR (18.2, 16.9, 16.9 nm for STO, KTO and MgO respectively) and the true thickness was used for all calculations of the magnetization. The magnetization vs. field (MH) hysteresis loops were measured by a Dynacool Physical Property Measurement System vibrating sample magnetometer (VSM) for in and out of plane magnetizations, and crystallographic information was collected from x-ray diffraction (XRD) using a Panalytical X'pert Pro (Cu-Kα) system. XRD was collected in the conventional geometry as well as the grazing incidence condition.

The 3*d* occupancy of the samples was measured by RIXS at sector 20-ID-C of the Advanced Photon Source (APS). The spin state of Fe was measured observing the *Kβ* x-ray emission, around the main peak ($K\beta_{1,3}$) near 7058 eV and the satellite (*Kβ'*) near 7045.5 eV, from energies 6098 to 7083 eV in 0.5 eV steps, with a total collection time of 22 hours per sample, using an incident flux of 10^{12} photon/s and using the miniXS spectrometer, which has a Rowland-circle geometry, using techniques outlined by Mattern et al [110]. XAS on the Fe $L_{3,2}$ edge was performed using beamline 6.3.1 at the Advanced Light Source and was taken using electron yield mode at room temperature. XMCD was obtained by taking the difference of the XAS spectra at ± 1.7 T on the MgO and KTO samples; the STO XMCD was not calculated since the maximum available field of 1.7 T is not able to saturate this sample (see Fig. 4.2).

4.3. Experimental observation of changes in spin state

The conventional XRD spectra, shown in Fig 4.1a, clearly shows that the FePt films have strong (001) texturing for each of the three substrates indicating each for all samples there is high quality L10 phase. Additionally, near the (001) FePt peak finite thickness oscillations are visible, which further supports the high quality and low surface roughness of the films. The (001) FePt peak for STO lies at 24.09°, KTO at 24.06°, and MgO at 23.98°, which corresponds to 3.691, 3.696 and 3.707 Å, for the *c*-lattice parameter, respectively. The ordering parameter, *S*, comparing the ratio of the integrated intensity for (001) and (002) FePt peaks compared to the theoretical ratio; which was calculated using equation 1.23. The calculated S was normalized by the KTO ordering parameter, since in highly textured films it is common to calculate S > 1.0, due to the derivation of S not adequately accounting for texture. It was found that S = 0.76, 1.00, and 0.96 for MgO, KTO and STO, respectively. Grazing incidence XRD was used to measure the in-plane lattice spacing by scanning the (200) FePt peak, as shown in Fig 4.1b. Due to significant peak overlap with the STO substrate, an additional asymmetric reflection scan at the FePt (201) was taken in addition for the STO sample (figure 1b inset). The in-plane lattice spacing for STO, KTO and MgO FePt was found to be 3.93, 3.90, and 3.89 Å, respectively. Using the experimentally measured values of c and a, a c/a ratio was found to be 0.936, 0.948, and 0.952 for STO, KTO and MgO, respectively. FePt grown on STO is shown to be more compressively strained than the KTO and MgO samples.

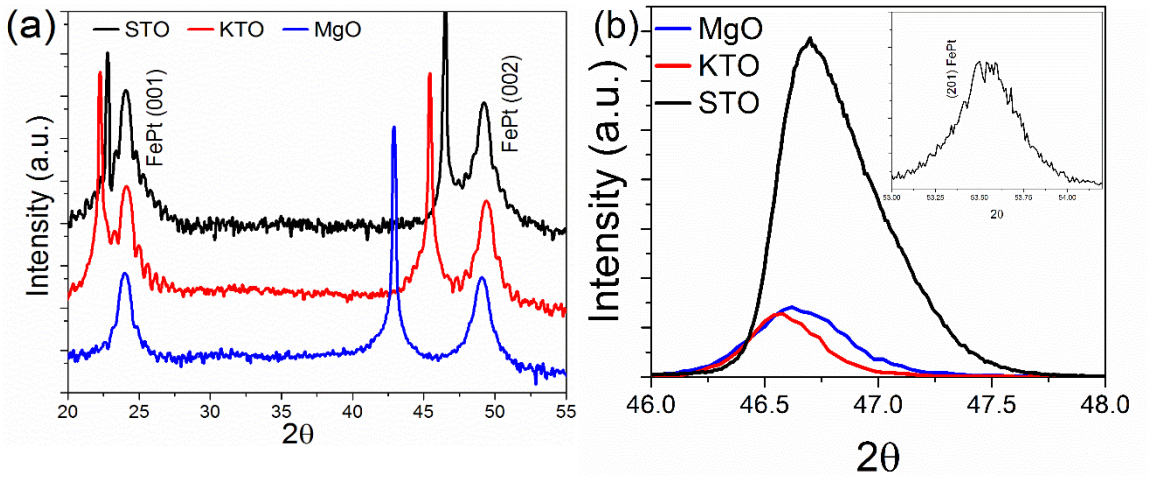

Fig. 4.1: (a) Conventional XRD spectra for 20 nm FePt on STO, KTO and MgO substrates, each showing strong (001) FePt peak near 24.1°; additional peaks are from the substrate. (b) XRD in the grazing incidence configuration for each sample, and the inset shows the off-specular XRD for the (201) FePt peak since the (200) grazing peak strongly overlaps with a substrate peak for the STO sample.

The curves for in- and out-of-plane magnetization vs field (M vs H) are shown in Fig 4.2. The hysteresis loops show a strong out of plane magnetization, as is clear from the 'squareness' of the out of plane loop, however, it should be noted the low coercivity (H_c) of the films is not due to low $L1_0$ ordering, but instead due to domain wall motion since the film is continuous and exchange coupled. There is a clear soft switching 'kink' in the out of plane MH loop for the FePt grown on STO, which is due to a partial A1 phase of FePt in the film, and while the STO film is not ideal, the magnetically hard K_u of the material can still be determined, from the high field switching point of the in-plane MH curve. K_u was calculated from the measured H_k from the in-plane MH loop by extrapolating the switching and saturation region, and using the intercept; as well as accounting for

demagnetization for each of the three samples K_u for STO, KTO and MgO seeded FePt was found to be 4.46, 4.43, and 4.18 x 10^7 erg/cm^3 (x 10^6 J/m^3), respectively. The M vs. H curves also show a variation in the saturation magnetization (M_s), and is 1140 (1.140 x 10^6), 1186 (1.186 x 10^6), and 1220 (1.220 x 10^6) emu/cm^3 (A/m) for STO, KTO and MgO samples, and these experimental values were used in the calculation of K_u.

Variation in K_u with strain, by comparing to the c/a ratio and to variation in ordering shows no conclusive trends. Given that the calculated K_u values are similar in value, and the calculation used the in-plane anisotropy field equation, which relies on M_s, the K_u values are within error since knowing M_s precisely in thin films is difficult in practice due to the error in estimating the magnetic volume. Furthermore, since the samples show an additional difference in ordering, it is impossible to distinguish the effect of strain from chemical ordering without supporting calculations.

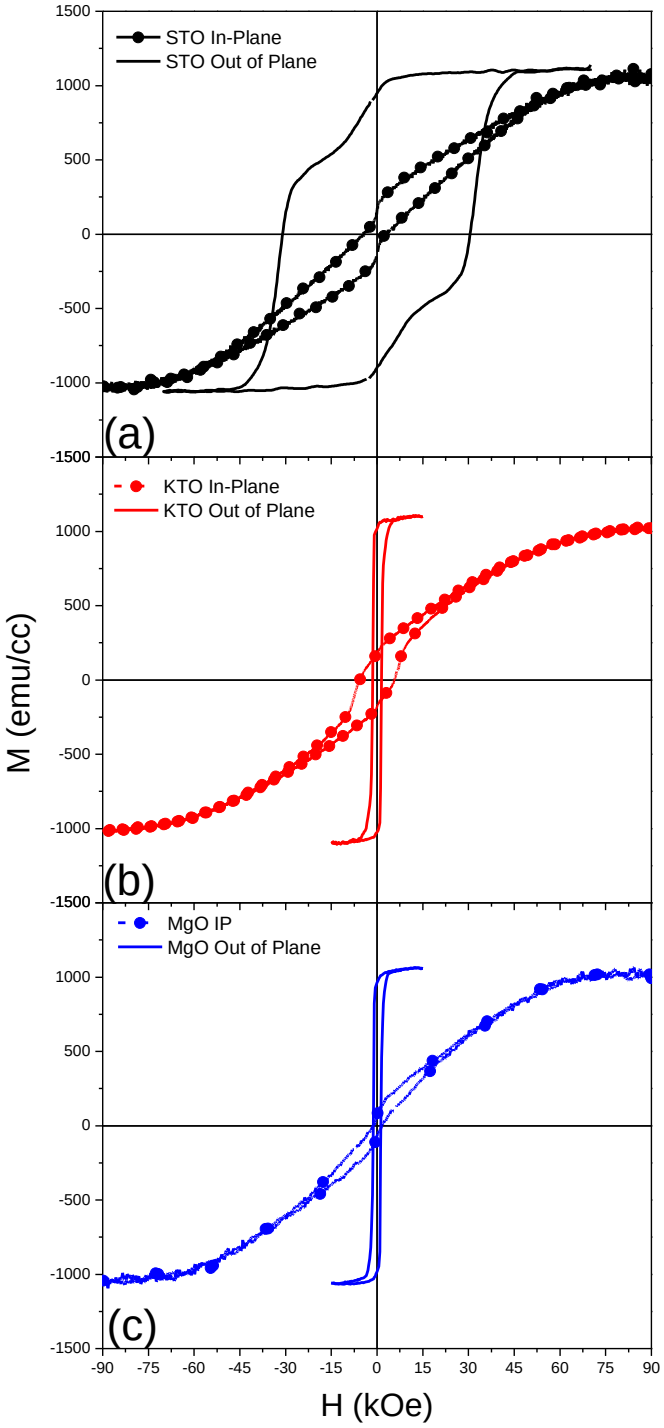

Fig. 4.2: MH out-of-plane (solid line) and in-plane (dashed) measurements for 20 nm FePt on (a) STO, (b) KTO and (c) STO substrates using a VSM at room temperature.

The measured RIXS spectra is shown in Fig. 4.3; the collected data was smoothed using a 5-point adjacent averaging method, and the non-linear background was removed using the Tougaard method [111]. In a RIXS spectra, a shift in the main Fe *Kβ* emission peak to higher energies indicates a lower average spin state compared to peaks at lower energies. The calculated c/a values for the FePt thin films grown on STO, KTO and MgO substrates are 0.936, 0.948 and 0.952, respectively from the XRD measurements. The RIXS spectra shows the main *Kβ* peak shifts to lower energy for increased *c/a* values. This implies that the MgO sample has the highest spin state of the three samples, and STO the lowest. It is also clear that the *Kβ'* satellite peak intensity for MgO is greater compared to the STO and KTO peaks; the latter of which are nearly indistinguishable, which further supports that MgO is at the highest spin state. It should be noted that in general the MgO raw RIXS scans showed higher levels of dispersion, including in MgO based samples not included in this work. Given the normalization and background subtraction schemes used, it is not possible to draw any definite quantitative conclusions concerning the intensity change of the main and satellite peak between the three samples.

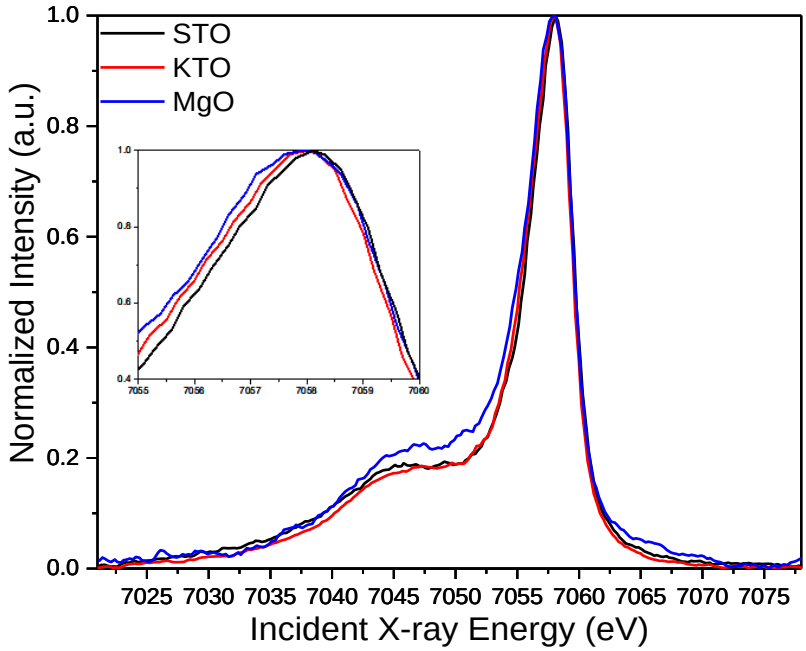

Fig. 4.3: RIXS spectra for Fe fluorescence peak and satellite peak at 7058 and 7045.5 eV, respectively for 20 nm FePt on STO, KTO and MgO substrates. *Kβ* peaks are located at 7058.12, 7057.99, and 7057.91 eV, for STO, KTO, and MgO substrates, respectively. The inset shows a zoom in of the K*β* peak.

XAS measured on the L_3 and L_2 edges for Fe on each sample is shown in Fig 4.4. The XAS shows that the FePt grown on MgO and KTO have similar 3*d* occupations with a majority of 3+ states (lower energy L_3 peak), with a smaller 2+ contribution (higher L_3 shoulder). The FePt grown on STO, however, has a larger 2+ contribution to the 3*d* occupation. XMCD for the samples grown on MgO and KTO are also shown; STO is not shown since the available magnetic field was not able to saturate the sample. It can be seen from the XMCD spectra that the magnetic moment of the Fe is the same for the FePt films grown on the KTO and MgO substrates.

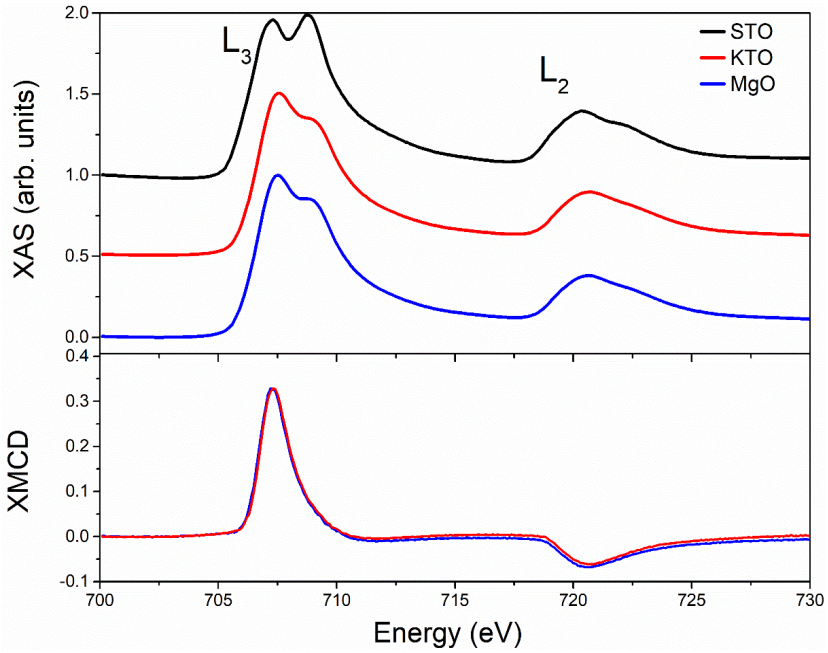

Fig. 4.4: XAS for Fe L_2 and L_3 absorption energies (top) and the XMCD for MgO and KTO samples. The XMCD curve (bottom) is calculated by taking the difference of the XAS spectra at +-1.7 T, which is enough to saturate these samples. The STO XMCD is not shown since 1.7 T cannot saturate the magnetization.

This experiment was proposed and completed to set a baseline for future studies in which time resolved XRD and RIXS measurements on FePt films grown on a ferroelectric when pulsed with an electric field. Unfortunately, it was found during our work that for 20 nm films of FePt a 22-hour RIXS scan per sample is needed to collect adequate signal, and even then, the results we show require significant data processing. Due to this long collection time, which is limited by the photon flux of the APS synchrotron, we have found that given current technologies a time resolved study is not feasible without an improved incident flux.

4.4. Calculations

First principles density functional theory (DFT) calculations have been performed using the Korringa-Kohn-Rostoker (KKR) formulism with the SPRKKR package using Perdew-Burke-Ernzerhof (PBE) exchange-correlation functional within generalized gradient approximation [112]. Configurational disorder was treated within coherent potential approximation (CPA). The DFT calculations were performed for FePt lattices with the lattice parameters reported earlier in the experimental section. The spin and orbital magnetic moment contributions for Fe, Pt and the sum of the two have been calculated and are summarized in Table 4.1.

Sample	lattice parameters(Å)			Fe		Pt		Total	
	a	c	c/a	Spin	Orbital	Spin	Orbital	Spin	Orbital
Bulk	3.86	3.72	0.96	2.90	0.073	0.31	0.051	3.20	0.124
MGO	3.89	3.706	0.952	2.70	0.060	0.29	0.062	2.63	0.110
KTO	3.9	3.696	0.947	2.94	0.073	0.33	0.057	3.27	0.129
STO(opt)	3.93	3.69	0.936	2.94	0.071	0.33	0.060	3.21	0.130

Table 4.1: Summary of moment contribution of Fe and Pt for different FePt lattice constants.

In order to compare to the experimental observation on the Fe 3*d* occupancy from the RIXS experiment, calculations of the Fe d orbital occupancy were calculated for variations in both the c/a value and the ordering of the FePt films, shown in Fig 4.5. Given that the samples also varied in ordering as well as strain, it is necessary to understand the role each effect has on the system, since FePt has been known to have strong variation in K_u due to both factors. The calculations show that both ordering and strain have an effect on the Fe occupancy, and are of similar orders of magnitude. The Fe occupancy has been

calculated to decrease with decreasing c/a, which qualitatively, is the same as observed experimentally.

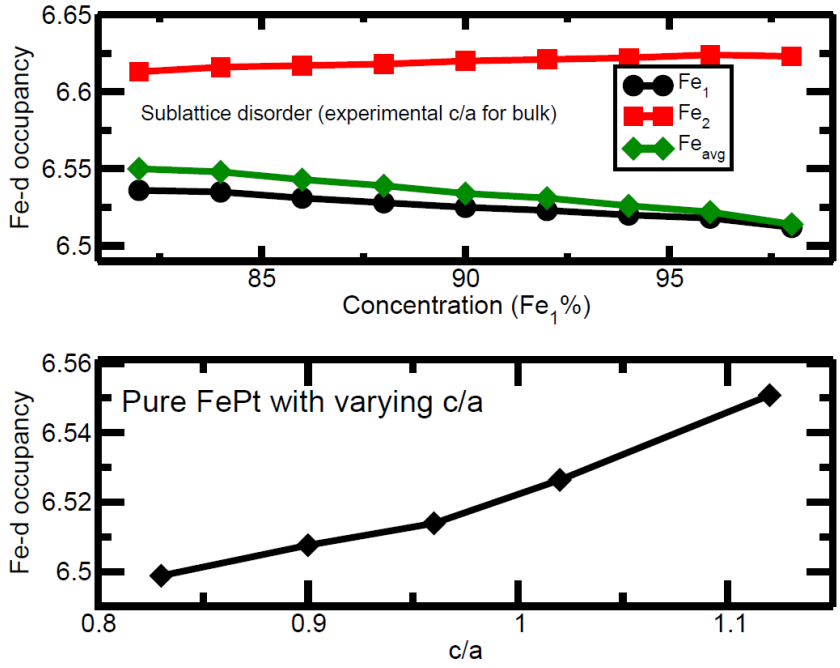

Fig 4.5: 3d orbital occupation for FePt using DFT calculations. The effect of ordering (a) and strain (b) on the Fe 3d occupancy.

4.5. Summary

In summary, we have measured and calculated the occupancy of Fe in FePt thin films with respect to strain. We have shown that a compressive c/a strain in FePt induces a decrease in the Fe 3*d* occupancy. FePt films with increased compressive strain were also found to have a higher K_u; however, due to variation in the ordering between films, it is not possible to draw a definite conclusion concerning strain and K_u from this work. First principles calculations were completed, and replicated the trend of strain on the 3*d* Fe occupancy, and the

effect of chemical ordering was also calculated as a comparison. Lastly, this work provides a static baseline for future time resolved XES and XRD studies to better understand the dynamics of repeatedly strained magnetic based memories, however, given technological limitations in RIXS experimental setups, this may not be feasible until beam lines with higher x-ray fluxes come online.

Chapter 5. Development of MnBi and effect of capping layer for spintronic applications

*Reprinted from P. Quarterman, Delin Zhang, Karl B. Schliep, Thomas J. Peterson, Yang Lv and Jian-Ping Wang, “Effect of capping layer on formation and magnetic properties of MnBi thin films” J. Appl. Phys. **122**, 213904 (2017), with the permission of AIP Publishing.

5.1. Mn based magnetic materials

Mn based materials such as Mn_3Ge, Mn_2Ga, and MnBi have become of interest due to their relatively large perpendicular K_u as large as 1 - 2 x 10^7 erg/cm^3 and modest M_s of approximately 670 emu/cm^3 or less for MnBi [15,32]. MnBi has a stable low temperature phase (LTP), in which a ferromagnetic NiAs hexagonal structure is formed, and has long been studied for permanent magnet applications [33,34], and more recently in spintronic applications due to its high K_u, low M_s, and relatively high spin polarization, and Curie temperature well above room temperature [35,36]. A spin polarization as high as 63% in NiAs structured MnBi has been experimentally demonstrated [37]. First-principles calculations predict a meta-stable zinc blende structure of MnBi which is half-metallic [38], but this metastable phase has not been experimentally reported to date. Furthermore, MnBi is of interest due to having an extraordinarily large Kerr angle [39], and predictions of ultra-fast domain wall motion under a thermal gradient [40]. Also having a MTJ based on hexagonal crystal structures allows for integration with

alternative tunnel barriers [41], and can lattice match to several topological insulators for spin orbit torque switching [42,43]. The previous results discussed use island structured MnBi with film thicknesses on order of 5-200 nm, and it has been shown that forming ferromagnetic MnBi at sub 25 nm thicknesses, while maintaining suitable K_u and M_s, is difficult to achieve [44], which must be overcome for MnBi to integrate into MTJ structures. In addition, MTJ thin films require continuous with low surface roughness, not island-like microstructure. The effect of dopants in MnBi has also been examined, and in the case of adding Fe or Au, the magnetization decreases, K_u and magnetoresistance (MR) ratio can be strongly modified, which has been proposed to be the result of competing ferromagnetic and anti-ferromagnetic interactions [45,46]. In addition MnBi/Al multilayers have been investigated to understand the effect of particle size on the magnetization reversal process [47]. K_u for MnBi also has been shown to have an inverse dependence on temperature [48,49], and is still not well understood.

5.2. Sample growth and characterization methods

LTP MnBi thin films with PMA were prepared by sputtering Bi(20 nm)/Mn(10 nm) bilayers, with a 5 nm capping layer, using a UHV 8-target sputtering system with a base pressure of 1.0×10^{-7} Torr or better at room temperature onto Si/SiO_2 substrates. The capping layer was varied (Ta, SiO_2, Cr and Au) in order to balance chemical stability of the stack structure and feasibility of patterning into nanostructures by minimizing etch rates of the capping layer. Immediately after sputter deposition, the samples were moved into a plasma-enhanced chemical

vapor deposition (PE-CVD) chamber, where an additional 150 nm capping layer of SiO_2 was deposited on top of the films to prevent oxidation of Mn and diffusion of Bi out of the samples during later annealing steps. This results in a completed structure of Substrate/MnBi(20)/X(5)/SiO_2(150), where X is Ta, SiO_2, Au or Cr. It was found without this additional PE-CVD SiO_2 capping layer, ferromagnetic MnBi did not form based on magnetic and crystalline properties, as the films evaporated during the annealing process. Finally, the samples were post annealed at 300 °C for 1 hour under high vacuum. The annealing temperature and time were determined experimentally by maximizing the magnetic moment and the 'squareness' of the magnetization vs field (MH) curve of post annealed films. The magnetic properties were characterized by in-plane and out-of-plane MH loops using a vibrating sample magnetometer (VSM) at room temperature, and crystallographic information was collected by x-ray diffraction (XRD) using a D8 Discover with Co-Kα source. The XRD spectra was recalculated to plot the θ-2θ scan for Cu-Kα angles for analysis more consistent with other reports. In addition, cross-section transmission electron microscope (TEM), in conjunction with energy dispersive spectroscopy (EDS), was used to understand the film structure using a Tecnai G^2 F30 field emission TEM; cross-section samples were prepared using a focused ion beam (FIB) technique [113]. The surface morphology of the films was characterized using bright field optical imaging. It should also be noted that a wide sample to sample variation in magnetic and crystallographic properties was observed, from pieces sputtered on the same wafer, due to variations in the

surface uniformity across the SiO_2 wafer, which leads delamination of the films from the substrate and an incorrect M_s—in order to minimize this error, samples for this work were only taken from the center of the wafer.

5.3. Effect of capping layer on formation of ow temperature phase MnBi

The in-plane and out-of-plane MH loops, for post-annealed MnBi thin films capped with Ta, SiO_2, Cr and Au, are shown in Fig. 5.1. It is clear, from the out-of-plane MH curves that MnBi films capped with Ta and SiO_2 display ferromagnetic behavior with large K_u and sharp switching, while MnBi thin films capped with Au and Cr are not ferromagnetic, and the observed slope of the curves are the dia- and para-magnetic contributions of the substrate and sample holder. In order to calculate M_s, it was assumed that the thin film thickness was twice that of the nominal Mn layer thickness, which assumes for every mono layer of Mn there is a corresponding Bi layer to form the LTP phase. This assumption is supported by the XRD and STEM EDS, which is discussed later in this work. This assumption leads to M_s, for the samples capped with Ta and SiO_2, of 650 and 324 emu/cm^3, respectively. The in-plane hysteresis loops for MnBi thin films capped with Ta and SiO_2 are shown, and using H_K from the in-plane curves, K_u can be estimated to be 6.8 and 3.8 x 10^6 erg/cm^3, respectively, and the demagnetization effect was accounted for ($2\pi M_s^2$). The observed M_s for MnBi films capped with Ta is near the expected value, however K_u is lower than the theoretical prediction [15,32]; this is partially due to a non-fully ordered film, and possibly the reported variations in K_{u1} and K_{u2} ($K_u = K_{u1} + K_{u2}$) and K_{u2} has been shown to be negative at room

temperature and above [48,49]. M_s for MnBi capped with SiO_2, and thus K_u, is even lower than with Ta however; this is due in part to SiO_2 partially oxidizing the Mn layer, which makes the assumption concerning the total thickness of the MnBi layer incorrect, and is also supported by the XRD discussed later in this work. In addition, it is possible that in the samples capped with SiO_2 the MnBi have been oxidized, as it has been reported that oxidized MnBi shows a decrease in M_s, and an increase in coercivity [114].

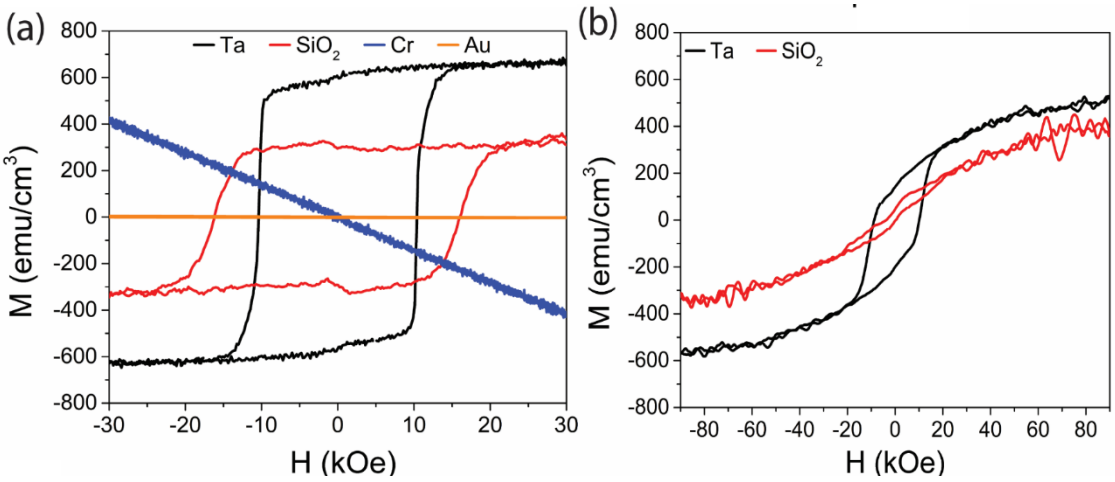

Fig. 5.1: (a) Out-of-plane and (b) in-plane M vs. H loops for MnBi thin films. Out of plane shows that the MnBi films capped with Ta and SiO_2 are clearly ferromagnetic and primarily perpendicular, whereas MnBi films capped with Au and Cr are not ferromagnetic. In-plane MH curves for the samples capped with Ta and SiO_2 show that there is an in-plane component to the easy axis, likely due to misalignment between MnBi grains.

The θ-2θ XRD spectra are shown in Fig. 5.2 for the as-deposited Bi/Mn bi-layer and the post annealed MnBi films with each relevant capping layer sample. The as-deposited XRD spectra are similar for all samples, clearly showing the (003), (012) and (006) Bi peaks, and a weak (012) MnBi peak is found, which may

be due to inter-diffusion at the Bi/Mn interface during deposition. After post annealing, the characteristic (002) and (004) MnBi peaks appear only in samples capped with Ta and SiO_2, which fits with the observed hysteresis loops in Fig. 5.1. The properly formed MnBi films show additional MnBi crystallographic orientations, which indicates the films are not fully textured in the out-of-plane orientation, which is also to be expected based on the MH curves. MnBi capped with Ta shows no strong Bi diffraction peaks, which suggests the Mn and Bi have fully diffused to

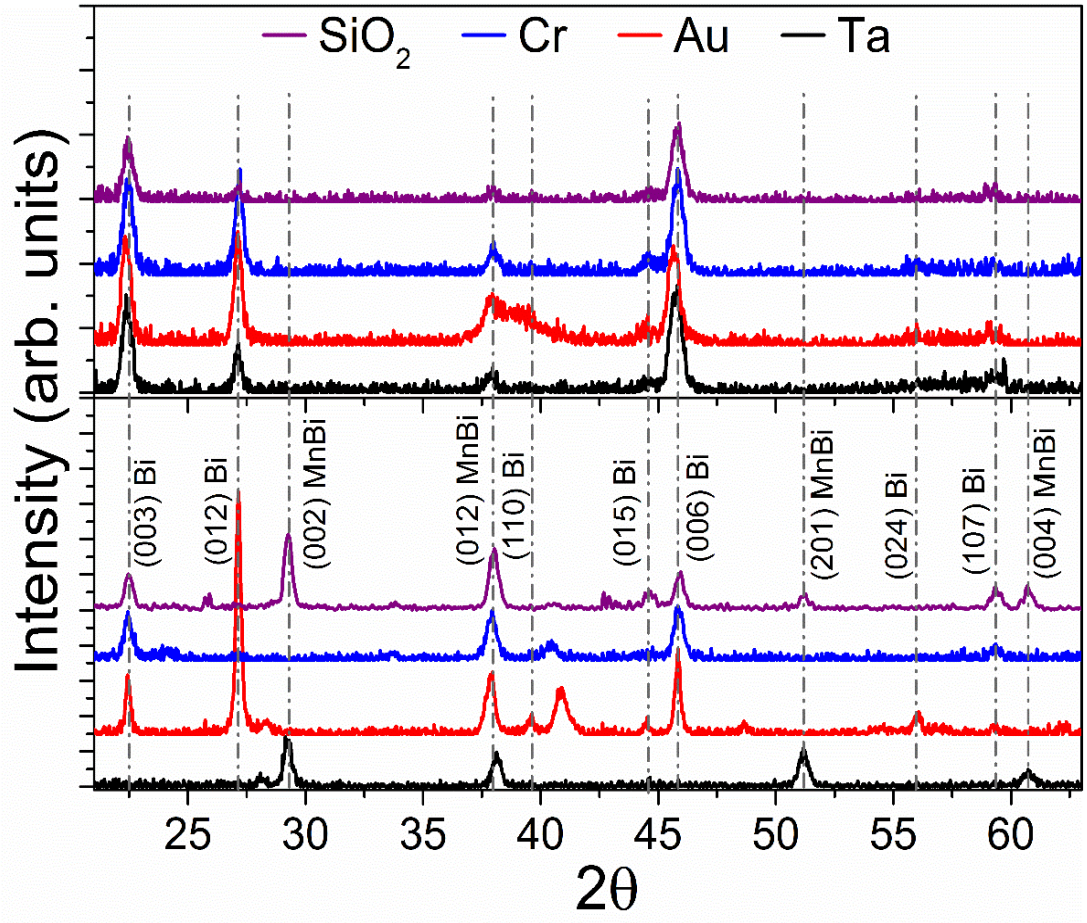

Fig. 5.2: XRD for MnBi thin films with varied capping layer as deposited (top) and after post annealing (bottom). The emergence of the characteristic (002) MnBi peak after post annealing can be seen.

form LTP MnBi. However, when capped with SiO_2, many Bi peaks appear after annealing, which indicates there is significant amount of Bi remaining under the MnBi, and this crystallized during the post annealing.

Cross-sectional STEM was used to further understand the structure of MnBi films capped with Ta after the annealing process. Fig. 5.3 shows MnBi capped with Ta, after post annealing, and the samples are continuous, with a MnBi thickness on average of 20 nm, but with large surface roughness; they are not uniformly

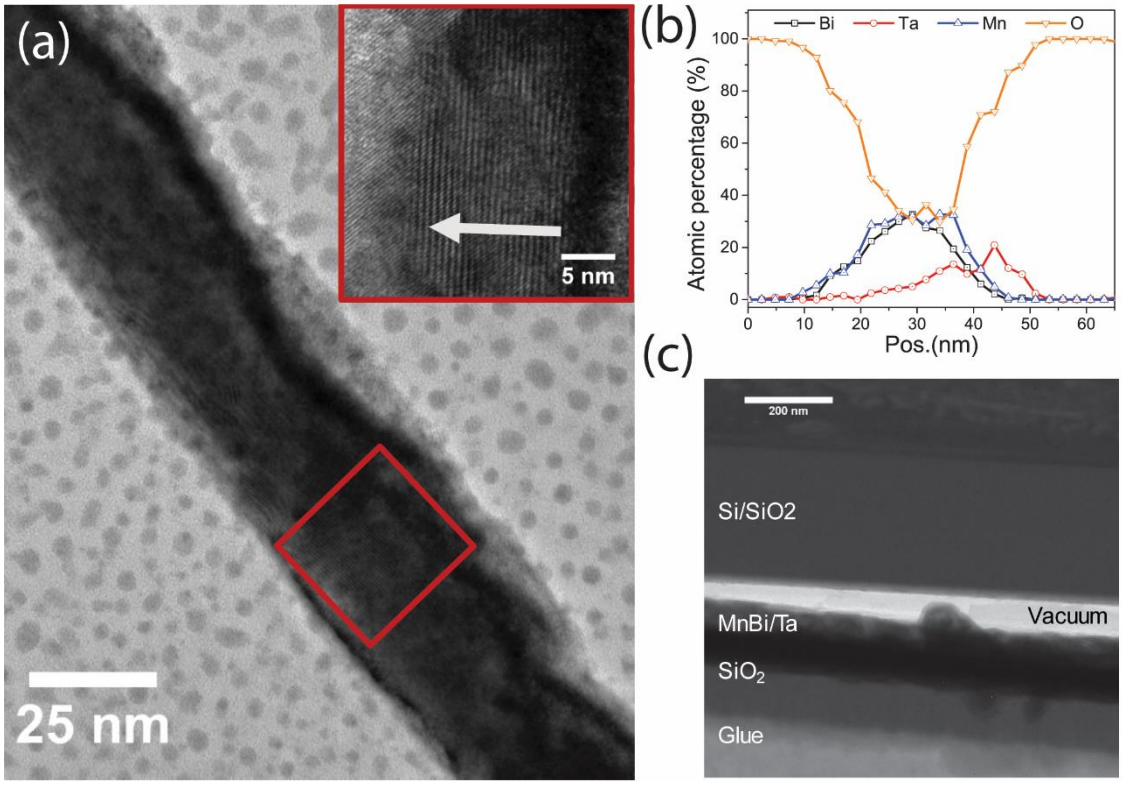

Fig. 5.3: (a) Cross-section TEM of MnBi capped with Ta after post annealing along the LTP phase [01-11] zone axis shows highly textured grains, but are not uniformly aligned in the out-of-plane orientation, as noted by the white arrow in the inset (red box). In addition, a large surface roughness is observed. (b) STEM EDS shows the MnBi film is fully diffused, and a large amount of oxygen is in the film, which occurred during the process of transferring the cross-section lamella from the FIB to TEM. (c) STEM shows regions of the MnBi film have peeled off the substrate.

textured along the (001) axis. STEM EDS across the sample cross section shows the Mn and Bi have fully formed the desired MnBi, and no obvious remaining Mn and Bi layers remain, and the Mn to Bi ratio is approximately 1:1, which supports our assumption on the thickness of the magnetic MnBi region. Regions in which the MnBi film has delaminated from the substrate can be seen in the STEM images, which partially accounts for sample to sample variation of magnetic and crystalline properties observed.

There are two possible explanations that can account for the capping layer effect observed that fit with the observed XRD—diffusion of the capping layer into the Mn/Bi layers (in the case of Au and Cr), or oxidation of the Mn layer. Cr and Au are known to commonly diffuse into neighboring thin films due to their high diffusivity, but given MnBi doped with Au has been reported on, and remains ferromagnetic with large K_u [45]. The other possible cause is Au and Cr are poor diffusion barriers from preventing the O_2 in the SiO_2 from oxidizing the Mn layer during the process of transferring from the sputtering to PE-CVD chamber, and during the PE-CVD process, due to a surface energy mismatch. This additional SiO_2 layer is necessary for the post-annealing process, since without it no (002) MnBi peak was found using XRD, and in addition samples without the additional 150 nm SiO_2 displayed no ferromagnetism. Fig. 5.4 shows the surface morphology of the samples after post annealing, and the samples capped with Ta and SiO_2 show a mostly continuous film surface. The films capped with Cr shows mazelike structure with large grain boundaries, and the Au capping layer has large regions

in which the Au appears to have peeled off, which indicates poor adhesion of Au and Cr due to a surface energy mismatch. The lack of a well adhered continuous film coating MnBi, which is clearly visible even at optical resolutions for Au and Cr, allows for oxidation of the Mn layer prior to annealing for MnBi formation. This explanation is also supported by evidence that when the capping layer is 5 nm of sputtered SiO_2 before the PE-CVD deposition, the noted M_s is lower than when

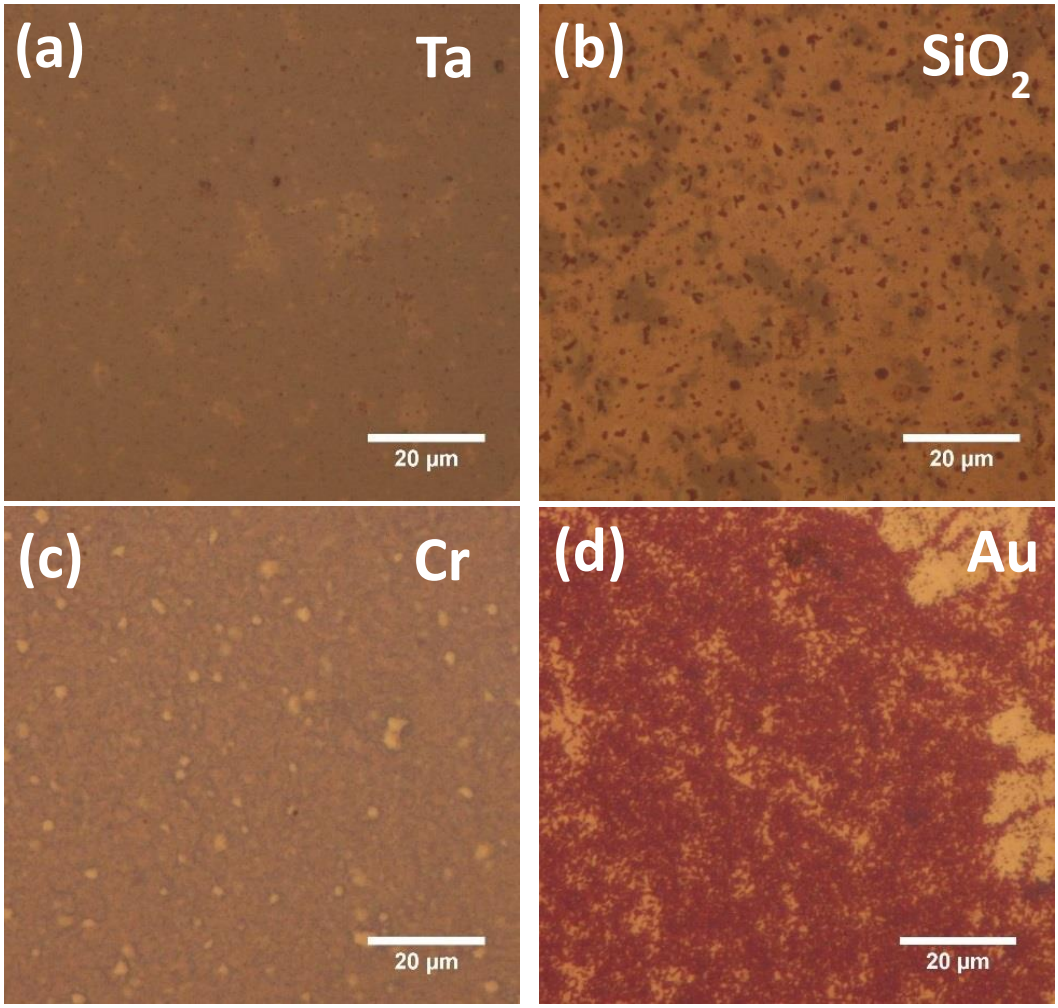

Fig. 5.4: Surface morphology of MnBi caped with (a) Ta, (b) SiO_2, (c) Cr, and (d) Au. Surface morphology of MnBi capped with Ta and SiO_2 show continuous like surfaces, show large grain boundaries, and in the case of gold even flaking off.

capped with Ta—if some of the sputtered SiO_2 oxides the Mn layer, then this would account for the slightly lower magnetization measured; which is further supported by the observed remaining crystalized Bi XRD peaks in the MnBi/SiO_2 film. In the case of Au and Cr capping layers, they allow for the Mn layer to fully oxidize, which in turn prevents the formation of MnBi. It is also feasible that Au and Cr diffuse into the underlying layer, which also prevents the formation of LTP MnBi. Given that even samples coated with SiO_2 show a decreased M_s, it is clear that oxidation of the Mn layer prior to post-annealing is detrimental to the LTP MnBi formation process.

5.4. Summary

In summary, we have shown that the formation of ferromagnetic LTP MnBi, utilizing sputtering deposition combined with vacuum post annealing, is dependent on the capping layer. It has been proposed that the cause for this effect is dependent on the capping surface energy matching with MnBi, and their ability to prevent Mn oxidation. We have demonstrated fully formed 20 nm LTP MnBi continuous thin films which, when capped with Ta, display an out-of-plane easy axis, with M_s of approximately 650 emu/cm^3 and K_u of 6.8 x 10^6 erg/cm^3. The films have large surface roughness, and suffer from sample consistency due to film delamination; this must be improved for MnBi to become a feasible material in MTJs, which can be solved by improving the adhesion to the substrate.

Chapter 6. Demonstration of the 4th ferromagnetic element at room temperature: Ru

*This chapter has been reproduced from the manuscript "*Demonstration of the 4th ferromagnetic element at room temperature: Ru*" by P. Quarterman, Congli Sun, Javier Garcia-Barriocanal, Mahendra DC, Yang Lv, Paul M. Voyles, and Jian-Ping Wang" which is under review with Nature Communications.

6.1. Introduction

Large MCA in magnetic materials is due to the involvement of 4*d* and 5*d* valence shells, which makes magnetism in metals with these valence shells of great interest. Bulk Ru is paramagnetic, stable in HCP crystal structure, and has a long history of use in as a seed layer in hard disk media [115], a spacer in synthetic anti-ferromagnetic structures that are used for both magnetic read heads and STT-RAM [116], and also can be used as a capping layer due to its chemical stability. Theoretical calculations have proposed ferromagnetism is possible in Ru, Os and Ur if these elements can be forced into a tetragonal lattice structure [117–119]. Shiki *et al.* claimed to have formed body centered tetragonal (BCT) Ru by growing on single crystal (110) Mo substrates, but in their study they did not report the magnetic properties of their thin films [120]. More recently it has been proposed that tetragonal Ru may have large perpendicular MCA with up to two orders of magnitude greater than traditional 3d magnetic metals due to Jahn-Teller splitting [121]. Due to its inherit metastability, BCT Ru cannot be grown in bulk.

However, by utilizing strain in thin films it is possible to realize a metastable phase given properly lattice matched seed layers to induce nucleation of this metastable BCT phase in ultra-thin Ru films. A BCT structure with lattice constant a = 3.25 Å and distorted such that c/a = 0.84, has been predicted to have large MCA; the dependence of the lattice parameters on the magnetic properties of tetragonal Ru is shown in Fig 6.1 [121]. In this work, we synthesized ultra-thin BCT Ru films and experimentally demonstrated Ru as the fourth room temperature ferromagnet on the periodic table.

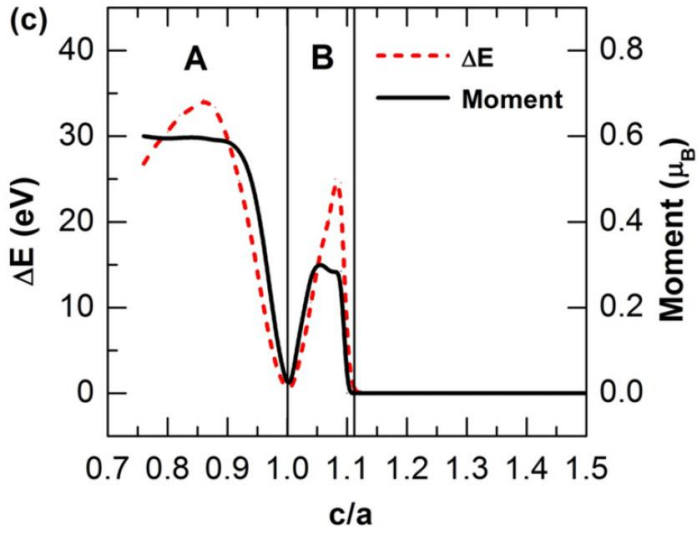

Fig 6.1: Predicted energy difference between magnetic and nonmagnetic Ru (ΔE) magnetic moment for tetragonal Ru as a function of lattice parameters as calculated by Odkhuu et al [121]. Reprinted with permission from Odkuu et all, Phys. Rev. B. 91, 014437 (2015). Copyright 2015 by the American Physical Society.

6.2. Sample fabrication and epitaxial relationships

Epitaxial Ru films with nominal thickness of 2.5, 6, and 12 nm were grown on ($11\bar{2}0$) Al_2O_3 substrates with a 20 nm (110) Mo seed layer at 400 ^oC. These

samples were grown using an 8-target UHV sputtering system at base pressure of 8 x 10^{-8} Torr or better and with an *in-situ* heater at 400°C; the samples were post annealed in the chamber for 1 hour immediately after deposition. A non-textured stack with a 20 nm Mo seed layer and 2.5 nm of Ru was grown at room temperature as a control sample, and a 20 nm (110) Mo layer, with no Ru, sample was grown at 400 ^{o}C on a (11 $\overline{2}$ 0) Al_2O_3 substrate as an additional control.

Magnetization vs field (M-H) loops were measured using a VSM at 10 K and 300 K, respectively. The crystallographic information was collected using conventional and grazing incidence XRD, and x-ray XRR with a Panalytic X'pert Pro (Cu-Kα) system. Cross section STEM samples were prepared by in-situ lift out using a Zeiss Auriga focused ion beam (FIB), the samples were coated with Au in order to protect the Ru surface during preparation. The final FIB milling voltage is dropped to 2 kV to minimize damage from implanted Ga. STEM imaging is performed on an FEI Titan with CEOS probe aberration corrector operated at 200 kV with a probe convergence angle of 24.5 mrad, spatial resolution of 0.08 nm, probe current of ~20 pA and by stabilizing the sample for 6+ hours inside the TEM column, with 20 µs pixel dwell time. Transport measurements to examine the anomalous Hall effect were conducted using a Quantum Design Physical Property Measurement System with magnetic field applied perpendicular to as-deposited 5 mm x 5 mm samples with the Vander-Pauw configuration. In addition to testing a BCT Ru textured sample, a non-textured with same stack structure was measured

under the same conditions. Atomic force microscopy (AFM) was acquired using a Bruker Nanoscope V Multimode 8.

6.3. Crystal structure characterization

(110) Mo lattice matches and grows well on (11$\bar{2}$0) Al_2O_3 oriented substrates at an offset angle of approximately 35° [122,123]. The crystallographic families of planes (11$\bar{2}$0) and (0001) of the Al_2O_3 substrate can be represented as (110) and (001), respectively, and will be denoted as such throughout the remainder of this paper. A cartoon of the expected epitaxial relationship for the film stack of (110) Al_2O_3 // (110) Mo // (01$\bar{1}$) Ru is shown in Fig. 6.2a. This epitaxial relationship has been confirmed using x-ray diffraction (XRD) in the grazing incidence configuration, and by rotating the sample 360°. As shown in Fig. 6.2b, the expected 4-fold symmetry for the (110) planes of Al_2O_3 has been observed, and the predicted Mo crystallographic orientation is rotated approximately 35° from the (001) substrate plane. The coupled θ-2θ XRD scans, for all four samples, are shown in Fig 6.2c. The sample grown at room temperature does not show any evidence of texturing in the thin films, but the samples with Ru layer with nominal thickness of 2.5, 6, and 12 nm grown at 400 °C, show highly textured (110) Mo. The scans show finite size diffraction fringes corresponding to the total thickness of the sample, and the low roughness of the interfaces. A peak, which corresponds to both the (01$\bar{1}$) BCT phase Ru at 43.25° or (101) HCP phase Ru at 44.02°, increases in intensity and shifts from 43.31° to 43.96° from the 2.5 nm to the 12

nm sample. Since with increasing Ru thickness, the peak shifts to larger 2θ, narrows in width, and the finite thickness fringes disappear, XRD scans suggest a mixing of BCT and HCP phases is present, and the HCP to BCT ratio increases with Ru thickness. This two-phase nature of the films is further supported by cross

section electron microscopy—discussed later in this paper. In addition, the desired BCT Ru structure, with *a* = 3.25 Å, is strained to a smaller interatomic spacing than is predicted. This is because the (001) Mo plane (3.15 Å) is straining the (100) BCT

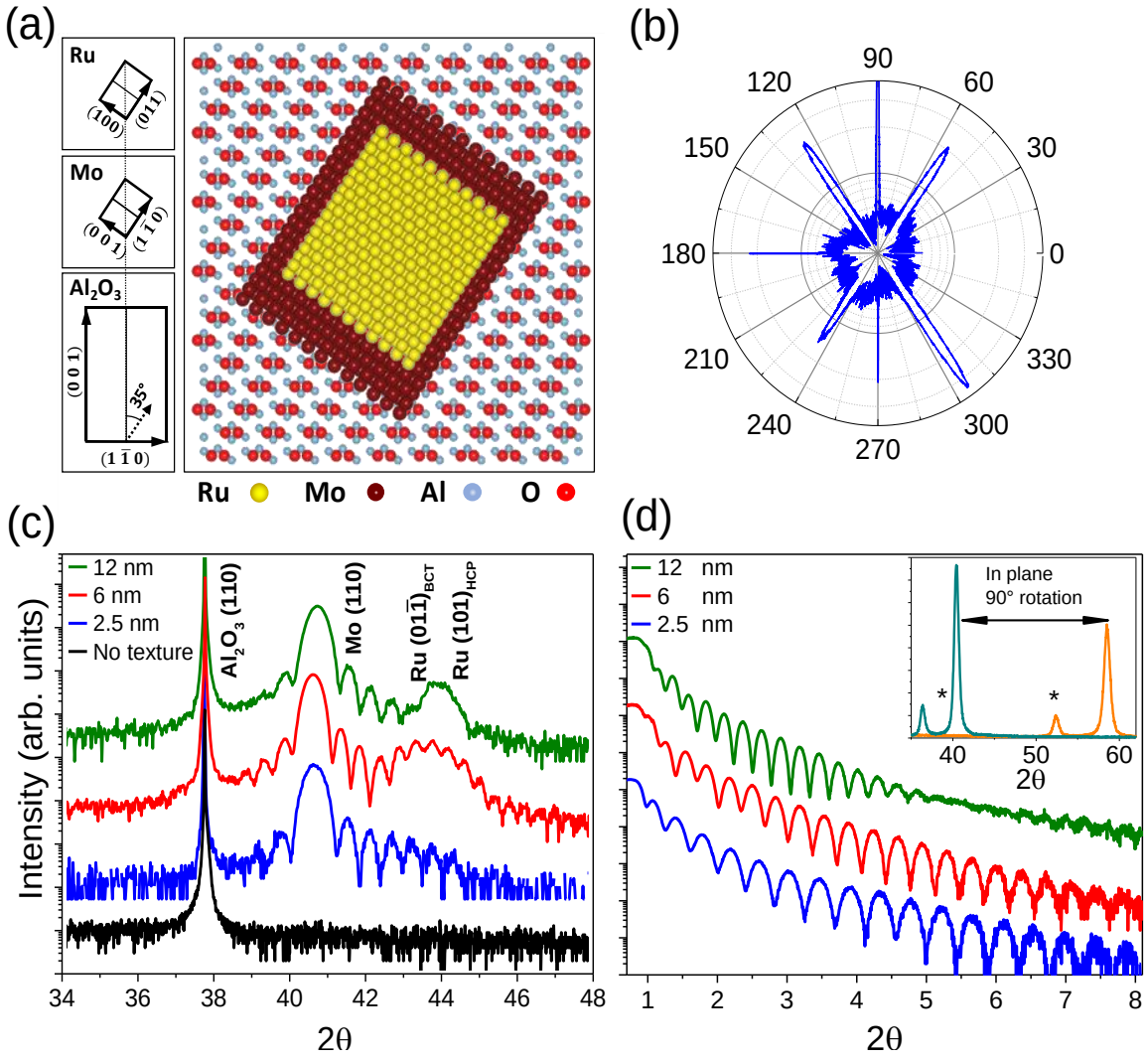

Fig. 6.2: The expected crystallographic structure and epitaxial relation is shown using (a) a cartoon showing the epitaxial growth relation for (110) Al_2O_3 // (110) Mo // 01$\bar{1}$Ru, and (b) x-ray diffraction using grazing incidence, by placing the detector in the (110) plane of Al_2O_3 and rotating the sample over 360°. (c) Conventional XRD spectra with the orientation parallel to {110} Al_2O_3, and (d) x-ray reflectivity for 2.5, 6, and 12 nm Ru films; with the inset of (D) showing the grazing incidence coupled scan when aligned to the short (black) and long (blue) edge of (110) Mo.

Ru plane. Such a strain on the BCT Ru lattice would shrink *a* to less than 3.25 Å, which creates a distortion of the BCT Ru phase, and will increase 2θ for the $(01\bar{1})$ BCT Ru plane. X-ray reflectivity (XRR) for the textured samples is shown in Fig. 1d, and the oscillations to 10° show the low roughness of the interfaces of the samples. The reflectivity curve was fit using GenX [55], which confirmed the film thicknesses for the Mo and Ru thin films, and a low interface roughness of less than 3 Å. The in-plane lattice parameters for the Mo layer were measured using the grazing incidence XRD configuration, as shown in the inset of Fig. 6.2d, and Mo lattice constants matching the theoretical values were observed. The roughness of the Ru surface was found to be 0.21, 0.13, and 0.21 nm for 2.5, 6,

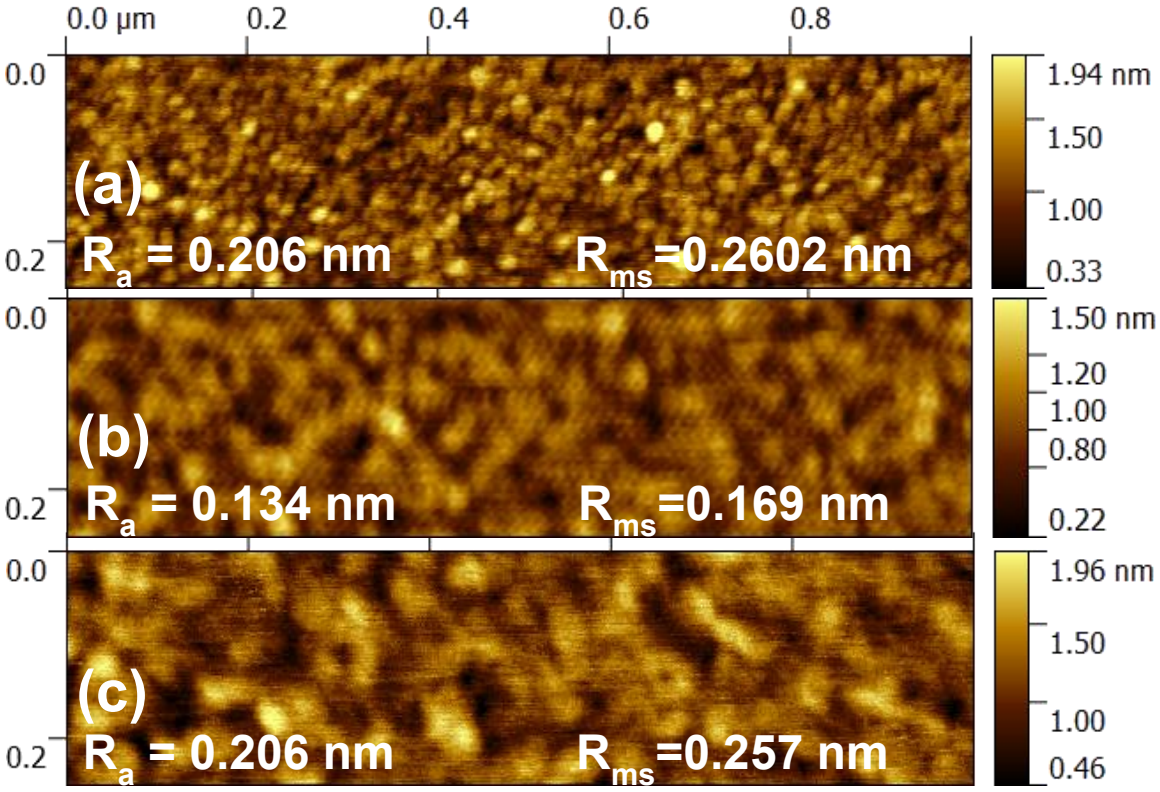

Fig 6.3: AFM images for (a) 2.5, (b) 6 and (c) 12 nm Ru films show a smooth Ru surface.

and 12 nm Ru films, respectively, as measured by atomic force microscopy (AFM), shown in Fig. 6.2, which closely matches the results of the XRR fits.

Cross-section STEM images along the [001] Al_2O_3 zone axis, which matches the [111] Ru zone axis, of the 6 nm Ru sample, were obtained, and are shown in Fig. 4. The high angle annular dark field (HAADF) STEM image (Fig. 4b) shows that the Ru and Mo layers are highly textured, and the tetragonal structure of the Ru layer has been confirmed using high precision HAADF STEM [124]. There are also clear distortions in the Ru epitaxy, which can be viewed as a shift of every other $(1\bar{1}0)$ plane, as shown in the high-precision HAADF STEM image. This distortion is believed to be caused by the mismatch between (001) Mo and (100) Ru, as pointed out in the XRD discussion earlier. The grain boundary shown in Fig. 6.3c is formed by different orientations of the lattice distortion, and two equivalent $\{10\bar{1}\}$ surfaces of tetragonal Ru on the [111] zone axis. Fast Fourier transform (FFT) of the STEM (red boxed region of Fig. 6.5b) has been used to determine that the structure of the Ru film is distorted BCT (Fig. 6.5). A cartoon to visualize the expected FFT pattern along the [111] zone axis for tetragonal Ru is shown in Fig. 6.5b. The lattice parameters, *c* and *a*, were estimated using fitting; it was completed with the assumption that the crystal is a perfect tetragonal structure, and using the measured interatomic distances (d_1, d_2, d_3) and atomic plane angles (θ_1, θ_2, θ_3). Using this method, d_1/d_2 has been calculated and leads to a *c/a* ratio

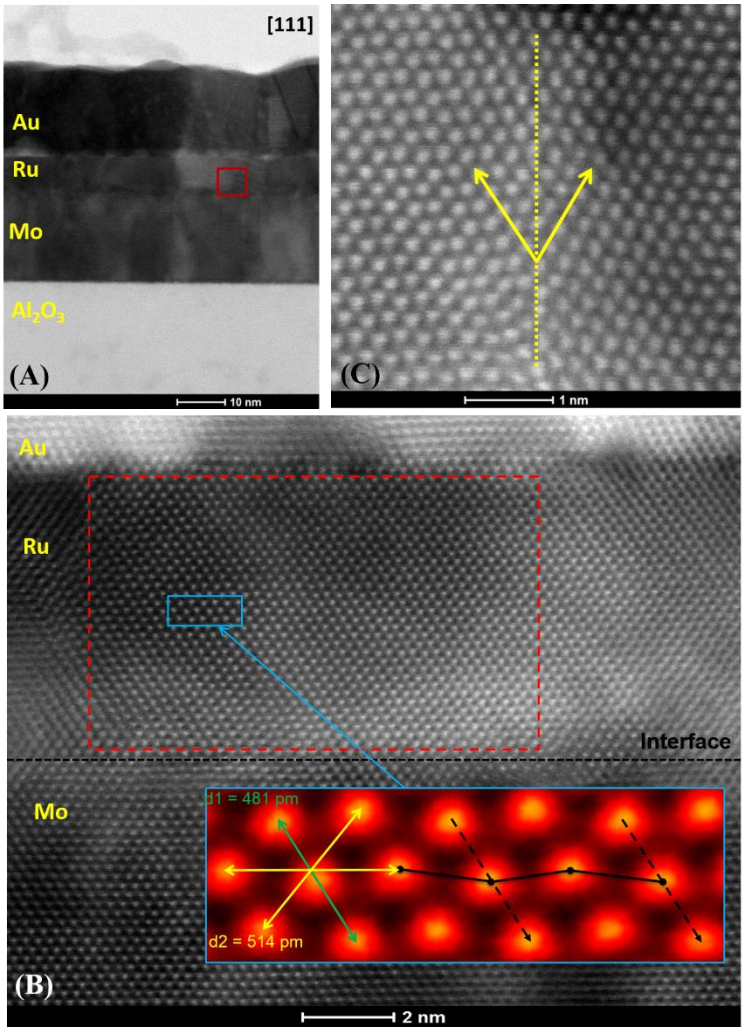

Fig. 6.4: Cross section STEM images along the [001] zone axis of Al_2O_3. (a) The annular bright field (ABF) STEM images of the full sample stack. (b) High angle annular dark field (HAADF) STEM at the Mo-Ru interface, with the inset showing the high-precision HADDF STEM for the [111] Ru zone axis using the non-rigid registration method [124]. The lattice distortion is shown using the dashed black line. (c) A HAADF STEM zoom in on a Ru grain boundary due to equivalent surfaces growth surfaces.

of 0.88, which corresponds to a = 3.19 ± 0.3 Å, and is near the optimal prediction for BCT Ru of 3.25 Å; furthermore, it is not surprising to see minor deviations given that the Ru film has distortions in the tetragonal structure, which cannot be accounted for in this model.

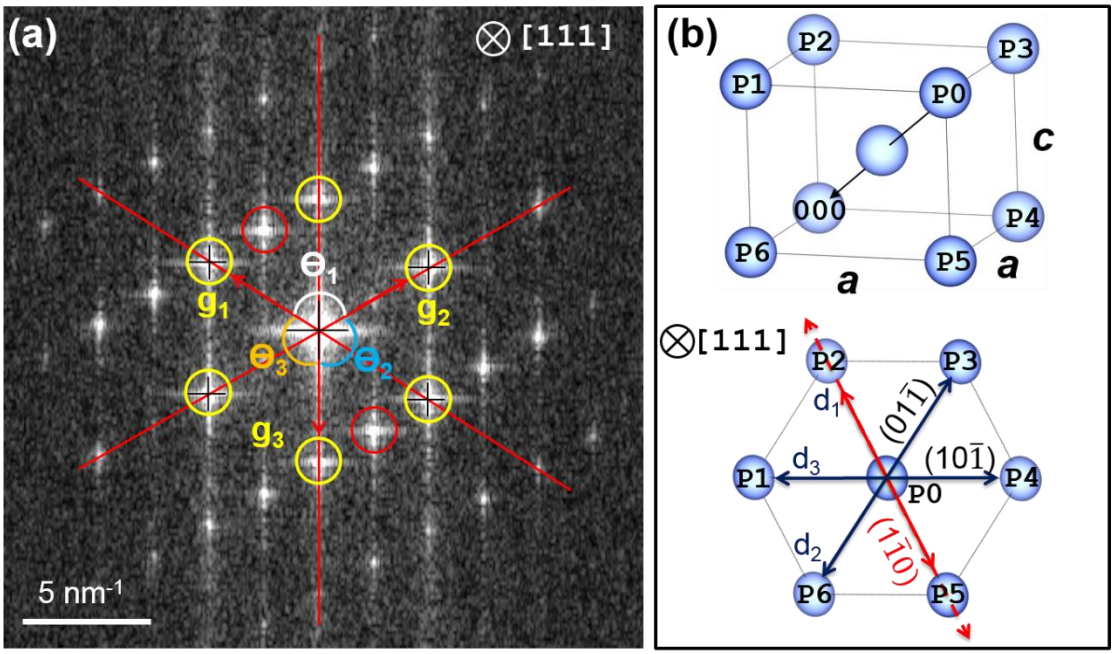

Fig. 6.5: (a) FFT of the 6 nm Ru film along the [111] zone axis, from indicated region of Fig. 4b, with the expected BCT grouping highlighted in yellow, and distortions in the tetragonal ordering are highlighted in red. (b) The expected [111] zone axis projection for BCT Ru, and by using the measured interatomic spacing and atomic plane angles, an estimate of c/a for a BCT structure can be calculated. The dashed red line shows the orientation of the lattice distortion.

Cross section STEM images were also collected on 2.5 and 12 nm Ru samples (Fig 6.6). These STEM images show that at 2.5 nm, the Ru thin film is predominately in the BCT phase. In the 12 nm Ru sample, while there are clear regions of BCT Ru spanning the entire film thickness, there are also regions that cannot be definitively identified by HR-STEM because of two competing Ru phases: BCT and HCP—which supports to XRD data which shows a shift from the BCT to HCP phase with increased thickness. The reason that the two-phase

regions cannot be identified by STEM images were collected at a zone axis correlating to the BCT Ru structure, and specific HCP Ru crystallographic information cannot be determined from these images. It should also be noted that two-phase regions, as shown in 12 nm Ru films of Fig 6.6, exist in 2.5 and 6 nm films, but it is clear that two-phase Ru regions increase in frequency as the Ru film thickness increases.

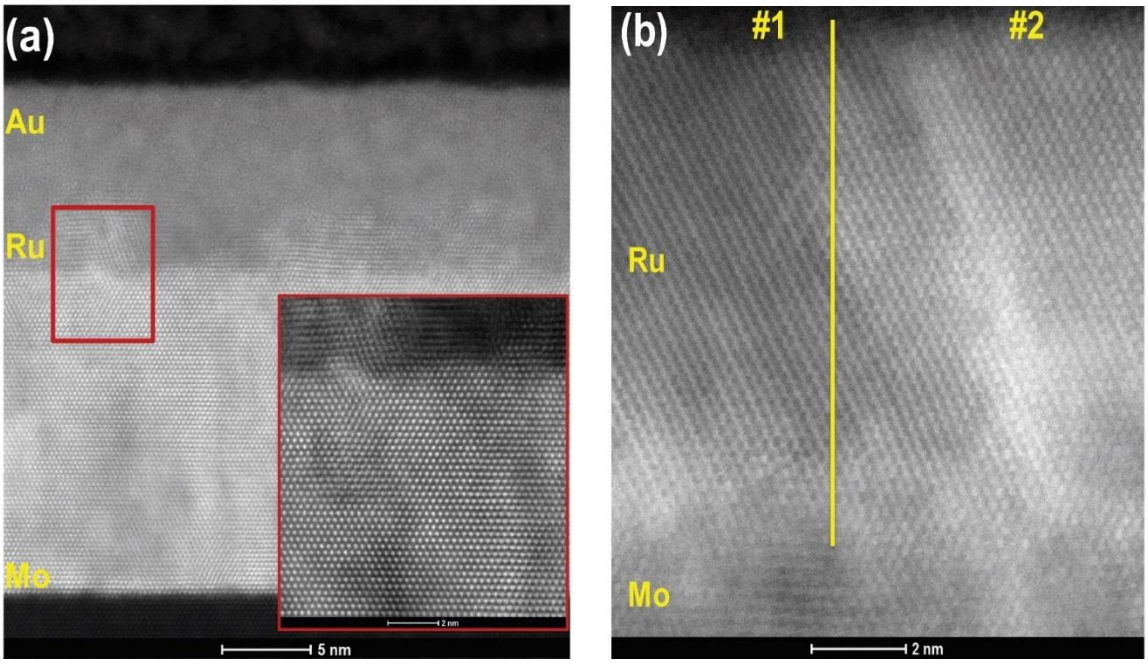

Fig 6.6: Cross-section STEM of (a) 2.5 nm Ru samples, where the inset shows the interface. And (b) 10 nm Ru samples. Even at 10 nm it is clear from region #2 BCT Ru grains pan the entire thickness, which supports our strain supporting BCT nucleation rather than a purely strain induced phase. In region #1, phase analysis cannot be completed due to overlapping phases.

6.4. Ferromagnetism in tetragonal phase Ru

The in-plane magnetization vs field (M-H) hysteresis loops for 2.5, 6 and 12 nm Ru films, grown at high temperature, were measured at 10 and 300 K (Fig. 6.7)

by a VSM. The M-H loops display clear ferromagnetic behavior with a maximum M_s of 160 and 148 emu/cm^3 at 10 and 300 K, respectively, in the 2.5 nm thick Ru film. M_s was calculated by assuming the entire Ru layer is magnetic, and M_s was found to decrease with increasing Ru thickness. Multiple samples, and multiple M-H curves were measured, for all samples, and are shown in Table 6.1. Given that 2.5 and 6 nm Ru samples show a similar room temperature M_s, a mean M_s value of 141 emu/cm^3 was calculated by averaging M_s from all samples with these thicknesses, which further rules out potential magnetic contamination. All samples show a coercivity (H_c) of ~130 Oe. In order to be further certain that the observed ferromagnetism is not due to sample contamination, the same sample holder used for the Ru measurement was measured alone (after each sample), at 10 K and 300 K, and only a paramagnetic signal was measured (Fig. 6.8a is such an example). Furthermore, the measurements were repeated several times with

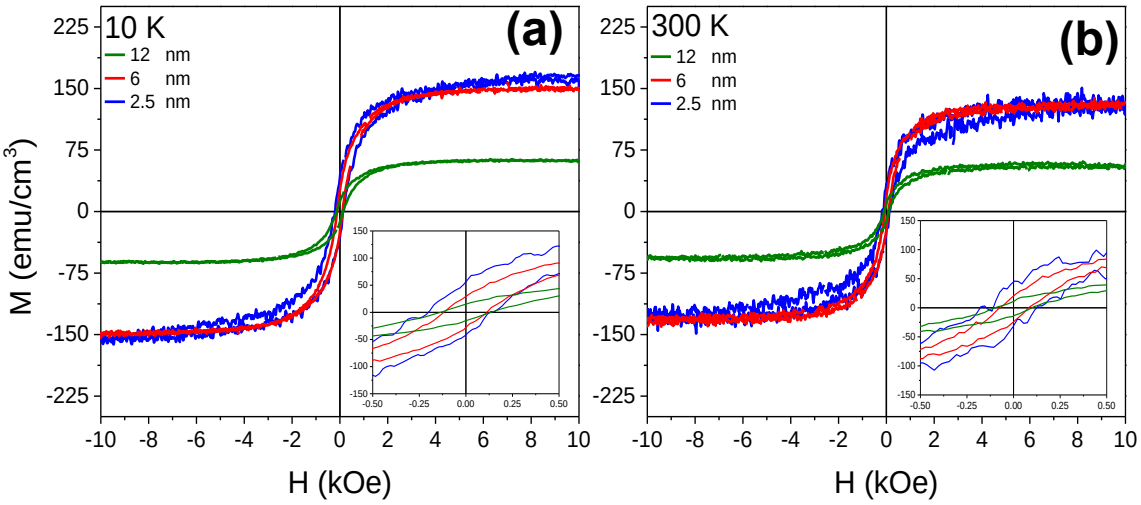

Fig. 6.7: Magnetization vs field hysteresis curves with an in-plane field orientation for 2.5, 6, and 12 nm of Ru at (a) 10 K and (b) room temperature, with the inset for each showing a zoom in near the coercive field region.

multiple holders to ensure results are not an artifact. To further support BCT textured Ru, not magnetic contamination, is responsible for the ferromagnetic M-H loop measurements on the room temperature deposited samples with no crystallographic texture were collected, and none display ferromagnetism (Fig. 6.8b is an example, which is repeatable). A textured (110) Mo sample grown on (110) Al_2O_3 at 400 °C was also measured (no Ru layer on top) as an additional control, and also showed no ferromagnetic behavior (Fig. 6.8b); this rules out ferromagnetism from the Mo layer, and any possible magnetic contamination introduced from *in situ* heating of the samples during deposition. This has been further supported by Rutherford backscattering measurements where no discernable signal corresponding to Fe, Co or Ni was found. A total of five 2.5 nm, five 6 nm, and 12 nm Ru samples were grown. In addition, five control samples were grown that should contain no ferromagnetism and are used to rule out

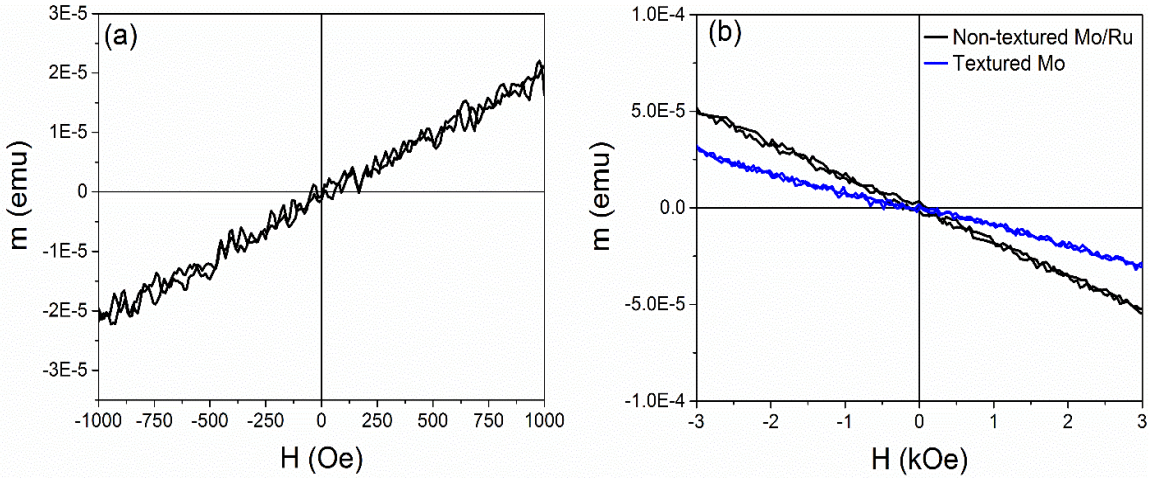

Fig 6.8: Moment vs field for (a) VSM sample rod, r (b) non-textured Ru (black) and textured (110) Mo with no Ru (blue) control samples. Both curves show no ferromagnetism, and correspond to the 2.5 nm sample. The 6 and 12 nm sample holder show similar non-ferromagnetic behavior.

contamination as the source of observed ferromagnetism (e.g. no texturing in thin films, or no Ru layer). Table 6.1 summarizes all samples grown, and a combined total of 11 out of 12 samples for 2.5, 6 and 12 nm samples show ferromagnetic behavior similar to results shown in Fig 6.7. In total, 0 out of 5 control samples (those with no texture, and (110) textured Mo with no Ru layer) displayed ferromagnetism. The sample that does not clearly show ferromagnetism was sputtered on a 2-inch Al_2O_3 wafer, whereas all other samples in this work were grown on 5 x 5 mm^2 Al_2O_3 squares. Each sample was measured multiple times at both room temperature and 10 K, the total number of ferromagnetic M vs. H hysteresis loops for each sample is also noted in Table 6.1.

Sample Sub\Mo(20)\Ru(X)	**2.5 nm**	**6 nm**	**10 nm**	**Control**	**Total FM samples**
# Made	5	5	2	5	12
# FM	4	5	2	0	11
# FM M vs. H	30	21	4	5	55

Table 6.1: The total number of samples fabricated (top row) are displayed in the '# Made' row and the number of these samples that display ferromagnetic (FM) behavior, such as in Fig. 6.7, are counted in the #FM row. Finally, the total number of ferromagnetic hysteresis loops measured across multiple measurements of the combined samples of the same thickness is counted in the '#FM M vs. H' row.

Room-temperature transport measurements were collected on the 6 nm textured BCT Ru sample, with the same (110) Al_2O_3 substrate and 20 nm (110) Mo seed layer, by measuring the Hall resistance as a function of external field

using the Vander Pauw method. A dc current for Hall measurements of 0.1 mA was used. The Hall resistance increases linearly as external out-of-plane field is increased, and it saturates when all in-plane moments are pulled out-of-plane near ±4 kOe as shown in Fig. 6.8. In ferromagnets, the Hall resistance is given by $R_{Hall} = R_o + R_{AHE}$, where R_o is the ordinary Hall resistance and proportional to the external field; R_{AHE} is the anomalous Hall resistance and is proportional to the perpendicular component of magnetization [125]. At lower external field R_{AHE} is

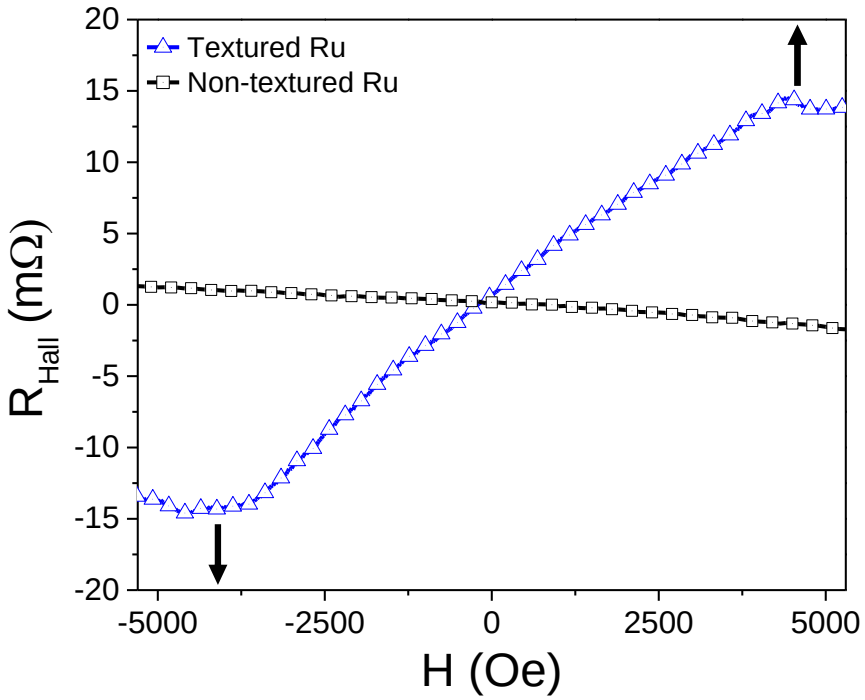

Fig 6.9: Hall resistance vs. field (applied perpendicular to surface) for textured triangles) and non-textured (squares) Mo/Ru films. The substrate/Mo/Ru sample, which has no crystallographic texture, shows only the ordinary Hall effect, but the Ru sample with BCT texture shows the anomalous Hall effect in addition to the ordinary Hall effect. Given that the Ru samples do not have a perpendicular easy axis, the resistance will change once the field is strong enough to saturate the demagnetization field of $4\pi M_s$, corresponding to a M_s of approximately 318 emu/cm^3. The saturated regions are designated by black arrows.

dominant whereas at larger field R_o dominates. The saturation external field is equivalent to the demagnetization field ($4\pi M_s$ for a thin film), which corresponds to the M_s = 318 emu/cm^3. Another control sample with a stack structure of substrate/Mo(20)/Ru(6), which has been shown to have no texture in the Mo or Ru layers (Fig. 1c), was measured and only shows a linear field dependent resistance due to the ordinary Hall effect. This supports our claim that the observed magnetism is due to Ru BCT texturing, and not from any magnetic contamination. Furthermore, the transport measurement rules out the possibility of the magnetism observed coming from dust, since dust cannot contribute to the conduction. It should be noted that the 2.5 nm Ru Hall resistance vs field curve is not shown given that the 20 nm Mo layer is so much thicker than the Ru that current shunting makes the noise level too large.

Odkhuu *et al.* predicted a M_s of approximately 400 emu/cm^3, and a perpendicular K_u of ~10^7 erg/cm^3, if the optimal tetragonal lattice is realized with the (001) tetragonal Ru orientation being out-of-plane [121]. The measured M_s of 160 emu/cm^3, at 10 K by VSM, is lower than the predicted 400 emu/cm^3, and decreased further with increased Ru thickness. M_s was calculated assuming the entire volume of the Ru layer is uniformly ferromagnetic, which has been shown to not be an accurate assumption, and is the major source of error in precisely calculating M_s. For example, it is clear from XRD spectra and STEM images that some Ru grains in the samples do not have BCT structure, and so this is a magnetic ‘dead’ region that dilutes the calculated magnetization. The frequency of

these non-BCT Ru grains increases with film thickness, and is the reason for the dependence of M_S on Ru thickness. The AHE measurement (Fig. 6.8) shows a M_S closer to the prediction, of approximately 318 emu/cm^3, which is not surprising since this technique does not rely on precisely knowing the volume of ferromagnetic Ru. Additionally, the lower than expected Ms, from both VSM and AHE measurements, can be due to both the c/a ratio not being exactly 0.84, as predicted, and the observed lattice distortions. Furthermore, it is not yet clear how the distortion of the tetragonal lattice affects the magnetic properties. The in- and out-of-plane (the latter not shown) measurements do not show a magnetic easy axis, which is as expected since the (001) BCT Ru axis does not align perpendicular to the substrate. The low coercivity and remanence observed can be explained by the multiple available equivalent growth orientations, the continuous thin films being in the free domain wall limit, and mis-matched tetragonal grains for the in-plane orientation.

6.5. Summary

In summary, we have developed a room temperature ferromagnetic metastable tetragonal phase of Ru by using a Mo seed layer to strain the Ru thin film. Our *c/a* ratio of 0.88 was found to be within error of the predicted ratio of 0.84. Using textured and non-textured seed layers, we have confirmed the observed ferromagnetism is not due to contamination in the sample. A magnetization of 148 emu/cm^3 was found at room temperature, and using multiple samples and M-H measurements, a mean value for the magnetization of 141 emu/cm^3 was

calculated. The metastable tetragonal structure of the Ru layer has been confirmed, and distortions were observed, which may dilute the magnetization and MCA. The (001) tetragonal Ru plane does not lie perpendicular to the substrates which leads to a soft coercive field, however, if out-of-plane texturing can be achieved high K_u Ru may be realized. The thickness dependence was also examined, and it has been found that due to Ru relaxing into a non-ferromagnetic phase, the magnetization drops with increasing thickness. Transport measurements of the anomalous Hall resistance supported the observation of ferromagnetism from BCT textured Ru. This work experimentally demonstrates that it is possible to create single element ferromagnetic materials at room temperature outside of Fe, Co and Ni. Finally, achieving high K_u BCT Ru with the (001) axis lying perpendicular to the substrate plane may be possible using a MgF_2 // Ta // Ru epitaxial relation.

Chapter 7. Concluding remarks

7.1. Summary

In chapter 1, an overview of ferromagnetism, and key effects for data storage and memory technologies have been presented. This chapter also summarized the key opportunities and challenges in magnetic based data technologies. Magnetic hard disk media has dominated for the past few decades but is now facing rising competition solid state memory technologies. On the memory front, magnetic based memories are on the rise by competing against traditional semiconductor technologies. Both aspects of magnetic data storage technologies have surmountable, but difficult challenges in order to continue to prove their viability in the marketplace.

Chapter 2 focused on summarizing experimental methods of thin film growth and the associated characterization techniques. Several techniques were derived in explicit detail, but more advanced techniques were presented with brevity since several thorough theoretical works have been published which delve into the complexity of the characterization methods.

In chapter 3, the long debated 'kink' in even highly ordered $L1_0$ FePt thin films and nanoparticles was addressed. In this work we showed the partially soft anisotropy field observed in FePt thin films and nanoparticles is not due to ordering or dipolar effects, but instead due to an invalid assumption concerning MCA. In magnetic materials where the number of surface atoms are on order of the 'bulk

state' atoms, it is no longer fair to assume the bulk MCA value due to a broken symmetry. In the case of FePt, which relies on 3*d* Fe electrons polarizing 5*d* Pt electrons for high anisotropy, at surfaces their decreased Fe-Pt interaction causes a decrease in MCA. We showed that by coating FePt nanoislands with an epitaxial Pt layer this symmetry issue can be avoided.

In chapter 4 the detailed effects of strain on the 3*d* Fe occupancy were studied by using FePt grown with different epitaxial mismatch. This study was designed to examine the fundamental magnetism of strained FePt which the basic magnetostriction model may have overlooked. It was found that in FePt, strain can have a minor change on the 3*d* occupancy of Fe on the same order which chemical ordering can. While this study was insightful in a case of constant strain, the long-term goals of this study to examine *in situ* time dependent strain effects is impossible due access to synchrotrons with higher brightness.

In chapter 5, MnBi was explored as an alternative high anisotropy material to FePt given that it has smaller critical current densities which is necessary for switching in STT technologies. In this work, we have shown that due to the volatility of Mn and diffusion of Bi, MnBi magnetic thin films are dramatically sensitive to even the capping layer used. Suitable and unsuitable capping layers were shown, and demonstration that MnBi thin films can have high K_u and predicted M_s even at 20 nm thicknesses was shown.

Finally, in chapter 6, we experimentally verified theoretical predictions that Ru is ferromagnetic at room temperature when in the metastable tetragonal phase.

The tetragonal phase was demonstrated using XRD and STEM, which independently verified each other's results. Multiple samples, including appropriate magnetic control samples, with repeated hysteresis loops were measured, in addition to anomalous Hall effect measurements to ensure the observations were not due to contamination. The predicted high Ku of tetragonal Ru was not observed, but this is due to the non-perpendicular epitaxial growth used to achieve tetragonal Ru.

7.2. Future of magnetic materials

The future of magnetism in data storage technologies and fundamental research is quite bright overall. HAMR hard disk drives are near ready for consumer usage, and technologies such as MAMR and BPM are in development to continue growth of areal densities. These technologies will rely extensively on the ability to grow or pattern sub 5 nm high K_u materials.

Magnetics in the spintronics field is especially promising and is on the forefront of research for both commercial and fundamental research. Recent advances in magnetic materials seem to hint that STT is ready to take place in the marketplace. Memory applications of magnetic memories are likely to start from applications such as automotive, internet of things, and eventually storage and computational methods.

Recently, it has been suggested that utilizing a spin orbit torque (SOT) scheme has been proposed as an alternative write scheme to STT, and predicts critical switching current densities as low as 10^4-10^6 A/cm^2 [126]. In the SOT write

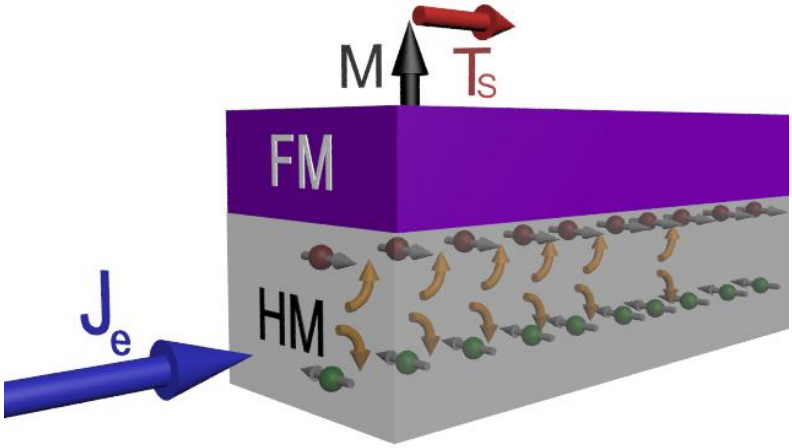

Fig 7.1: Schematic of spin Hall based switching of a ferromagnetic using purely a charge current.

scheme (shown in Fig. 1), the ferromagnetic (FM) free layer of the MTJ is in contact with a non-ferromagnetic heavy metal (HM) with large spin orbit coupling. When an in-plane charge current (J_e) is injected into the HM, a spin current (J_S) is generated in the vertical direction due to spin orbit coupling, and the accumulated spin current at the HM/FM interface exerts a spin torque, which can assist switching of the magnetization direction of the FM layer. SOT structures can also be used to realize a three-terminal configuration, by separating the read and write current channels, which limits aging of the device, and accidental writes due to the read current [127]. In the SOT scheme, generation of J_S transverse to J_e arises from the spin Hall effect, where $J_S = \theta_{SH}(\boldsymbol{\sigma} \times \boldsymbol{J_e})$, and θ_{SH} corresponds to the spin Hall angle, which is the magnitude of the ratio J_S/J_e is material dependent. This spin current accumulation exerts a spin torque, which can assist in flipping the magnetization direction of the adjacent FM, as diagrammed in Fig 7.1. Traditional HM, also known as spin Hall channel, materials come from the 5d transition metals,

such as Pt [128] and high resistivity β-Ta [129] with θ_{SH} ≈ 0.07 and -0.15, respectively, due to their inherit large spin orbit coupling associated with 5d orbitals. An increase in θ_{SH} means each electron from J_e injected into the HM induces a larger spin accumulation at the HM/FM interface, thus a larger spin torque, leading to a smaller write current needed for switching. An in-plane J_e serves as the write current, which is longitudinal to the HM, and so does not stess the MTJ tunnel barrier, while the read current is transverse to the MTJ, which cannot cause accidental writes.

This new write scheme has opened the door to countless studies of materials suitable for SOT switching in both traditional magnetic materials, and non-traditional such as topological insulators. These structures require heavy metals due to their large spin-orbit effect, but the field is still in the early stages. The work presented for ferromagnetic Ru may prove to be of great interest since the electron shells for magnetism are in the 4*d* orbitals, rather than 3*d* for traditional magnetic materials, which may give rise to useful spin-orbit effects.

The current 'holy grail' of spintronics is full realization of using electric field to manipulate the magnetization orientation. This allows for low write energies and non-volatility. Magnetic technologies are even making their way into healthcare by using GMR and magnetic nanoparticles to detect cancers [130]. Since the realization of spin triplet Josephson junctions, the traditional view of magnetism and superconductivity being incompatible has been overturned. This opens

another avenue for magnetics in data storage methods and does not require the advanced high K_u materials discussed in this dissertation dictate.

References

[1] R. O'Handley, *Modern Magnetic Materials: Principles and Applications* (2000).

[2] H. E. Nigh, S. Legvold, and F. H. Spedding, Phys. Rev. **132**, 1092 (1963).

[3] M. M. Sigalas and D. A. Papaconstantopoulos, Phys. Rev. B. **50**, 7255 (1994).

[4] B. D. Cullity and C. D. Graham, in 2nd ed. (Wiley, 2009), pp. 258–266.

[5] R. C. O'Handley, *Modern Magnetic Materials* (John Wiley & Sons, 2000).

[6] A. Moser, K. Takano, D. T. Margulies, M. Albrecht, Y. Sonobe, Y. Ikeda, S. Sun, and E. E. Fullerton, J. Phys. D Appl. Phys. **35**, R157 (2002).

[7] D. Weller, X. Wang, E. Champion, G. Parker, T. Klemmer, A. Ajan, G. Ju, and B. Stipe, Available: Http://www.idema.org (2012).

[8] J. P. Wang, M. Jamali, A. Klemm Smith, and Z. Zhao, in *Nanomagnetic Spintron. Devices Energy-Efficient Mem. Comput.* (John Wiley & Sons, 2016), p. 352.

[9] K. L. Wang, J. G. Alzate, and P. Khalili Amiri, J. Phys. D. Appl. Phys. **46**, 74003 (2013).

[10] A. V. Khvalkovskiy, D. Apalkov, S. Watts, R. Chepulskii, R. S. Beach, A. Ong, X. Tang, A. Driskill-Smith, W. H. Butler, P. B. Visscher, D. Lottis, E. Chen, V. Nikitin, and M. Krounbi, J. Phys. D Appl. Phys. **46**, 139601 (2013).

[11] H. Meng and J. P. Wang, Appl. Phys. Lett. **88**, 172506 (2006).

[12] S. Ikeda, K. Miura, H. Yamamoto, K. Mizunuma, H. D. Gan, M. Endo, S.

Kanai, J. Hayakawa, F. Matsukura, and H. Ohno, Nat. Mater. **9**, 721 (2010).

[13] K. Ikegami et al, IEDM Tech. Dig S28 (2014).

[14] T. Kawakhara, K. Ito, R. Takemura, and H. Ohno, Microelectron. Reliab. **52**, 613 (2012).

[15] A. Sugihara, K. Suzuki, T. Miyazaki, and S. Mizukami, Metals (Basel). **2**, 910 (2015).

[16] J. P. Wang, Proc. IEEE, Invit. Pap. Spec. Issue Adv. Magn. Storage Technol. **96**, 1847 (2008).

[17] E. Yang, D. E. Laughlin, and J. G. Zhu, IEEE Trans. Magn. **48**, 7 (2012).

[18] O. A. Ivanov, L. V. Solina, V. A. Demshina, and L. M. Magat, Fiz. Met. Met. **35**, 92 (1973).

[19] B. M. H. Kryder, E. C. Gage, T. W. Mcdaniel, W. A. Challener, R. E. Rottmayer, G. Ju, Y. Hsia, and M. F. Erden, Proc. IEEE **96**, (2008).

[20] S. Ikeda, K. Miura, H. Yamamoto, K. Mizunuma, H. D. Gan, M. Endo, S. Kanai, J. Hayakawa, F. Matsukura, and H. Ohno, Nat. Mater. **9**, 721 (2010).

[21] D. Weller, a. Moser, L. Folks, M. E. Best, M. F. Toney, M. Schwickert, J.-U. Thiele, and M. F. Doerner, IEEE Trans. Magn. **36**, 10 (2000).

[22] D. Weller and A. Moser, IEEE Trans. Magn. **35**, 4423 (1999).

[23] K. R. Coffey, M. a. Parker, and J. K. Howard, IEEE Trans. Magn. **31**, 2737 (1995).

[24] S. Sun, C. B. Murray, D. Weller, L. Folks, and A. Moser, Science (80-.). **287**, 1989 (2000).

[25] H. Zeng, J. Li, Z. L. Wang, and S. Sun, Nature **420**, 395 (2002).

[26] T. Moriyama, S. Mitani, T. Siki, T. Shima, and K. Takanashi, J. Appl. Phys. **95**, 6789 (2004).

[27] G. H. O. Daalderop, P. J. Kelly, and M. F. H. Schuurmans, Phys. Rev. B. **44**, 12054 (1991).

[28] Z. Li, J. Cao, F. Wei, K. Piao, S. She, and D. Wei, J. Appl. Phys. **102**, 113918 (2007).

[29] Z. Lu, R. V. Chepulskii, and W. H. Butler, Phys. Rev. B. **81**, 94437 (2010).

[30] Y. Xu, J. S. Chen, and J. P. Wang, Appl. Phys. Lett. **80**, 3325 (2002).

[31] W. K. Shen, J. H. Judy, and J.-P. Wang, J. Appl. Phys. **97**, 10H301 (2005).

[32] D. Chen, J. F. Ready, and E. G. Bernal, J. Appl. Phys. **39**, (1968).

[33] N. V. R. Rao, A. M. Gabay, and G. C. Hadjipanayis, J. Phys. D Appl. Phys. **46**, 62001 (2013).

[34] J. B. Yang, W. B. Yelon, W. J. James, Q. Cai, M. Kornecki, S. Roy, N. Ali, and L. Ph, J. Phys. Cond. Matt. **14**, 6509 (2002).

[35] R. R. Heikes, Phys. Rev. B. **99**, 446 (1955).

[36] J. B. Yang, K. Kamaraju, W. B. Yelon, W. J. James, Q. Cai, and A. Bollero, Appl. Phys. Lett. **79**, 1846 (2001).

[37] P. Kharel, P. Thapa, P. Lukashev, R. F. Sabirianov, E. Y. Tsymbal, D. J. Sellmyer, and B. Nadgorny, Phys. Rev. B. **83**, 24415 (2011).

[38] Y.-Q. Xu, B.-G. Liu, and D. G. Pettifor, Phys. Rev. **66**, 184435 (2002).

[39] R. F. Sabiryanov and S. S. Jaswal, Phys. Rev. B. **53**, 313 (1996).

[40] A. Sukhov, L. Chotorlishvili, A. Ernst, X. Zubizarreta, S. Ostanin, I. Mertig, E. K. U. Gross, and J. Berakdar, Sci. Rep. **6**, 24411 (2016).

[41] O. V. Yazyev and A. Pasquarello, Phys Rev. B. **80**, 35408 (2009).

[42] L. Liu, O. J. Lee, T. J. Gudmundsen, D. C. Ralph, and R. A. Buhrman, Phys. Rev. Lett. **109**, 96602 (2012).

[43] M. Jamali, J. S. Lee, J. S. Jeong, F. Mahfouzi, Y. Lv, Z. Zhao, B. K. Nikolic, K. A. Mkhoyan, N. Samarth, and J. P. Wang, Nano Lett. **15**, 7126 (2015).

[44] T. Hozumi, P. Leclair, G. Mankey, C. Mewes, K. Hono, and T. Suzuki, J. Appl. Phys. **115**, 17A737 (2014).

[45] P. Kharel, R. Skomski, D. J. Sellmyer, P. Kharel, R. Skomski, and D. J. Sellmyer, J. Appl. Phys. **109**, 07B709 (2011).

[46] P. Kharel, X. Z. Li, V. R. Shah, N. Al-Aqtash, K. Tarawneh, R. F. Sabirianov, R. Skomski, and D. J. Sellmyer, J. Appl. Phys. **111**, 07E326 (2012).

[47] U. Rüdiger, G. Güntherodt, P. Fumagalli, L. Thomas, S. S. P. Parkin, and A. D. Kent, J. Appl. Phys. **88**, 4221 (2000).

[48] T. Suwa, Y. Tanaka, G. Mankey, R. Schad, and T. Suzuki, AIP Adv. **6**, 56008 (2016).

[49] I. Masashi, Y. Tanaka, T. Satoh, G. Mankey, R. Schad, and T. Suzuki, AIP Adv. **7**, 56226 (2017).

[50] H. Adachi, T. Hata, T. Matsushima, T. Motohiro, and K. Tominaga, *Handbook of Sputtering Technology*, 2nd ed. (Elsevier, 2012).

[51] S. A. Campbell, *Fabrication Engineering at the Micro and Nanoscale*, 3rd ed.

(OUP, 2008).

[52] M. Ohring, *Materials Science of Thin Films*, 2nd ed. (Academic Press, n.d.).

[53] J. A. Thornton, J. Vac. Sci. Technol. A **4**, 3059 (1986).

[54] A. Gibaud and S. Hazra, Curr. Sci. **78**, 1467 (2000).

[55] M. Björck and G. Andersson, J. Appl. Cryst. **40**, 1174 (2007).

[56] A. Martins, N. M. Souza-Neto, M. C. A. Fantini, A. D. Santos, R. J. Prado, and A. Y. Ramos, J. Appl. Phys. **100**, (2006).

[57] J. Yano and V. K. Yachandra, Photosynth Res **102**, 241 (2009).

[58] U. Bergmann and P. Glatzel, Photosynth. Res. **102**, 255 (2009).

[59] K. Tsutsumi, H. Nakamori, and K. Ichikawa, Phys Rev. B. **13**, 929 (1976).

[60] J. P. Rueff, C. C. Kao, V. V Struzhkin, J. Badro, J. Shu, R. J. Hemley, and H. K. Mao, Phys. Rev. Lett. **82**, 3343 (1999).

[61] L. J. P. Ament, M. Van Veenendaal, T. P. Devereaux, J. P. Hill, and J. Van Den Brink, Rev. Mod. Phys. **83**, 705 (2011).

[62] G. van der Laan and A. I. Figueroa, Coord. Chem. Rev. **277**, 95 (2014).

[63] https://commons.wikimedia.org/wiki/File:TEM_ray_diag.basic.en.png, (n.d.).

[64] L. Neel, J. Phys. Radium **15**, 225 (1954).

[65] S. D. Bader, Rev. Mod. Phys. **78**, 1 (2006).

[66] I. Zutic, J. Fabian, and S. Das Sarma, Rev. Mod. Phys. **76**, 323 (2004).

[67] M. Jamet, W. Wernsdorfer, C. Thirion, D. Mailly, V. Dupuis, P. Mélinon, and A. Pérez, Phys. Rev. Lett. **86**, 4676 (2001).

[68] H. Lv, Y. Lei, A. Datta, and G. Wang, Appl. Phys. Lett. **103**, 132405 (2013).

[69] C. Liu, E. R. Moog, and S. D. Bader, Phys. Rev. Lett. **60**, 2422 (1988).

[70] H. C. Mireles and J. L. Erskine, Phys. Rev. Lett. **87**, 37201 (2001).

[71] H. Kachkachi and H. Mahboub, J. Mag. Mag. Mater. **278**, 334 (2004).

[72] D. A. Garanin and H. Kachkachi, Phys. Rev. Lett. **90**, 65504 (2003).

[73] J. M. Qiu and J. P. Wang, Appl. Phys. Lett. **88**, 192505 (2006).

[74] J.-M. Qiu and J.-P. Wang, Adv. Mater. **19**, 1703 (2007).

[75] R. Wang, O. Dmitrieva, M. Farle, G. Dumpich, H. Ye, H. Poppa, R. Kilaas, and C. Kisielowski, Phys. Rev. Lett. **100**, 17205 (2008).

[76] J. M. Qiu, J. M. Bai, and J. P. Wang, Appl. Phys. Lett. **89**, 222506 (2006).

[77] T. Shima, K. Takanashi, Y. K. Takahashi, and K. Hono, Appl. Phys. Lett. **85**, 2571 (2004).

[78] T. Shima, K. Takanashi, Y. K. Takahashi, and K. Hono, Appl. Phys. Lett. **88**, 63117 (2006).

[79] L. Han, U. Wiedwald, B. Kuerbanjiang, and P. Ziemann, Nanotechnology **20**, 285706 (2009).

[80] O. Mosendz, S. Pisana, J. W. Reiner, B. Stipe, and D. Weller, J. Appl. Phys. **111**, 07B729 (2012).

[81] Y. Tamada, Y. Morimoto, S. Yamamoto, M. Takano, S. Nasu, and T. Ono, J. Magn. Magn. Mater. **310**, 2381 (2007).

[82] J. Zhou, R. Skomski, and D. J. Sellmyer, J. Appl. Phys. **99**, 08F909 (2006).

[83] H. Kachkachi and M. Dimian, Phys. Rev. B. **111**, 174419 (2002).

[84] http://math.nist.gov/oommf, (n.d.).

[85] B. Ma, H. Wang, H. Zhao, C. Sun, R. Acharya, and J. P. Wang, J. Appl. Phys. **109**, 83907 (2011).

[86] Z. L. Zhao, J. S. Chen, J. Ding, J. B. Yi, B. H. Liu, and J. P. Wang, Appl. Phys. Lett. **88**, 52503 (2006).

[87] J. S. Chen, Y. Xu, and J. P. Wang, J. Appl. Phys. **93**, 1661 (2003).

[88] S. Okamoto, N. Kikuchi, O. Kitakami, T. Miyazaki, Y. Shimada, and K. Fukamichi, Phys. Rev. B **66**, 24413 (2002).

[89] K. Roy, S. Bandyopadhyay, and J. Atulasimha, Appl. Phys. Lett. **99**, 99 (2011).

[90] J.-M. Hu, Z. Li, L.-Q. Chen, and C.-W. Nan, Nat. Commun. **2**, 553 (2011).

[91] M. Ghidini, R. Pellicelli, J. L. Prieto, X. Moya, J. Soussi, J. Briscoe, S. Dunn, and N. D. Mathur, Nat. Commun. **4**, 1453 (2013).

[92] A. K. Biswas, S. Bandyopadhyay, and J. Atulasimha, Appl. Phys. Lett. **103**, (2013).

[93] M. Buzzi, R. V. Chopdekar, J. L. Hockel, A. Bur, T. Wu, N. Pilet, P. Warnicke, G. P. Carman, L. J. Heyderman, and F. Nolting, Phys. Rev. Lett. **111**, 1 (2013).

[94] S. Zhang, Y. Zhao, X. Xiao, Y. Wu, S. Rizwan, L. Yang, P. Li, J. Wang, M. Zhu, H. Zhang, X. Jin, and X. Han, Sci. Rep. **4**, 3727 (2014).

[95] K. Roy, S. Bandyopadhyay, and J. Atulasimha, J. Appl. Phys. **112**, (2012).

[96] K. Roy, S. Bandyopadhyay, and J. Atulasimha, Phys. Rev. B. **83**, 1 (2011).

[97] B. Zhu, C. C. H. Lo, S. J. Lee, and D. C. Jiles, J. Appl. Phys. **89**, 7009 (2001).

[98] C.-Y. Liang, S. M. Keller, A. E. Sepulveda, A. Bur, W.-Y. Sun, K. Wetzlar, and G. P. Carman, Nanotechnology **25**, 435701 (2014).

[99] M. Salehi Fashami, K. Roy, J. Atulasimha, and S. Bandyopadhyay, Nanotechnology **22**, 309501 (2011).

[100] P. V. Lukashev, N. Horrell, and R. F. Sabirianov, J. Appl. Phys. **111**, 07A318 (2012).

[101] A. Sakuma, J. Phys. Osc. Jpn. **63**, 3053 (1994).

[102] B. Zhang, J. Chen, and G. M. Chow, IEEE Trans. Magn. **47**, 4402 (2011).

[103] S. N. Hsiao, F. T. Yuan, H. W. Chang, H. W. Huang, S. K. Chen, and H. Y. Lee, Appl. Phys. Lett. **94**, 232505 (2009).

[104] A. Kotani and S. Shin, Rev. Mod. Phys. **73**, 203 (2001).

[105] T. Sham, S. Naftel, P.-S. Kim, R. Sammynaiken, Y. Tang, I. Coulthard, A. Moewes, J. Freeland, Y.-F. Hu, and S. Lee, Phys. Rev. B. **70**, 45313 (2004).

[106] L. G. Parratt, Rev. Mod. Phys. **31**, 616 (1959).

[107] L. J. P. Ament, M. Van Veenendaal, T. P. Devereaux, J. P. Hill, and J. Van Den Brink, Rev. Mod. Phys. **83**, 705 (2011).

[108] A. Martins, N. M. Souza-Neto, M. C. A. Fantini, A. D. Santos, R. J. Prado, and A. Y. Ramos, J. Appl. Phys. **100**, 13905 (2006).

[109] K. F. Dong, H. H. Li, and J. S. Chen, J. Appl. Phys. **113**, 233904 (2013).

[110] B. A. Mattern, G. T. Seidler, M. Haave, J. I. Pacold, R. A. Gordon, J. Planillo, J. Quintana, and B. Rusthoven, Rev. Sci. Instrum. **83**, (2012).

[111] P. Tougaard, S.; Simund, Phys. Rev. B. **25**, 4452 (1982).

[112] H. Ebert, D. Ködderitzsch, and J. Minár, Reports Prog. Phys. **74**, 96501 (2011).

[113] M. Schaffer, B. Schaffer, and Q. Ramasse, Ultramicroscopy **114**, 62 (2012).

[114] M. Y. Sun, X. . W. Xu, X. . A. Liang, X. W. Sun, Y. J. Zheng, X. W. Xu, X. A. Liang, X. W. Sun, and Y. J. Zheng, J. Alloy. Compd. **672**, 59 (2016).

[115] J.-P. Wang, W. Shen, and J. Bai, IEEE Trans. Magn. **41**, (2005).

[116] N. M. S. S. P. Parkin and K. P. Roche, Phys. Rev. Lett. **23**, 130 (1990).

[117] M. Kobayashi, T. Kai, N. Takano, and K. Shiiki, J. Phys. Condens. Matter **7**, 1835 (1995).

[118] S. Schönecker, M. Richter, K. Koepernik, and H. Eschrig, Phys Rev. B. **85**, 24407 (2012).

[119] S. Watanabe, T. Komine, T. Kai, and K. Shiiki, J. Magn. Magn. Mater. **220**, 277 (2000).

[120] K. Shiiki and O. Hio, Jpn. J. Appl. Phys. **36**, 7360 (1997).

[121] D. Odkhuu, S. H. Rhim, N. Park, K. Nakamura, and S. C. Hong, Phys. Rev. B. **91**, 14437 (2015).

[122] U. May, R. Calarco, J. O. Hauch, H. Kittur, M. Fonine, and U. R, **489**, 144 (2001).

[123] F. Martin, J. Pacaud, G. Abadias, C. Jaouen, and P. Guérin, Appl. Surf. Sci. **188**, 90 (2002).

[124] A. B. Yankovich, B. Berkels, W. Dahmen, P. Binev, S. I. Sanchez, S. A.

Bradley, A. Li, I. Szlufarska, and P. M. Voyles, Nat. Commun. **5**, 4155 (2014).

[125] C. Kittel, *Introduction to Solid State Physics*, 8th ed. (Wiley, New York, 2004).

[126] A. Manchon and S. Zhang, Phys. Rev. B. **79**, 94422 (2009).

[127] M. Cubukcu, O. Boulle, M. Drouard, K. Garello, C. Onur Avci, I. Mihai Miron, J. Langer, B. Ocker, P. Gambardella, and G. Gaudin, Appl. Phys. Lett. **104**, (2014).

[128] L. Liu, T. Moriyama, D. C. Ralph, and R. A. Buhrman, Phys. Rev. Lett. **106**, 36601 (2011).

[129] L. Liu, C. F. Pai, Y. Li, H. W. Tseng, D. C. Ralph, and R. A. Buhrman, Science (80-.). **336**, 555 (2012).

[130] K. Wu, T. Klein, V. D. Krishna, D. Su, A. M. Perez, and J. P. Wang, ACS Sens. **2**, 1594 (2017).